

UNIVERSITY OF CALIFORNIA
Santa Barbara

Development of Ultra-Low Resistance Ohmic Contacts for InGaAs/InP HBTs

A Thesis submitted in partial satisfaction
of the requirements for the degree of

Doctor of Philosophy

in

Electrical and Computer Engineering

by

Ashish Baraskar

Committee in Charge:

Professor Mark J. W. Rodwell, Chair

Professor Arthur Gossard

Professor Christopher Palmstrøm

Professor Umesh Mishra

September 2011

The Thesis of
Ashish Baraskar is approved:

Professor Arthur Gossard

Professor Christopher Palmstrøm

Professor Umesh Mishra

Professor Mark J. W. Rodwell, Committee Chairperson

June 2011

Development of Ultra-Low Resistance Ohmic Contacts for InGaAs/InP HBTs

Copyright © 2011

by

Ashish Baraskar

Abstract

Development of Ultra-Low Resistance Ohmic Contacts for InGaAs/InP HBTs

Ashish Baraskar

With the continued scaling of transistors to obtain increased transistor bandwidth and packing density, achieving very low resistance metal-semiconductor contacts becomes crucial. The base and emitter contact resistivities in heterojunction bipolar transistors (HBTs) must decrease in proportion to the inverse square of the transistor cutoff frequency. Similarly for field-effect transistors (FETs), progressive reduction in contact resistivity is required for both increased speed of operation and increased device packing density. Contact resistivities less than $10^{-8} \Omega\text{-cm}^2$ are required for III-V HBTs and FETs for having simultaneous 1.5 THz current-gain (f_t) and power-gain (f_{max}) cutoff frequencies. Owing to higher electron velocity, higher transistor bandwidths are more readily obtained in InGaAs than in Si, hence there is strong motivation to develop low resistance ohmic contacts to InGaAs.

This dissertation is focused on efforts to develop ultra-low resistance ohmic contacts to n-In_{0.53}Ga_{0.47}As, n-InAs and p-In_{0.53}Ga_{0.47}As for their application in InP based HBTs. There were four main challenges in obtaining ultra-low contact resistivities:

1. High doping: Attainment of high active carrier concentration which is required for reducing the depletion region in the semiconductor.
2. Surface preparation: Contact resistivity strongly depends on surface preparation and obtaining resistivities $10^{-8} \Omega\text{-cm}^2$ requires a significant attention to removal of semiconductor surface oxides before the contacts are made.
3. Refractory metal contact: Owing to high current densities ($50 \text{ mA}/\mu \text{ m}^2$) and to the high temperatures involved during fabrication of the scaled HBTs and FETs, it becomes important to keep the metal semiconductor junctions abrupt for their continued operation as desired. To achieve this thermal stability, it is required to use refractory metals for making the contact.
4. Accurate extraction of contact resistivities

In this work, molecular beam epitaxy thin-film growth technique was used to grow the semiconductor thin films. After careful growth optimization and calibrations, the highest active carrier concentration obtained was $6 \times 10^{19} \text{ cm}^{-3}$, $1 \times 10^{20} \text{ cm}^{-3}$ (**record highest**) and $2.2 \times 10^{20} \text{ cm}^{-3}$ for n-In_{0.53}Ga_{0.47}As, n-InAs and p-In_{0.53}Ga_{0.47}As, respectively. W, Mo and Ir refractory metals were chosen to form the contacts to these semiconductors to achieve thermal stability. Transmission line model structures were designed to accurately determine the contact resistivities. The lowest contact resistivities obtained were $(0.98 \pm 0.34) \times 10^{-8} \Omega\text{-cm}^2$, $(0.6 \pm 0.4) \times 10^{-8} \Omega\text{-cm}^2$ and

$(0.6 \pm 0.5) \times 10^{-8} \Omega\text{-cm}^2$ for contacts to n-In_{0.53}Ga_{0.47}As, n-InAs and p-In_{0.53}Ga_{0.47}As, respectively, which are the **lowest contact resistivities** reported to date for these semiconductors. Contacts to n-In_{0.53}Ga_{0.47}As and n-InAs were found to remain thermally stable. However, slight degradation on annealing was observed for contacts made to p-In_{0.53}Ga_{0.47}As. We have also generated theoretical models to validate our experimental data. The models were extended to calculate the lowest possible contact resistivities for GaAs, InP, InSb and GaSb.

Contents

Abstract	iv
List of Figures	x
List of Tables	xiv
1 Introduction	1
1.1 Current Transport Mechanisms	5
1.2 Metal-Semiconductor Contact Resistance	8
1.3 Ohmic contacts	9
1.3.1 Why Ultra-Low Resistance Ohmic Contacts?	9
1.3.2 Thermal Stability	14
1.4 Survey of ohmic contacts	15
1.5 Thesis Goal and Approach	17
1.6 Experimental Techniques	21
1.6.1 Thin Film Growth: Molecular Beam Epitaxy (MBE)	21
1.6.2 Film Characterization	22
2 Transmission Line Model (TLM) structures	28
2.1 Design of TLM structures	31
2.2 Error Analysis	35
3 n-InGaAs: Epitaxial Growth and Ohmic Contacts	43
3.1 Doping Calibrations	43
3.1.1 Dopant flux calibration	44
3.1.2 Arsenic flux calibration	44
3.1.3 Growth temperature calibration	45
3.2 Ohmic Contacts	50

3.2.1	In-situ contacts	50
3.2.2	Ex-situ contacts	56
3.2.3	Quasi-insitu contacts	56
4	n-InAs: Thin Film Growth and Ohmic Contacts	60
4.1	n-InAs growth and doping calibrations	61
4.2	Ohmic Contacts	63
5	p-InGaAs: Epitaxial Growth and Ohmic Contacts	67
5.1	pInGaAs Doping Calibrations	67
5.1.1	Dopant flux calibrations	67
5.1.2	Arsenic flux calibrations	68
5.1.3	Substrate temperature calibrations	69
5.2	Ohmic Contacts	73
5.2.1	In-situ Contacts	73
5.2.2	Ex-situ Contacts	74
5.3	Capacitance-Voltage Measurements	77
6	Thermal Stability	80
7	Theoretical Analysis	85
7.1	Current Density Derivation	85
7.1.1	Calculation of transmission coefficient, T: Parabolic case	93
7.1.2	Transmission probability: Non-parabolic case	103
7.2	Contact Resistivity Comparison	105
7.2.1	nInAs Contact Resistivity	106
7.2.2	n-In _{0.53} Ga _{0.47} As contact resistivity	112
7.2.3	p-In _{0.53} Ga _{0.47} As contact resistivity	114
7.2.4	Contact resistivities for GaAs, InP, GaSb and InSb	115
8	Conclusions and Future Work	132
8.1	High doping	132
8.2	Contact Resistivity	133
8.3	Future Work	136
8.3.1	Epitaxial Contacts	136
8.3.2	Regrown Base Ohmic Contacts	136
8.3.3	Contact Resistivity Error Reduction	137
8.3.4	Annealing Studies	138
	Bibliography	139

A	Transformation of k-vectors	146
B	TLM Fabrication Process Flow	148

List of Figures

1.1	Energy-band diagram of a metal-semiconductor contact	2
1.2	Various proposed models for explaining the origin of Fermi level pinning [1]	4
1.3	Current transport mechanisms across a metal semiconductor interface .	6
1.4	HBT cross section showing various parameters	11
1.5	MOSFET schematic showing all the relevant capacitances and resistance in the on state ($V_{gs} = V_{ds} = V_{dd}$) [2].	12
1.6	MOSFET schematic showing the source resistance components[2]. . .	13
1.7	TEM image showing Pd diffusion in InGaAs on annealing (TEM: Evan Lobisser).	15
1.8	Schematic of a molecular beam epitaxy system [3].	22
1.9	Schematic illustrating van der Pauw technique [4]	24
1.10	Schematic illustrating (a) Hall effect (b) sample geometry for n_s and μ_s measurements [4].	25
1.11	$1/C^2$ versus applied bias plot for ϕ_B measurement [5]	26
2.1	Cross-sectional circuit model for transmission line model structures .	29
2.2	Variation of electron concentration and mobility with Si atomic concentration	31
2.3	Scanning electron micrograph of the previous TLM structures used in our group.	32
2.4	Four point probe measurement illustrating probe positioning for removing the component of metal resistance.	34
2.5	Scanning electron micrograph of the re-designed TLM structures used in this work.	34
2.6	Scanning electron micrograph of the TLM structure. Non uniform edges are indicated by arrows.	36

2.7	Scanning electron micrograph of the TLM structure indicating current distribution	37
2.8	Scanning electron micrograph of the TLM structure indicating current distribution	38
2.9	Illustration of 'worst case' fit obtained for various combinations of slopes and intercepts.	42
3.1	Variation of electron concentration with total silicon concentration for samples grown at a substrate temperature of 460 ° C and at an As flux of 5×10^{-6} Torr.	45
3.2	Variation of electron concentration with arsenic flux for samples grown at a substrate temperature of 460 ° C.	46
3.3	Variation of electron concentration with substrate temperature.	47
3.4	Variation of electron concentration with the total Si concentration for samples grown at various substrate temperatures.	48
3.5	Variation of mobility with electron concentration for the samples grown at three different temperatures.	49
3.6	Variation of contact resistivity and electron concentration with total Si concentration.	52
3.7	Variation of contact resistivity and electron concentration with total Si concentration. Error bars are indicated on respective contact resistivity values.	53
3.8	Donor impurity level and donor impurity band at low, medium and high doping concentrations for (a) an ordered impurity distribution and (b) a random impurity distribution. (c) Band diagram illustrating hopping conduction and impurity band conduction (from Schubert [6]).	54
3.9	Band gap narrowing resulting from high donor in InP (solid) and $\text{In}_{0.53}\text{Ga}_{0.47}\text{As}$ (dashed) [7].	55
3.10	RHEED patterns of the atomic H cleaned sample along the (110) and ($\bar{1}10$) azimuths showing (2×4) reconstructed surface.	58
4.1	Variation of electron concentration and mobility with Si atomic concentration	62
4.2	Variation of electron concentration with substrate temperature.	63
4.3	Variation of contact resistivity with electron concentration.	65
4.4	Measured TLM resistance as a function of pad spacing for the sample with $\rho_c = (0.6 \pm 0.4) \times 10^{-8} \Omega\text{-cm}^2$	66
5.1	Variation of hole concentration and mobility with CBr_4 foreline pressure.	69
5.2	Variation of hole concentration with group V/group III ratio during growth.	70

5.3	Variation of hole concentration with substrate temperature	71
5.4	Dependence of hole concentration on substrate temperature	72
5.5	Variation of contact resistivity with hole concentration for in-situ W, Mo and Ir contacts.	74
5.6	Variation of contact resistivity with hole concentration for ex-situ W contacts.	76
5.7	Reverse-bias $1/C^2$ versus voltage measured at room temperature for the Schottky diodes fabricated with W, Mo and Ir.	79
6.1	TEM images of W-pInGaAs samples before and after annealing. Inter-mixing between Ti and Au can be observed for annealed samples	83
6.2	Compositional line scan along the cross section obtained by EDS	84
7.1	Schematic of the approximated potential barrier.	94
7.2	Schematic of the approximated potential barrier.	95
7.3	Schematic of a potential energy step	102
7.4	Variation of electron concentration with Fermi energy level for parabolic and non-parabolic case	107
7.5	Variation of contact resistivity with electron concentration for parabolic and non-parabolic case.	108
7.6	Comparison of contact resistivity obtained for a step barrier and for the case when $T(E)=1$ for parabolic energy dispersion.	109
7.7	Comparison of contact resistivity obtained for a step barrier and for the case when $T(E)=1$ for non-parabolic energy dispersion.	110
7.8	Comparison of experimental and calculated contact resistivity	111
7.9	Energy band diagram for InAs [8].	112
7.10	Variation of contact resistivity with electron concentration for parabolic case for various ϕ_B . Experimental data points are also plotted for comparison.	113
7.11	Variation of contact resistivity with electron concentration for various metal Fermi energies	114
7.12	Variation of contact resistivity with electron concentration for various electron effective mass in metal	115
7.13	Dependence of electron transmission probability on effective mass	116
7.14	Variation of electron concentration with Fermi energy level for parabolic and non-parabolic energy bands for n-type $\text{In}_{0.53}\text{Ga}_{0.47}\text{As}$	117
7.15	Variation of contact resistivity with electron concentration for parabolic and non-parabolic energy bands for n-type $\text{In}_{0.53}\text{Ga}_{0.47}\text{As}$	118
7.16	Comparison of experimental and calculated contact resistivity for n-type $\text{In}_{0.53}\text{Ga}_{0.47}\text{As}$. Calculations were done assuming non-parabolic energy bands.	119

7.17	Comparison of experimental and calculated contact resistivities at various ϕ_B . Calculations were done assuming parabolic energy bands.	120
7.18	Variation of electron concentration with Fermi energy level for parabolic case.	121
7.19	Comparison of calculated and experimental contact resistivities at various ϕ_B	122
7.20	Comparison of contact resistivities of various semiconductors indicating the dependence on effective electron mass.	123
7.21	Comparison of contact resistivities of various p-type semiconductors.	124
7.22	Comparison of contact resistivities of various semiconductors indicating the effect of effective hole mass.	125
7.23	Comparison of calculated and experimental contact resistivities at various ϕ_B for n-type GaAs	126
7.24	Comparison of calculated and experimental contact contact resistivities at various ϕ_B for p-type GaAs	126
7.25	Comparison of calculated and experimental contact contact resistivities at various ϕ_B for n-type GaSb	127
7.26	Comparison of calculated and experimental contact resistivities at various ϕ_B for p-type GaSb	127
7.27	Comparison of calculated and experimental contact resistivities at various ϕ_B for n-type InP	128
7.28	Comparison of calculated and experimental contact resistivities at various ϕ_B for p-type InP	128
7.29	Comparison of calculated and experimental contact resistivities at various ϕ_B for n-type InSb	129
7.30	Comparison of calculated and experimental contact resistivities at various ϕ_B for p-type InSb	129
7.31	Comparison of calculated and experimental contact resistivities at various ϕ_B for n-type InGaAs	130
7.32	Comparison of calculated and experimental contact resistivities at various ϕ_B for p-type InGaAs	130
7.33	Comparison of calculated and experimental contact resistivities at various ϕ_B for n-type InAs	131
7.34	Comparison of calculated and experimental contact resistivities at various ϕ_B for p-type InAs	131
8.1	Scanning electron micrograph of p-InGaAs regrowth on dummy emitters.	137

List of Tables

1.1	Summary of simultaneous parameter scaling for a $\gamma:1$ increase in HBT and circuit bandwidth	10
1.2	Refractory metal work functions and melting points	20
5.1	Refractory metal work functions and melting points	73
5.2	Refractory metal contact resistivity and Schottky barrier height	79
6.1	Resistivity comparison of various contacts before and after annealing	80
7.1	Compound semiconductor parameters	106

Chapter 1

Introduction

Metal semiconductor contacts have been studied widely over the past several decades. The first Schottky contact was demonstrated by Braun [9] in 1874 for metal sulphides. In 1938, Walter Schottky [10] and N. F. Mott [11] established a theoretical model explaining the rectification behavior of the metal semiconductor contacts. Metal semiconductor contacts can also be ohmic (non-rectifying) in nature. Ohmic contacts find extensive application in semiconductor devices and integrated circuits. Extensive discussions regarding the history, development and theory of metal semiconductor contacts can be found in references [12] [13]

The energy band diagram for a metal semiconductor contact is shown in figure 1.1. For an ideal contact, the barrier height, $q\phi_B$ is given by

$$q\phi_B = q(\phi_m - \chi) \quad (1.1)$$

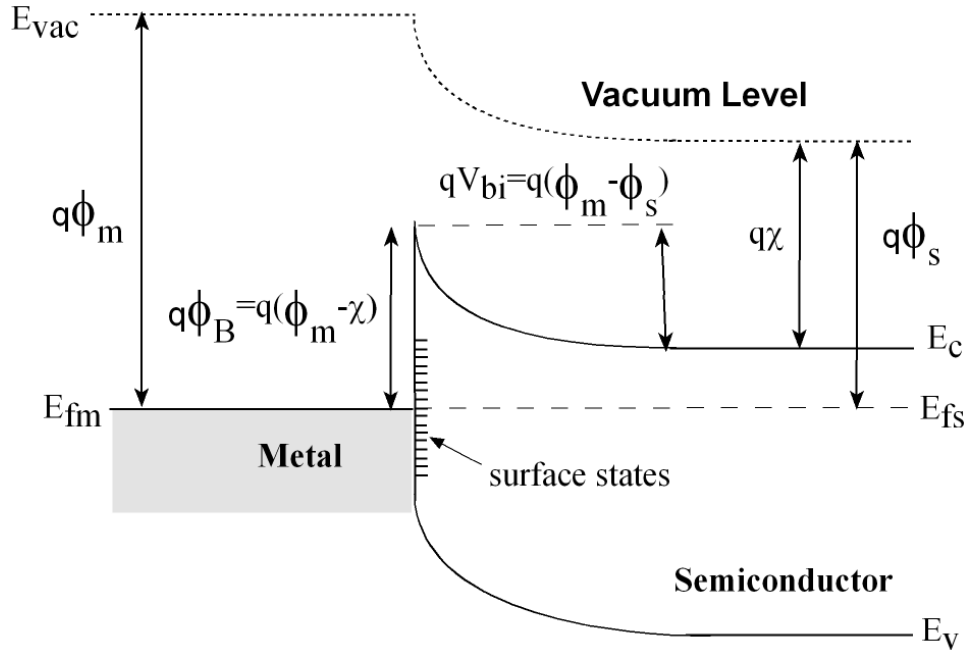


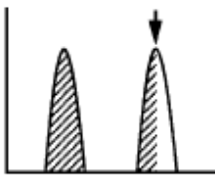
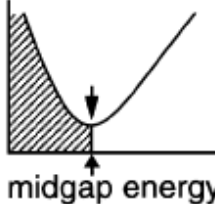
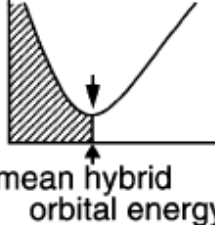
Figure 1.1: Energy-band diagram of a metal-semiconductor contact

where $q\phi_m$ is the work function of the metal. $q\chi$ is the semiconductor electron affinity which can be expressed as

$$q\chi = q\phi_s - (E_c - E_f) \quad (1.2)$$

where $q\phi_s$ is the work function of the semiconductor, E_c is the conduction band energy and E_f is the Fermi energy level. However, in practice, surface dipoles exist due the presence of dangling bonds on semiconductor surface. These dangling bonds result in surfaces states which are distributed in energy within the band gap of the

semiconductor (shown in fig 1.1). In most covalent semiconductors, these surface states have a high density at a certain energy level known as neutral level (E_o). This neutral level tends to pin the Fermi level in the semiconductor and makes the Schottky barrier height weakly dependent on the metal work function [14][15]. Various models have been proposed to explain the origin of Fermi level pinning which include unified defect model (UDF)[16], metal induced gap state (MIGS)[17][18], disorder induced gap states (DIGS)[19] and the effective work function model[20]. Figure 1.2 summarizes the basic ideals of these models [1]. In spite of extensive research on metal semiconductor interfaces, the exact mechanism responsible for Fermi level pinning has not been clearly understood.

Models	origin of pinning states	N_{SS} distribution and pinning position	applicable interfaces	nature of pinning
Unified Defect Model	deep level related to stoichiometry, especially, As_{Ga}		V-S, S-S, I-S, M-S	extrinsic
MIGS Model	penetration of metal wave function into semiconductor		M-S	intrinsic
DIGS Model	loss of 2D periodicity due to disorder of bonds at interface		V-S, S-S, I-S, M-S	extrinsic
Effective Work Function Model	precipitation of As and P cluster at interface	pinned at E_F of metallic cluster	V-S, S-S, I-S, M-S	extrinsic

V-S : Vacuum-Semiconductor interface
 S-S : Semiconductor-Semiconductor interface
 I-S : Insulator-Semiconductor interface
 M-S : Metal-Semiconductor interface

Figure 1.2: Various proposed models for explaining the origin of Fermi level pinning [1]

1.1 Current Transport Mechanisms

The Schottky-barrier diode is mainly a majority-carrier device. As shown in figure 1.3, there are five prominent mechanisms of carrier transport across the metal semiconductor junction.

1. Thermionic emission over the top of the potential barrier
2. Quantum mechanical tunneling through the barrier
3. Tunneling via interface states
4. Generation/recombination in the space charge region
5. Minority carrier transport

Among these transport mechanisms, tunneling and thermionic emission are the most important carrier transport processes. At equilibrium, whether one process or the other is dominant depends on the active carrier concentration. Other conduction mechanisms like surface generation/recombination or minority carrier injection are less efficient and can be neglected. Tunneling via interface states may also become important at heavy doping concentrations (discussed in section 3.2.1).

At low doping concentrations, electron transport is dominated by thermionic emission. In this case, the depletion region is too thick and results in minimal or no tunneling

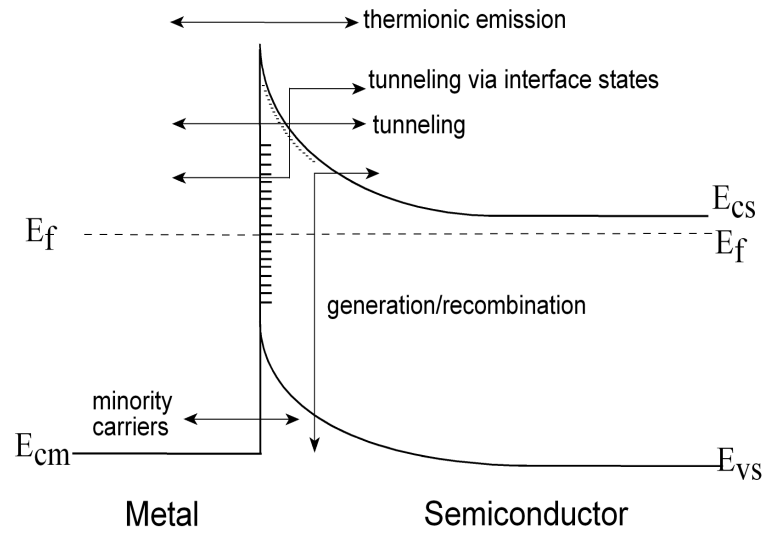


Figure 1.3: Current transport mechanisms across a metal semiconductor interface

across the interface. The thermionic current across a metal semiconductor junction is given by:

$$J = A^*T^2 \exp(-q\phi_B/kT)(\exp(qV/kT) - 1) \quad (1.3)$$

where,

$$A = 4\pi qm^*k^2/h^3 \quad (1.4)$$

is the effective Richardson constant. For thermionic emission, the kinetic energy of the carriers should be high in order to surpass the potential barrier. If the carrier

temperature is raised, the kinetic energy of the carriers increases resulting in enhanced thermionic emission [14].

For heavily doped semiconductors, the thickness of the semiconductor depletion region decreases. Due to this reduction in depletion region, carriers can penetrate or tunnel through the barrier. Thus, above a certain carrier concentration, tunneling current starts to dominate. If the tunneling of carriers takes place at energies between the top of the barrier and the Fermi level, the process is called as thermionic field emission. If most of the tunneling of carriers takes place close to the Fermi level, the process is known as field emission [21][14]. The relative contributions of these components depend on both temperature and active carrier concentration. A parameter, E_{oo} , was defined as [21],

$$E_{oo} = q\hbar/2\sqrt{N/m^*\epsilon_r} \quad (1.5)$$

when $kT \gg E_{oo}$, thermionic emission dominates

when $kT \approx E_{oo}$, thermionic field emission dominates

when $kT \ll E_{oo}$, field emission dominates

1.2 Metal-Semiconductor Contact Resistance

Metal-semiconductor contact resistance is defined as the resistance to the flow of carriers across the metal-semiconductor interface. The contact resistance is characterized by specific contact resistivity, $\rho_c(\Omega - \mu m^2)$ which is defined as:

$$\frac{1}{\rho_c} = \frac{dJ}{dV} @V=0 \quad (1.6)$$

where V is the voltage across the barrier and J is the current density through the barrier. This resistance could be due to different factors as discussed here. For a metal semiconductor contact, the current density for the carriers moving from semiconductor to metal is given by:

$$dJ_{sm} = \frac{2q}{(2\pi)^3} f(E, E_{fs})(1 - f(E, E_{fm}))v_{sz}T dk_{sx}dk_{sy}dk_{sz} \quad (1.7)$$

where $(1 - f(E, E_{fm}))$ accounts for the reflection of carriers due to occupied states in metal, T is the transmission probability of the carriers (including tunneling through the interface) and $v_{sz} = \hbar k_z/m_s$ is the velocity of the carriers crossing the interface. As can be seen from equation 1.6 and 1.7, even when $T=1$, there exists a finite contact resistance due to the difference in density of states across the interface and finite car-

rier mass resulting in finite carrier velocity. The lower limits on contact resistivity for various semiconductors are calculated in chapter 7.

1.3 Ohmic contacts

For semiconductors with very high active carrier concentration, the energy band bending is large resulting in a thin potential barrier at the metal-semiconductor interface. Carriers can easily tunnel through this thin potential barrier and tunneling becomes the dominant current transport mechanism, leading to high current densities at low voltage drops. For this type of contact, known as ohmic contact, the resistance is very low and the I-V characteristics can be approximated as linear. Ohmic contacts are an integral part of all semiconductor devices. It is used to apply external voltages as well as supply current from external sources.

1.3.1 Why Ultra-Low Resistance Ohmic Contacts?

Bipolar Transistors

Ultra-low resistance metal-semiconductor contacts are fundamental to the continued scaling of transistors towards THz bandwidths. In order to improve HBT as well as analog and digital IC speed, all significant capacitances and transit times must be simultaneously reduced by an appropriate amount corresponding to an intended $\gamma:1$ in-

crease in bandwidth [22][23]. This is done while maintaining constant all resistances, the operating voltages and current I_c , and transconductance, $g_m = qI_c/\eta kT$ i.e. I_c and $g_m \propto \gamma^0$. The proportion by which various parameters need to be scaled for a $\gamma:1$ increase in HBT bandwidth are listed in Table 1.1

Table 1.1: Summary of simultaneous parameter scaling for a $\gamma:1$ increase in HBT and circuit bandwidth

Device Parameter	Required Change
collector depletion layer thickness	decrease $\gamma:1$
base thickness	decrease $\sqrt{\gamma}:1$
emitter-base junction width	decrease $\gamma^2:1$
collector-base junction width	decrease $\gamma^2:1$
emitter depletion thickness	decrease $\sqrt{\gamma}:1$
emitter contact resistivity, ρ_{ex}	decrease $\gamma^2:1$
emitter current density	increase $\gamma^2:1$
base contact resistivity	decrease $\gamma^2:1$
bias currents and voltages	constant
resistances	constant

Consider equations 1.8 and 1.9, which describe the dependence of current gain cut-off frequency (f_t) and power gain cut-off frequency (f_{max}) on various parameters. Some of these parameters are indicated in fig. 1.4

$$\frac{1}{2\pi f_t} = \tau_{tr} + C_{cb}(R_{ex} + R_c) + \frac{\eta kT}{qI_e}(C_{cb} + C_{je}) \quad (1.8)$$

$$f_{max} = \sqrt{\frac{f_t}{8\pi(R_{bb}C_{cb})_{eff}}} \quad (1.9)$$

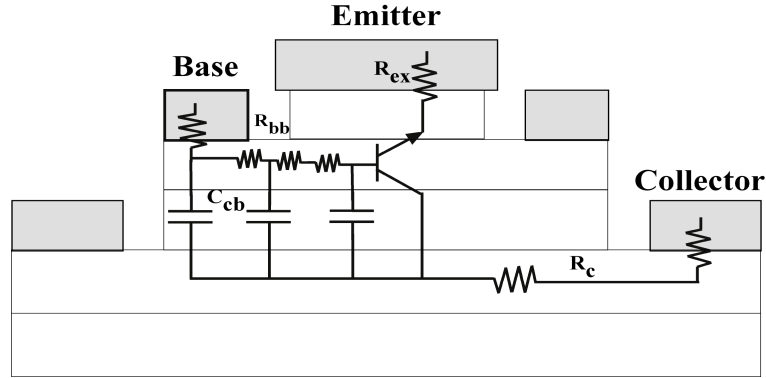


Figure 1.4: HBT cross section showing various parameters

Reducing the collector depletion layer thickness T_c by $\gamma^2:1$ and base thickness T_b by $\gamma^1/2:1$ reduces $\tau_{tr}(= \tau_b + \tau_c)$ by the required proportion. This, however, results in an increase in C_{cb} and R_{bb} . In order to reduce C_{cb} by $\gamma:1$, the emitter and collector junction areas need to be reduced in proportion to $\gamma^2:1$. At the $0.6 \mu\text{m}$ emitter junction scaling generation, scaling for a $\gamma:1$ increase in bandwidth would result in R_{bb} as a whole remaining unchanged. To obtain the required reduction in C_{cb} , the ohmic contact width must be reduced $\gamma:1$, which requires a $\gamma^2:1$ reduction in the base contact resistivity ρ_c .

Field Effect Transistors

The current gain cutoff frequency f_t of a MOSFET is given by

$$\frac{1}{2\pi f_t} = \frac{C_{gg,t}}{g_m} + \frac{C_{gg,t}}{g_m}(R_s + R_d)g_d + (R_s + R_d)C_{gd,t} \quad (1.10)$$

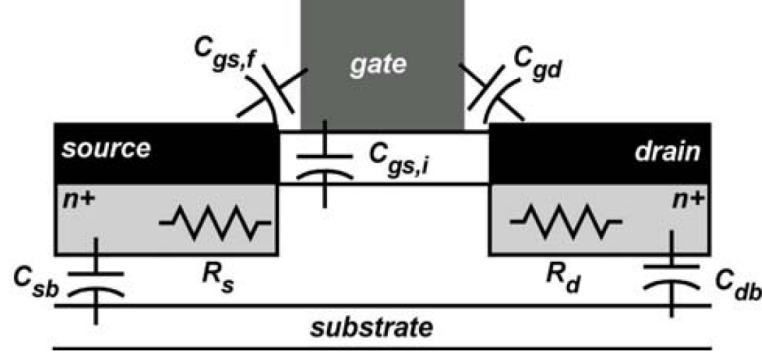


Figure 1.5: MOSFET schematic showing all the relevant capacitances and resistance in the on state ($V_{gs} = V_{ds} = V_{dd}$) [2].

where $C_{gg,t} = C_{gs,t} + C_{gd,t} = C_{gs,i} + C_{gs,f} + C_{gd,t}$ is the total gate capacitance, $C_{gd,t}$ is the total gate to drain capacitance, g_d is the output conductance and R_s , R_d are the parasitic source and drain resistances [24]. Figure 1.5 shows the relevant capacitances and resistances for a MOSFET.

For large gate length, $\frac{C_{gg,t}}{g_m} \approx \frac{C_{gs,i}}{g_m}$, which is usually referred to as the intrinsic delay of the transistor and is approximately given by $\tau_{int} = L_g/v$, where v is the electron velocity under the gate. The terms in equation 1.10, $\frac{C_{gg,t}}{g_m}(R_s + R_d)g_d + (R_s + R_d)C_{gd,t}$ refer to the RC delay of the transistor. In the constant voltage scaling, the aim is to increase the device bandwidth $\gamma:1$ by reducing all the transport delays and capacitances by $\gamma^2:1$ while keeping constant all resistances, voltages and currents [22][23][25]. This is achieved by scaling down both the lateral and vertical device dimensions by a factor of $\gamma:1$.

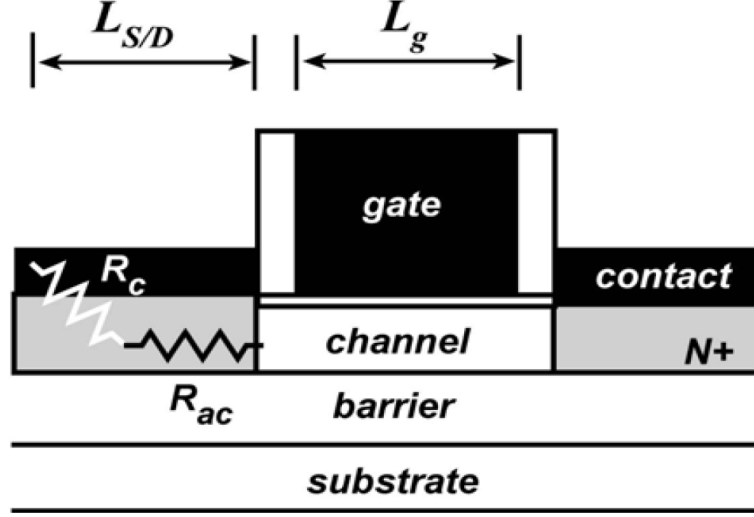


Figure 1.6: MOSFET schematic showing the source resistance components[2].

Scaling the oxide thickness (t_{ox}) increases the equivalent gate capacitance $C_{gs,i} = C_{eq} \approx 1/t_{ox}$ per unit area. Reducing the gate width W_g by $\gamma:1$ keeps the $g_m \approx W_g C_{eq} v_{inj}$ and $I_d \approx W_g C_{eq} v_{inj} (V_g - V_t)$ constant. Reducing the gate length L_g $\gamma:1$ reduces the total gate capacitance $C_{gs} = C_{eq} W_g L_g + \alpha W_g$ by $\gamma:1$. The second term in C_{gs} is the fringing capacitance. Other parasitic capacitances C_{gd} , C_{sb} and $C_{db} \propto W_g$ are also scaled down by $\gamma:1$. The source/drain contact length $L_{s/d}$ is also scaled by a factor $\gamma:1$ in proportion with the gate length. This requires a $\gamma^2:1$ decrease in the specific contact resistivity to keep the source resistance $R_s = \frac{\rho_c}{L_{s/d} W_g} + \frac{\rho_s L_{s/d}}{W_g}$ constant [2]. The different components of the source resistance are shown in fig. 1.6.

1.3.2 Thermal Stability

Today's high speed HBTs and FETs operate at high current densities ($50 \text{ mA}/\mu\text{m}^2$) leading to a lot of heat generation. Also, the processes involved in fabricating these devices involve heat treatment/annealing at elevated temperatures. Therefore, in a scaled device with very small device dimensions, it becomes important to keep the metal semiconductor junctions abrupt for their continued operation as desired. For example, in an HBT with 80 nm emitter-base junction, the desired base thickness is ≈ 25 nm. If a non-refractory metal, such as Pd, Pt, is used as the contact metal, it may diffuse through the base and short the collector. Figure 1.7 shows the cross-sectional TEM image of Pd contacts to p-type InGaAs. For this sample, 2.5 nm of Pd was deposited and the sample was then annealed at 250°C for 60 minutes under N_2 atmosphere. As seen in the figure, Pd diffuses about 15 nm in InGaAs on annealing. Similarly, Pt contacts formed to InGaAs base in an HBT were found to diffuse and deteriorate device characteristics [26]. Fukai et al [27] have compared the reliability of emitter contacts formed by non-refractory metal (Ti/Au) and refractory metal (W). It was shown that device reliability greatly improves with the use of refractory metals. Hence, in order to improve the reliability by keeping the metal-semiconductor interfaces abrupt, it is important to use refractory metals, such as Mo, W, Ir, for forming contacts to the semiconductor.

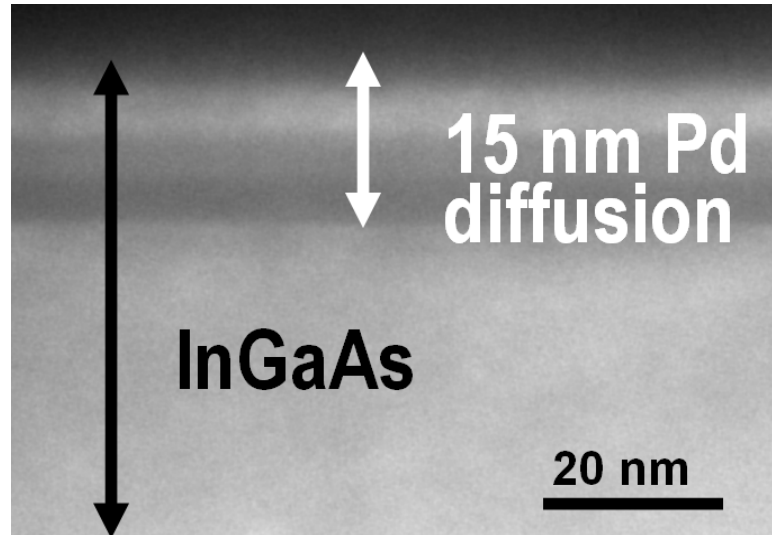


Figure 1.7: TEM image showing Pd diffusion in InGaAs on annealing (TEM: Evan Lobisser).

1.4 Survey of ohmic contacts

Ohmic contacts to III-V materials have been studied extensively over the past few decades. Numerous reports pertaining to the choice of contact metal and surface preparations have been published. References [28][29] report detailed survey of ohmic contacts to various III-V semiconductors.

Contact resistivity strongly depends on surface preparation [30] and obtaining resistivities $<1 \times 10^{-8} \Omega\text{-cm}^2$ requires a significant attention to removal of semiconductor surface oxides before the contacts are made. A $4.3 \times 10^{-8} \Omega\text{-cm}^2$ contact resistivity to n-InGaAs was achieved with Ti/Pt/Au layers by Ar^+ sputter cleaning the semiconduc-

tor surface before contact deposition [31]. Ti contacts diffuse [32] into InGaAs at high temperatures and hence can impair reliability [26], particularly in high- f_{max} devices, where semiconductor junctions typically lie within ≈ 20 nm of the contact surface. While ex-situ ohmic contacts can provide low resistivity, reproducibility is often problematic. Contact resistivity can be highly sensitive to surface preparation and to the time interval between the surface preparation and metal deposition, factors which may be difficult to control experimentally. In-situ contact formation prevents surface contamination and oxidation; metal is deposited on the semiconductor immediately after semiconductor growth without exposing the samples to air. Highly degenerate semiconductor doping is also desirable [14], as this decreases the contact barrier (depletion) thickness and increases tunneling probability.

For n-type InAs, contacts formed by ex-situ techniques have shown to result in $\rho_c = 2 \times 10^{-8} \Omega\text{cm}^2$ for $2 \times 10^{19} \text{cm}^{-3}$ active carrier concentration [33]. Ohmic contacts to GaAs and $\text{In}_{0.53}\text{Ga}_{0.47}\text{As}$ using an InAs cap layer have been studied extensively [33][34][35]. The contact resistance to GaAs (using an InAs cap layer) decreases on increasing the GaAs active carrier concentration because of the increased tunneling across the InAs/GaAs heterojunction [34]. The active carrier concentration in InAs was kept constant in these samples.

Ohmic contacts to p-type $\text{In}_{0.53}\text{Ga}_{0.47}\text{As}$ have been studied extensively because of its application as the base contacts in InP based HBTs. Ex-situ Pd/Ti/Pd/Au contacts

have shown $\rho_c = 4 \times 10^{-8} \Omega\text{-cm}^2$ to p-In_{0.53}Ga_{0.47}As [36][37], but penetrates into the semiconductor by combined chemical reaction and diffusion [38]. Low resistivity, thermally stable contacts having < 5 nm metal penetration depth are required for HBTs having < 20 nm thick base layers.

Apart from surface preparation, the interface conduction band barrier potential, determined either by Fermi level pinning or by work functions, also plays a crucial role in determining the contact resistance. For low resistance Ohmic contacts the Schottky barrier height at the metal-semiconductor interface should be as low as possible. A barrier height of approximately 0.2 eV was predicted from intrinsic interface state theory [18] for metal/n-InGaAs contacts. A barrier height of 0.5 eV was determined experimentally for contacts made to p-type InGaAs [39][40]. The low Schottky barrier height suggests that it should not be very difficult to prepare low resistivity contacts to nInGaAs. For InAs, the Fermi level is pinned in the conduction band [41][42] which makes it a potential candidate to be used as the contact layer for metal-semiconductor contacts.

1.5 Thesis Goal and Approach

1. **Ultra-low contact resistivity:** The primary goal of this thesis was to develop ultra low resistance ohmic contacts to n-type and p-type In_{0.53}Ga_{0.47}As for appli-

cation in sub-100 nm InGaAs/InP HBTs. n-type $\text{In}_{0.53}\text{Ga}_{0.47}\text{As}$ forms the emitter cap (on n-type InP) whereas p-type $\text{In}_{0.53}\text{Ga}_{0.47}\text{As}$ forms the base for the InP HBTs being developed in our group. Ohmic contacts to n-type InAs were also studied, as a potential capping layer over n-type $\text{In}_{0.53}\text{Ga}_{0.47}\text{As}$ /n-type InP.

Approach:

- (a) **High carrier concentration:** In order to obtain very low contact resistivities, it is important to have high active carrier concentrations in the semiconductor. High active carrier concentration reduces the Schottky barrier width in the semiconductor resulting in enhanced tunneling across the metal-semiconductor interface [14]. In this work, the semiconductor thin films were grown by molecular beam epitaxy technique and the high active carrier concentrations were achieved by optimization of growth conditions.
- (b) **Surface preparation:** The second approach was to prepare/clean the semiconductor surface before contact metal deposition. In this work three types of contacts, with different surface preparations, were studied:
 - i. In-situ contacts: For these type of contacts, the contact metal was deposited immediately after the MBE growth of the semiconductor thin film without ever exposing the semiconductor surface to air. This tech-

nique minimizes semiconductor oxidation and provides a clean metal-semiconductor interface.

- ii. Ex-situ contacts: For these type of contacts, the sample was first exposed to air. The semiconductor surface was then oxidized and chemically etched before contact metal deposition.
- iii. Quasi in-situ contacts: For these type of contacts, atomic hydrogen cleaning was utilized in addition to the techniques used for ex-situ contacts.

2. **Thermal Stability:** As mentioned before, these contacts were being developed for sub-100 nm devices. For these scaled devices, thermal stability of the metal-semiconductor interface is important for the long term reliability. Hence, the second goal of this thesis was to develop thermally stable metal contacts to n-type and p-type $\text{In}_{0.53}\text{Ga}_{0.47}\text{As}$ and n-type InAs .

Approach:

To obtain thermally stable metal-semiconductor contact with minimal or no intermixing at the interface, we chose tungsten (W), molybdenum (Mo) and iridium (Ir) as the contact metal. The melting points and work functions of these metals are listed in table 5.1.

Table 1.2: Refractory metal work functions and melting points

Metal	Work Function (eV)	Melting Point (°C)
W	4.5	3420
Mo	4.6	2620
Ir	5.7	2460

3. **Design of transmission line model (TLM) structures:** The third goal was to design TLM structures for accurate extraction of contact resistivities. Resistances extracted using previous TLM structures suffered from a huge component of metal resistance.

Approach: TLM structures were designed to minimize the component of parasitic metal resistance. Additionally, thicker metal was deposited for providing low resistance path for the current to flow from the contact pad to the semiconductor. This approach has been detailed in chapter ref.

4. **Development of theoretical model:** The final goal was to develop a theoretical model to compute the lower limits on the contact resistivities for n-type and p-type $\text{In}_{0.53}\text{Ga}_{0.47}\text{As}$ and n-type InAs .

Approach:

Lowest possible contact resistivities were calculated for different Schottky barrier heights and for various doping concentrations. Calculated values were compared

with experimental data. Calculations were also done to compute the lower limits on the contact resistivity for n-type and p-type GaAs, InP, GaSb and InSb.

1.6 Experimental Techniques

In this section, the experimental techniques used for the epitaxial thin film growth and characterization are discussed.

1.6.1 Thin Film Growth: Molecular Beam Epitaxy (MBE)

Molecular beam epitaxy (MBE) technique is a common method of growing epitaxial thin films of compound semiconductors. This technique was developed by Cho and Arthur in early 1970s [43][44]. Figure 1.8 shows the cross section of a typical MBE system. This technique involves interaction of one or several molecular or atomic beams on a surface of a heated crystalline substrate. MBE system consists of effusion cells with each cell containing one ultra-pure element. Each cell is covered with a shutter. For growing a film, effusion cells are heated to evaporate the source material and the shutters are utilized to control the thickness of the films. Further details about an MBE system can be obtained in reference [45]. The thin films studied in this work i.e. $\text{In}_{0.53}\text{Ga}_{0.47}\text{As}$ and InAs were grown on a Varian Gen-II solid source molecular beam

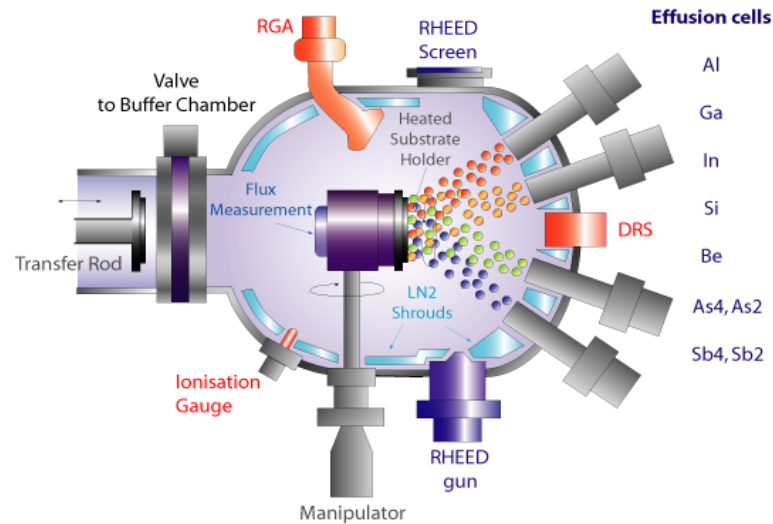


Figure 1.8: Schematic of a molecular beam epitaxy system [3].

epitaxy system. The sources available in this system were In, Ga, Al, As, Sb, Er, Be, Si, Te and C.

1.6.2 Film Characterization

Structural Characterization

Reflection High Energy Electron Diffraction (RHEED) RHEED is an in-situ growth monitoring tool in an MBE system. It can be used to monitor surface morphology during growth and calibrate growth rates. It is also useful during oxide desorption from a semiconductor surface and for determining growth kinetics. It consists of a RHEED gun which emits highly energetic (10-15 eV) electrons. These electrons strike

the semiconductor surface at a grazing angle. Electrons interact with the surface atoms resulting in a diffraction pattern which is recorded on a phosphor coated screen [9]. The position of the RHEED gun and the phosphor screen are shown in fig. 1.8. The type of pattern obtained on the screen gives information about the arrangement of atoms on the surface. In addition, the variation in the intensity of the specular spot on the screen can be calibrated to obtain growth rate of the film.

X-ray Diffraction (XRD) Since the goal of this work to develop ohmic contacts to $\text{In}_{0.53}\text{Ga}_{0.47}\text{As}$ layers for application to InP based HBTs, it was important to grow defect free $\text{In}_{0.53}\text{Ga}_{0.47}\text{As}$ films, lattice matched to InP. The stoichiometry of the grown films were verified by X-ray diffraction (XRD) technique. XRD was also used to estimate the amount of strain in degenerately doped thin films [46].

Atomic Force Microscopy Films were also characterized by atomic force microscopy (AFM) to study the RMS roughness of the films, especially for heavily doped films. For heavily doped p-type $\text{In}_{0.53}\text{Ga}_{0.47}\text{As}$ films, the dopant carbon tends to segregate and forms clusters deteriorating the rms roughness of the films.

Electrical Characterization

Hall Measurements To determine the active carrier concentrations, mobility and sheet resistance of the films, a combination of Hall and van der Pauw technique was used. According to van der Pauw, there are two characteristic resistances R_A and R_B ,

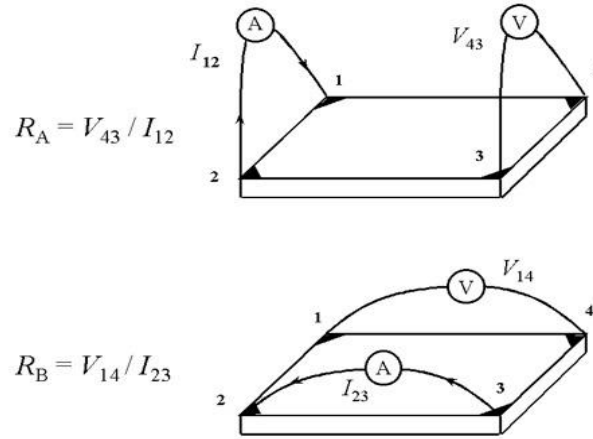


Figure 1.9: Schematic illustrating van der Pauw technique [4]

associated with the corresponding terminals shown in Fig. 1.9. van der Pauw equation (equation 1.11) relates R_A and R_B to the sheet resistance, R_s [4] [5].

$$\exp(-\pi R_A / R_s) + \exp(-\pi R_B / R_s) = 1 \quad (1.11)$$

Hall effect measurement is then used to calculate the sheet carrier density (n_s) and mobility (μ_s). Using the arrangement shown in figure 1.10, n_s , μ_s and R_s are related by equations 1.11, 1.12 and 1.13 [4][5].

$$n_s = IB / qV_H \quad (1.12)$$

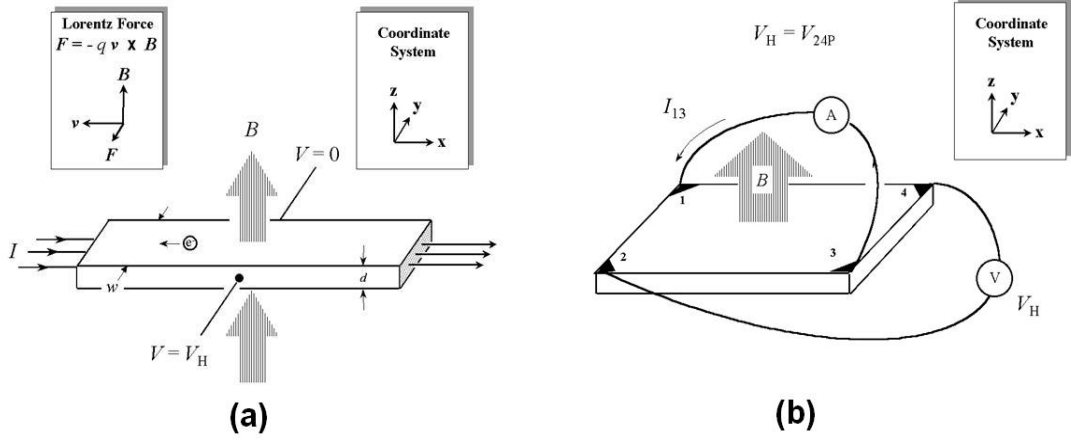


Figure 1.10: Schematic illustrating (a) Hall effect (b) sample geometry for n_s and μ_s measurements [4].

$$\mu = V_H / R_S I B = 1 / (q n_s R_s) \quad (1.13)$$

where I is the current and B is the magnetic field.

Capacitance-Voltage (CV) Measurements CV measurements were done on Schottky diodes made to n-type and p-type $\text{In}_{0.53}\text{Ga}_{0.47}\text{As}$ to calculate the barrier height [5].

The capacitance per unit area of a Schottky diode is given by:

$$C/A = \sqrt{\frac{\pm q \epsilon_s \epsilon_o (N_A - N_D)}{2 \pm V_{bi} \pm V - kT/q}} \quad (1.14)$$

where + sign is used for p-type ($N_A > N_D$) samples and – sign is used for n-type ($N_D > N_A$) samples. The barrier height and the built-in potential are related by:

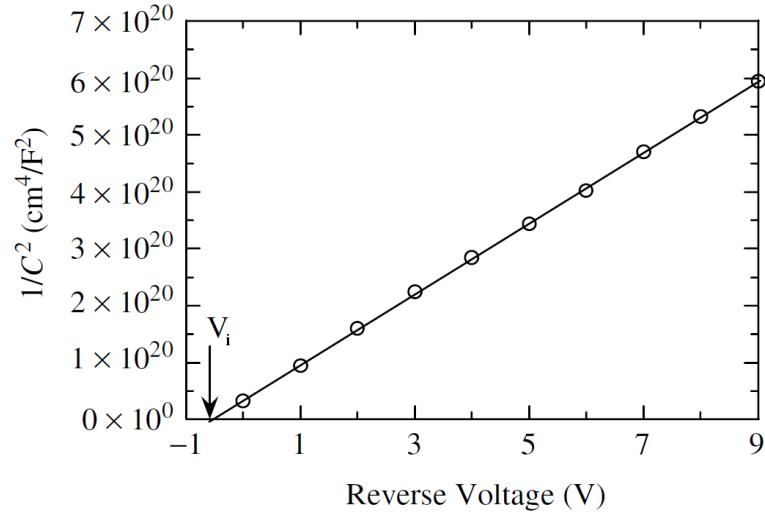


Figure 1.11: $1/C^2$ versus applied bias plot for ϕ_B measurement [5]

$$\phi_B = V_{bi} + V_o \quad (1.15)$$

$$V_o = (kT/q) \ln(N_v/N_A) \quad (1.16)$$

where N_v is the valence band density of states. By plotting $1/(C/A)^2$ against V , one obtains a curve with the intercept on voltage axis, $V_i = -V_{bi} + kT/q$.

The barrier height is then determined as:

$$\phi_B = -V_i + V_o + kT/q \quad (1.17)$$

The slope of curve can used to calculate the doping density by;

$$\text{slope} = 2/(2q\epsilon_s\epsilon_oN_A) \quad (1.18)$$

Chapter 2

Transmission Line Model (TLM) structures

In this work, the specific contact resistivity, ρ_c for metal-semiconductor contact was extracted using transmission line model (TLM) structures. The TLM method was developed by Berger [47]. Figure 2.1 shows the circuit diagram describing the metal-semiconductor contact. In the contact region, the current and the voltage differential equations are given by:

$$V'(x) = \frac{R_s}{W} I(x) dx \quad (2.1)$$

$$I'(x) = \frac{W}{\rho_c} V(x) dx \quad (2.2)$$

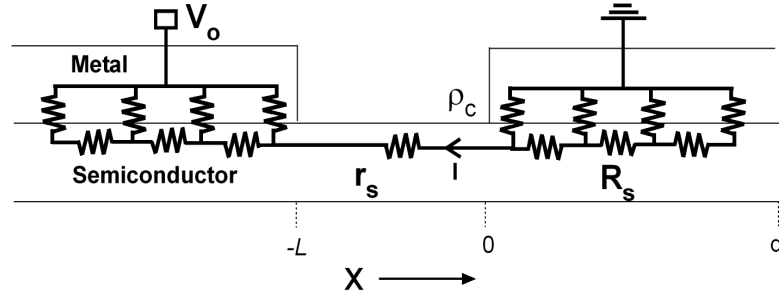


Figure 2.1: Cross-sectional circuit model for transmission line model structures

Combining equations 2.1 and 2.2 results in

$$d'' V(x) = \frac{R_s}{\rho_c} V(x) \quad (2.3)$$

The general solution for $V(x)$ and $I(x)$ are

$$V(x) = \frac{I L_T R_s}{W} \frac{\cosh \frac{d-x}{L_T}}{\sinh \frac{d}{L_T}} \quad (2.4)$$

$$I(x) = I \frac{\sinh \frac{d-x}{L_T}}{\sinh \frac{d}{L_T}} \quad (2.5)$$

where d is the total contact length, W is the contact width, I is the current flowing into the contact. The term $L_T = \sqrt{\rho_c / R_s}$ is known as the transfer length of the contact and is defined as the length over which the voltage drops by $1/e$ along the contact. The

total contact resistance is then given by

$$R_c = \frac{V(0)}{I(0)} = \frac{\sqrt{\rho_c R_s}}{W} \coth\left(\frac{d}{L_T}\right) \quad (2.6)$$

Usually, $d > 1.5L_T$, for which $\coth\left(\frac{d}{L_T}\right) \approx 1$. Therefore,

$$R_c = \frac{\sqrt{\rho_c R_s}}{W} \quad (2.7)$$

$$\rho_c \approx \frac{W^2 R_c^2}{R_s} \quad (2.8)$$

The resistances measured for a TLM structure with a gap, L_{gap} , between the contact metal pads follows the relation

$$R_{measured} = 2\rho_c/WL_T + R_s L_{gap}/W \quad (2.9)$$

Resistance measurement on TLM structures with different L_{gap} results in a plot shown in figure 2.2.

From equation 2.9

$$R_c = \rho_c/WL_T \quad (2.10)$$

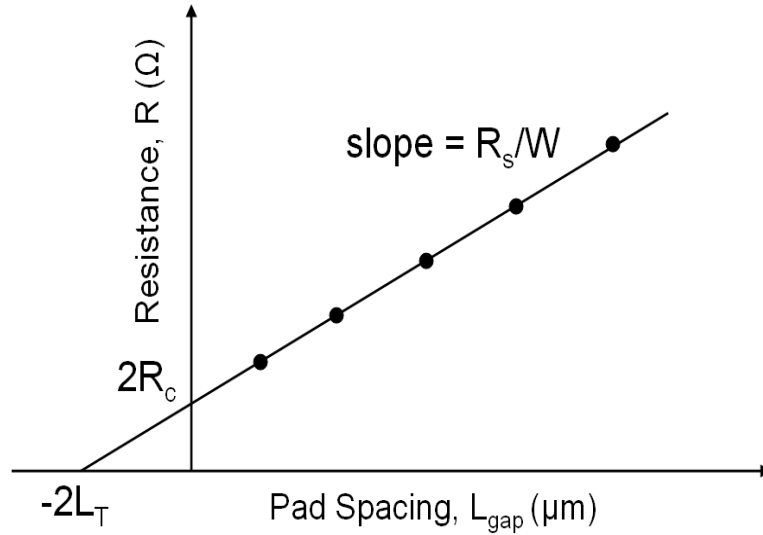


Figure 2.2: Variation of electron concentration and mobility with Si atomic concentration

$$slope = R_s L_{gap} / W \quad (2.11)$$

ρ_c can be calculated using equations 2.8, 2.10 and 2.11.

2.1 Design of TLM structures

Since the aim of this work was to develop ultra low resistance ohmic contacts, it was important to design test structures carefully to accurately determine the contact resistivity. In our test structures, we used separate pads for driving the current and for measuring the potential drop (four point probe measurement). This eliminates the

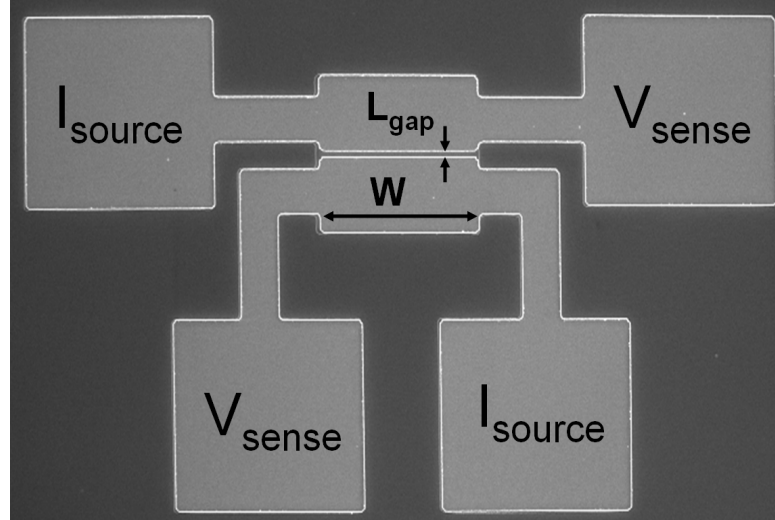


Figure 2.3: Scanning electron micrograph of the previous TLM structures used in our group.

parasitic resistances (probe as well as probe contact resistance) during measurement. However, it may still include the resistance due the metal. Figure ?? shows the TLM structures that were used previously for extracting the contact resistivity. For this TLM structure, the measured resistance,

$$R_{measured} = 2\rho_c/W L_T + R_s L_{gap}/W - R_m' \quad (2.12)$$

contains contribution contribution R_m' from the sheet resistivity (ρ_m/T_m) of the contact metal. Here ρ_c is the metal-semiconductor contact resistivity, R_s the semiconductor sheet resistivity, $L_T = \sqrt{\rho_c/R_s}$ the transfer length, ρ_m the bulk metal resistivity and T_m the contact metal thickness. The dimensions W and L_{gap} are defined in Fig 2.3.

In the previous publications from our group (references [48][49]), this metal resistance term (R_m') was ignored and erroneous contact resistivity values were reported. To remove any component of metal resistance, as indicated in figure 2.4, the potential drop must be measured at points close to the contact edges. Considering this requirement, TLM structures were re-designed to minimize the metal resistance component. Figure 2.5 shows the re-designed TLM structures used in this work. For this structure, the observed resistance,

$$R_{measured} = 2\rho_c/WL_T + R_sL_{gap}/W + R_m \quad (2.13)$$

contains a small contribution R_m from the sheet resistivity (ρ_m/T_m) of the contact metal. R_{metal} was determined from separate measurements of ρ_m/T_m and from numerical finite-element analysis of the contact geometry. For the narrow width ($W = 10 \mu\text{ m}$) test structures, metal R changes the contact resistivity data by less than 5 %. Note that the TLM geometry used here (Fig. 2) differs from that used in [50], and the associated metal R term reduced by over 4:1 for $W = 10 \mu\text{ m}$.

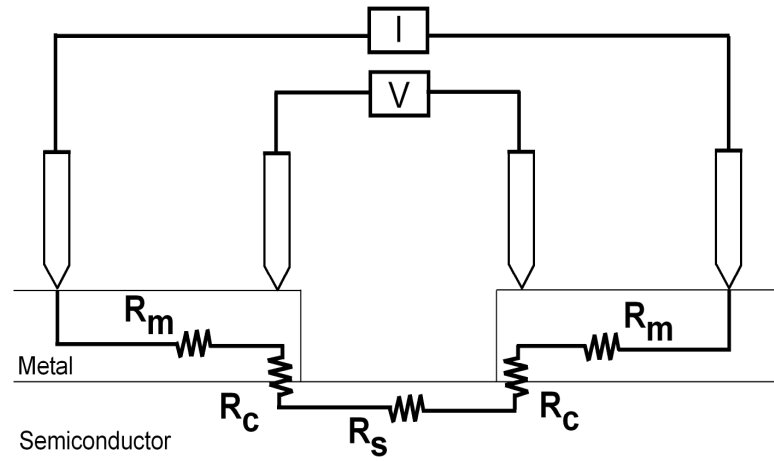


Figure 2.4: Four point probe measurement illustrating probe positioning for removing the component of metal resistance.

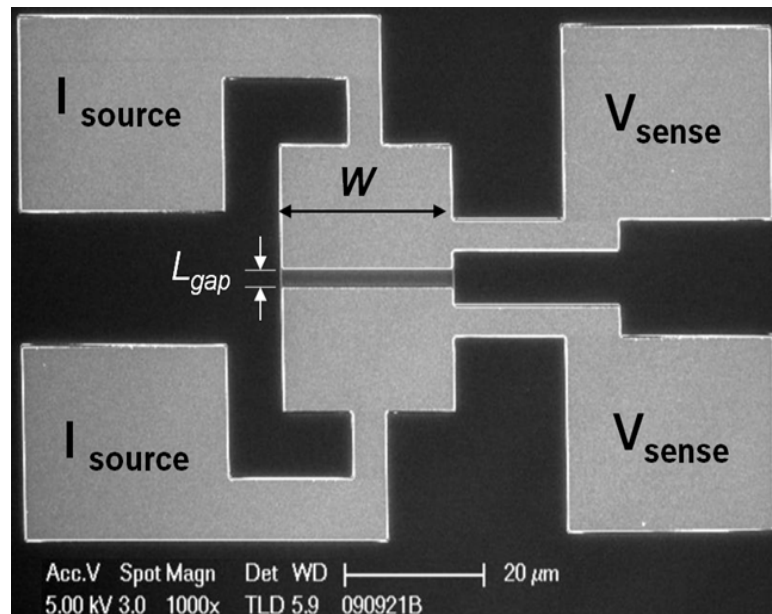


Figure 2.5: Scanning electron micrograph of the re-designed TLM structures used in this work.

2.2 Error Analysis

In this section we describe our method of estimating the errors involved in ρ_c calculations. These errors arise because of two factors. The first one is due to the resolution (dR) in the resistance measured by the parameter analyzer. To ascertain the value of dR, resistance measurements were done by keeping the probes in contact mode and making multiple measurements. Resistances were also measured by repeatedly lifting and contacting the measurement pads. The variation in the resistances measured by these techniques were found to vary by less than 0.01Ω . However, a safer value of $dR=0.02\Omega$ was assumed for the error analysis. The second factor is due to the resolution of the scanning electron microscope, dL, used for measuring L_{gap} . The resolution of the microscope, as specified by the manufacturer was 1.5 nm at > 10 kV, 2.5 nm at 1 kV, and 3.5 nm at 500 eV. However, for the error analysis, a resolution of $dL=20$ nm was assumed considering the non-uniformities along the metal semiconductor edge that could arise due to processing (fig. 2.6).

In addition, spreading of current occurs in the semiconductor, as shown in figure 2.7. To minimize the error in ρ_c extraction due to this spreading in current, resistance measurements were done on wider ($W = 25 \mu m$) TLM structures. For TLM structures with large width, the ratio of dW/W is smaller as compared to that for narrow width TLM structures, as can be seen in figure 2.8.

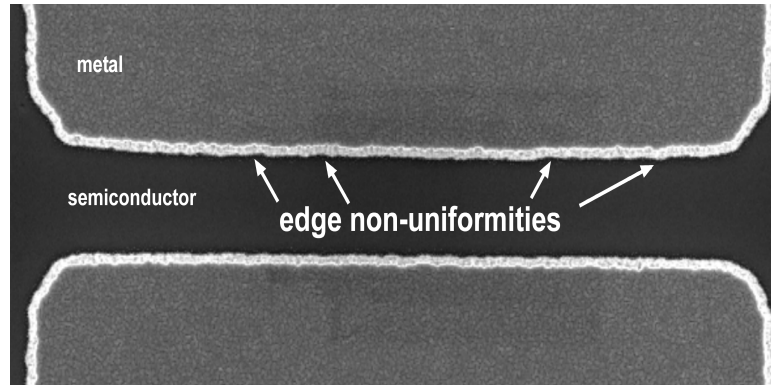


Figure 2.6: Scanning electron micrograph of the TLM structure. Non uniform edges are indicated by arrows.

Now, the linear fit for the plot shown in figure 2.2 can be expressed as:

$$R = a + cL \quad (2.14)$$

where a and c are the intercept and the slope of the curve, respectively.

$$\begin{bmatrix} R_1 \\ R_2 \\ \cdot \\ \cdot \\ R_n \end{bmatrix} = a + c \begin{bmatrix} L_1 \\ L_2 \\ \cdot \\ \cdot \\ L_n \end{bmatrix}$$

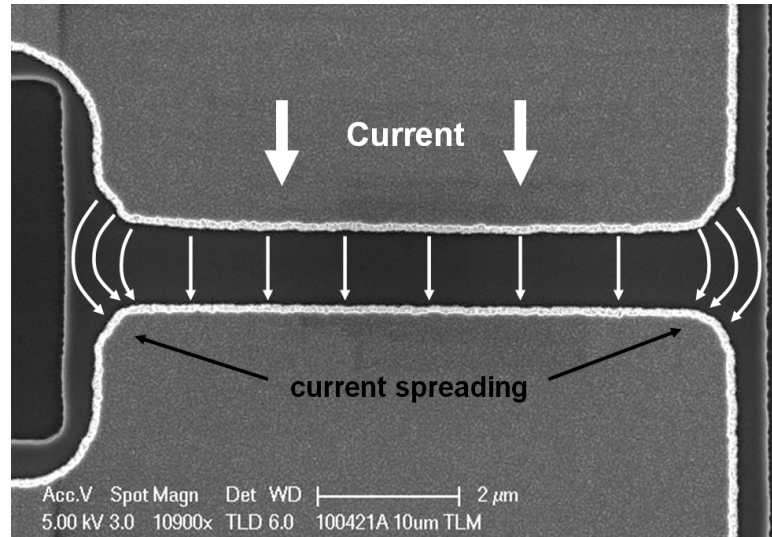


Figure 2.7: Scanning electron micrograph of the TLM structure indicating current distribution

$$\begin{bmatrix} R_1 \\ R_2 \\ \cdot \\ \cdot \\ R_n \end{bmatrix} = \begin{bmatrix} 1 & L_1 \\ 1 & L_2 \\ \cdot & \cdot \\ \cdot & \cdot \\ 1 & L_n \end{bmatrix} \begin{bmatrix} a \\ c \end{bmatrix}$$

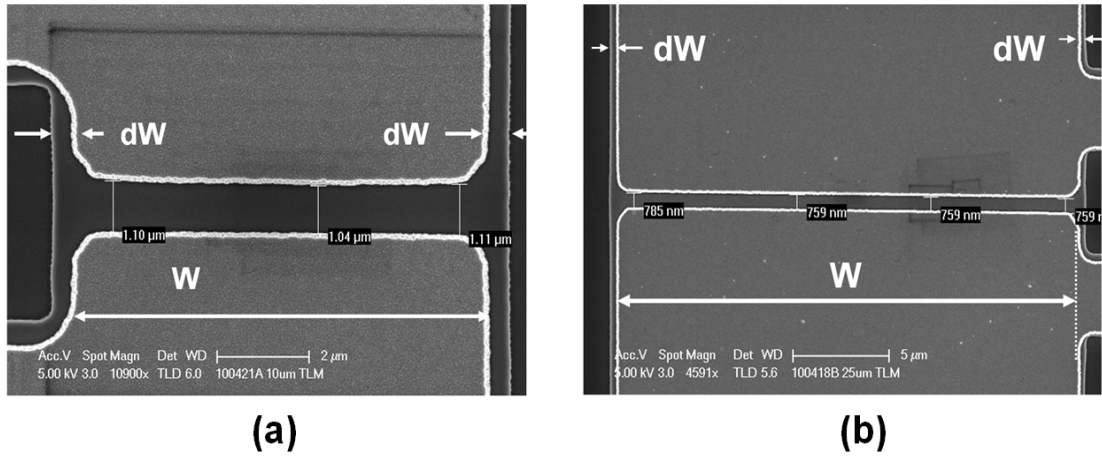


Figure 2.8: Scanning electron micrograph of the TLM structure indicating current distribution

$$Y = X \begin{bmatrix} a \\ c \end{bmatrix}$$

where,

$$X = \begin{bmatrix} 1 & L_1 \\ 1 & L_2 \\ \cdot & \cdot \\ \cdot & \cdot \\ 1 & L_n \end{bmatrix}, Y = \begin{bmatrix} R_1 \\ R_2 \\ \cdot \\ \cdot \\ R_n \end{bmatrix}$$

$$\begin{bmatrix} \hat{a} \\ \hat{c} \end{bmatrix} = (X^T X)^{-1} X^T Y$$

Hence, the best fit is given by

$$R = \hat{a} + \hat{c}L \quad (2.15)$$

Using similar formalism, the error in intercept, da and the error in slope, dc can be calculated as shown below.

$$dR = da + cdL + Ldc \quad (2.16)$$

or

$$\begin{bmatrix} dR_1 \\ dR_2 \\ \cdot \\ \cdot \\ dR_n \end{bmatrix} = \begin{bmatrix} 1 & L_1 \\ 1 & L_2 \\ \cdot & \cdot \\ \cdot & \cdot \\ 1 & L_n \end{bmatrix} \begin{bmatrix} da \\ dc \end{bmatrix} + c \begin{bmatrix} dL_1 \\ dL_2 \\ \cdot \\ \cdot \\ dL_n \end{bmatrix}$$

$$\begin{bmatrix} dR_1 \\ dR_2 \\ \cdot \\ \cdot \\ dR_n \end{bmatrix} - c \begin{bmatrix} dL_1 \\ dL_2 \\ \cdot \\ \cdot \\ dL_n \end{bmatrix} = X \begin{bmatrix} da \\ dc \end{bmatrix}$$

$$\begin{bmatrix} da \\ dc \end{bmatrix} = (X^T X)^{-1} X^T \left(\begin{bmatrix} dR_1 \\ dR_2 \\ \cdot \\ \cdot \\ dR_n \end{bmatrix} - c \begin{bmatrix} dL_1 \\ dL_2 \\ \cdot \\ \cdot \\ dL_n \end{bmatrix} \right)$$

Here, $dR_1 = dR_2 = \dots = dR_n = dR = \pm 0.02 \Omega$ and $dL_1 = dL_2 = \dots = dL_n = dL = \pm 20 \text{ nm}$

$$\begin{bmatrix} da \\ dc \end{bmatrix} \leq (X^T X)^{-1} X^T \left(\begin{bmatrix} dR_{1,v} \\ dR_{2,v} \\ \cdot \\ \cdot \\ dR_{n,v} \end{bmatrix} - c \begin{bmatrix} dL_{1,v} \\ dL_{2,v} \\ \cdot \\ \cdot \\ dL_{n,v} \end{bmatrix} \right)$$

where $dR_{n,v}$ and $dL_{n,v}$ can be positive or negative. Depending on the sign of an element in $(X^T X)^{-1} X^T$, the sign of $dR_{n,v}$ and $dL_{n,v}$ is chosen such that the value of da and dc is maximized. Based on these calculations, the maximum and the minimum values of the slope and intercept are obtained. These values (plotted in figure 2.9), are then used for calculating the minimum and maximum ρ_c using equation (2.8).

$$\hat{a} - da \leq a \leq \hat{a} + da \quad (2.17)$$

$$\hat{c} - dc \leq c \leq \hat{c} + dc \quad (2.18)$$

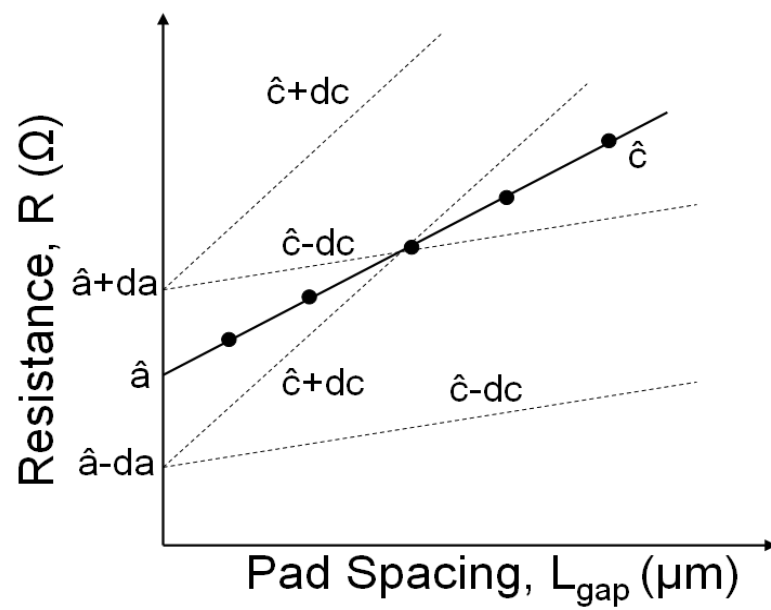


Figure 2.9: Illustration of 'worst case' fit obtained for various combinations of slopes and intercepts.

Chapter 3

n-InGaAs: Epitaxial Growth and Ohmic Contacts

In this chapter, the experimental details of the epitaxial growth of n-type InGaAs and the characterization of electron concentration is presented. The contact resistivities obtained for molybdenum (Mo) contacts made to the degenerately doped epilayers is discussed. Various surface preparations before forming the metal contact are also detailed.

3.1 Doping Calibrations

The primary aim of this study was to achieve as high electron concentration as possible by calibrating the growth conditions. It was achieved by optimizing three parameters during MBE growth:

1. Dopant flux

2. Arsenic flux

3. Substrate temperature

3.1.1 Dopant flux calibration

A set of samples were grown using Si cell at various temperatures, keeping a constant substrate temperature (460° C) and As flux (5×10^{-6} Torr). As shown in fig 3.1, for silicon concentration $\leq 2 \times 10^{19} \text{ cm}^{-3}$, the electron concentration increases linearly with increase in Si flux but saturates at higher Si concentrations because of amphoteric nature of Si. The highest electron concentration obtained through this calibration was $5 \times 10^{19} \text{ cm}^{-3}$ at a total silicon concentration of $2 \times 10^{20} \text{ cm}^{-3}$.

3.1.2 Arsenic flux calibration

To calibrate the arsenic flux, another set of samples were grown at various arsenic fluxes, keeping a constant substrate temperature and Si cell temperature. As shown in fig 3.2, the As flux was varied from 3×10^{-6} Torr to 14×10^{-6} Torr. The substrate temperature and the total Si concentration was maintained at 460° C and 10^{20} cm^{-3} , respectively. It was observed that the electron concentration increased with the increase in arsenic flux during growth. This is because the number of arsenic vacancies are reduced at higher arsenic fluxes. Hence the probability of Si atoms occupying the arsenic vacancies is reduced resulting in less autocompensation [51].

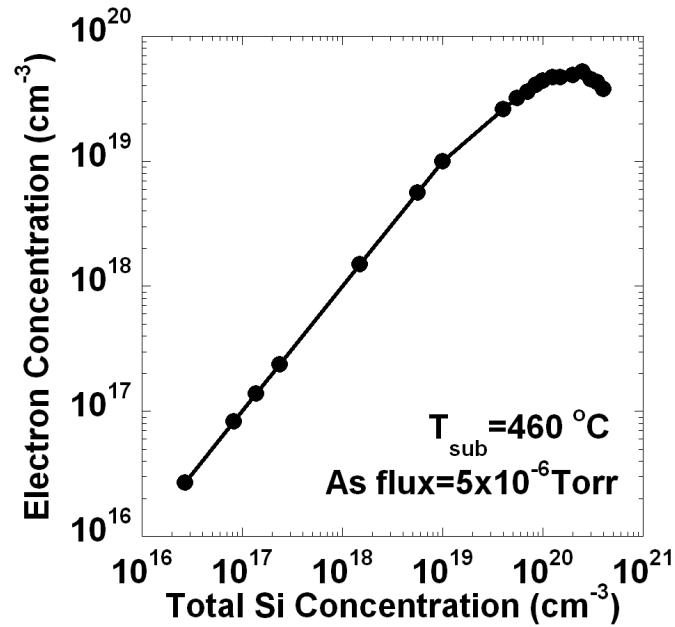


Figure 3.1: Variation of electron concentration with total silicon concentration for samples grown at a substrate temperature of 460 °C and at an As flux of 5×10^{-6} Torr.

3.1.3 Growth temperature calibration

During this calibration, the substrate temperature was varied from 300 °C to 460 °C. The arsenic flux and total Si concentration was kept constant at 14×10^{-6} Torr and $1.5 \times 10^{20} \text{ cm}^{-3}$, respectively. The electron concentration was found to increase as the substrate temperature was reduced (fig 3.3). This is because the sticking coefficient of As is increased at lower substrate temperatures thereby reducing the number of As vacancies, hence lower autocompensation [51].

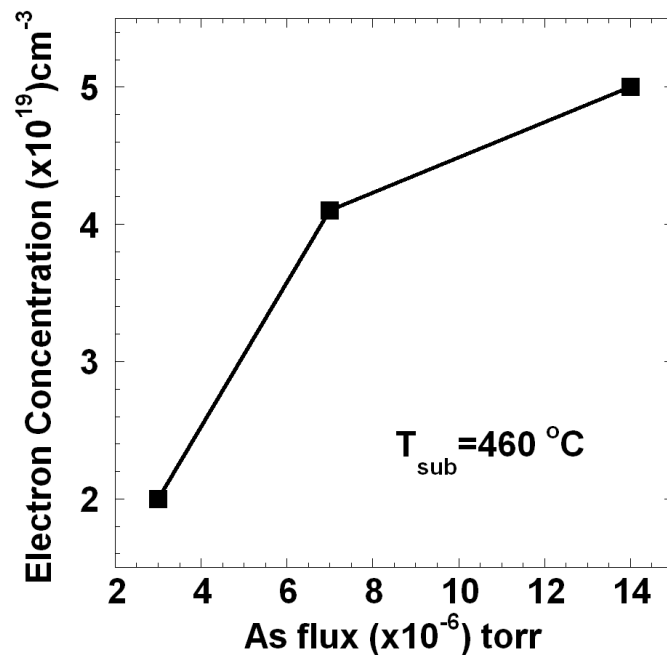


Figure 3.2: Variation of electron concentration with arsenic flux for samples grown at a substrate temperature of 460 ° C.

Fig 3.4 shows the variation of electron concentration with the total Si concentration for samples grown at various substrate temperatures. It can be clearly seen that the samples grown at lower temperatures had higher electron concentration. An electron concentration as high as $7.2 \times 10^{19} \text{ cm}^{-3}$ was also obtained at a substrate temperature of 360 °C and for a total Si concentration of $1.5 \times 10^{20} \text{ cm}^{-3}$. But the Si cell used for these growths had to be removed for maintenance and the results were not reproduced with the replacement cell.

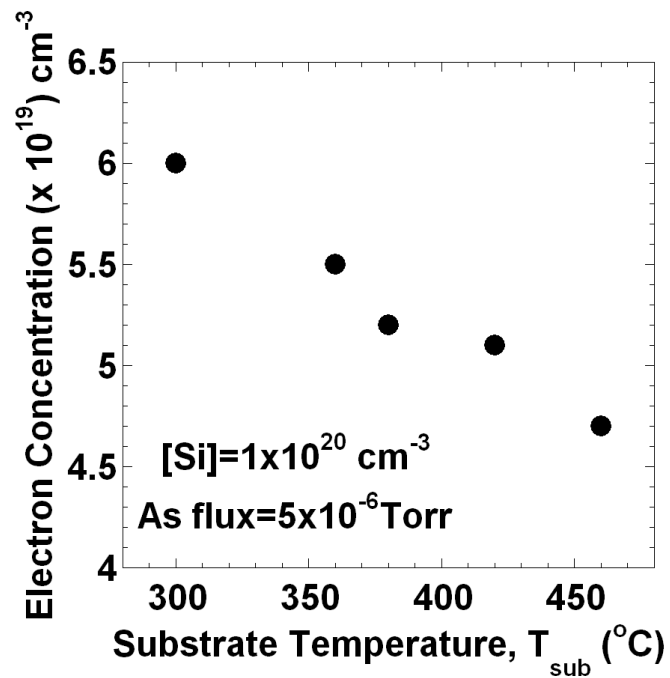


Figure 3.3: Variation of electron concentration with substrate temperature.

Based on these calibrations, an electron concentration of $6 \times 10^{19} \text{ cm}^{-3}$ was obtained consistently at a substrate temperature of 300°C , As flux of 14×10^{-6} Torr and a total Si concentration of $2 \times 10^{20} \text{ cm}^{-3}$. Fig 3.5 shows the variation of mobility with electron concentration for the samples grown at three different temperatures. The mobility was found to drop as the electron concentration increased [52].

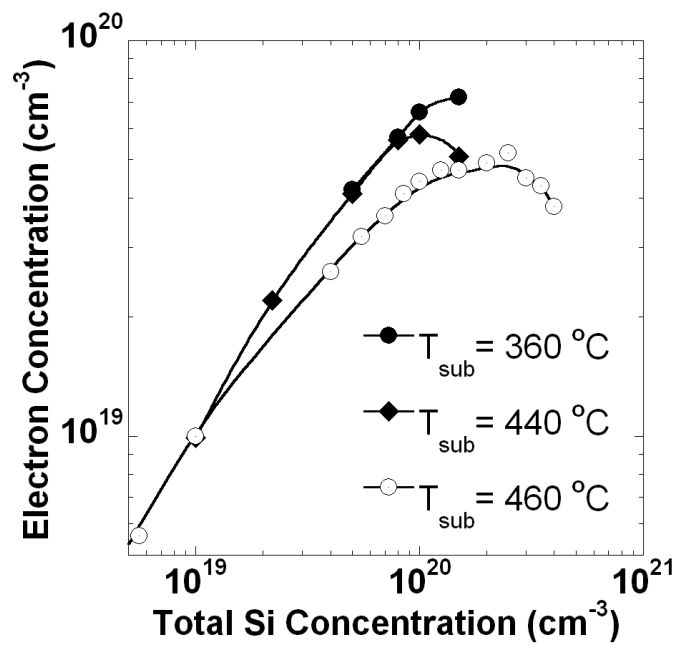


Figure 3.4: Variation of electron concentration with the total Si concentration for samples grown at various substrate temperatures.

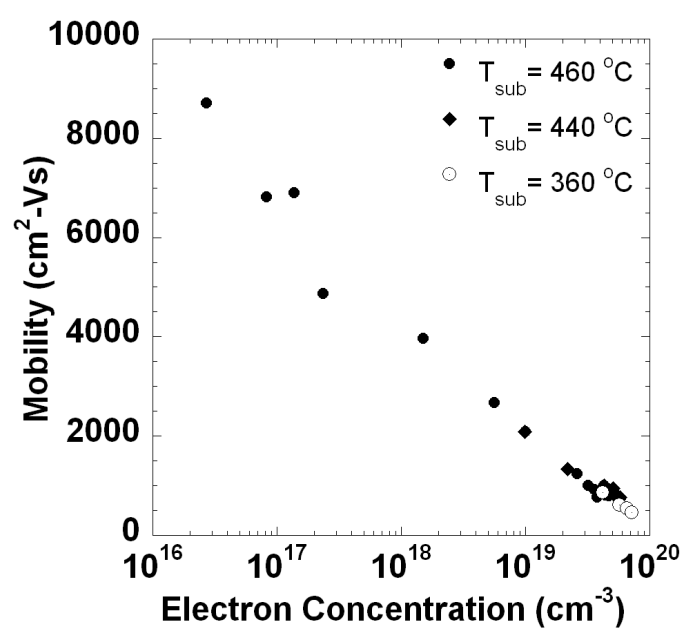


Figure 3.5: Variation of mobility with electron concentration for the samples grown at three different temperatures.

3.2 Ohmic Contacts

After the electron concentration was optimized, metal contacts were formed on n-type InGaAs epilayers. The contacts were formed by three techniques as discussed below:

3.2.1 In-situ contacts

For making in-situ contacts, the contact metal was deposited immediately after the MBE growth of the semiconductor thin film without ever exposing the semiconductor surface to air. For this, the samples were transferred under ultra high vacuum to the electron beam metal deposition chamber. Contact metal was deposited on half the wafer through a shadow mask. The active carrier concentration, mobility, and sheet resistance were obtained from Hall measurements by placing indium (In) contacts on samples taken from the half of the wafer not coated with metal. The portion of the wafer coated with metal was processed into transmission line model (TLM) structures for contact resistance measurement. Doping concentration was thus measured on pieces of the same growth samples as those used for resistance measurement; this avoids experimental errors resulting from variation in doping concentration between growth samples. After the metal contacts were formed, the samples were processed into transmission line model structures using the process described in chapter 2

Figure 3.6 shows specific contact resistivity and the total active carrier concentration as a function of the total incorporated Si dopant concentration. These InGaAs samples were grown at 440 °C substrate temperature. For dopant concentrations below $8 \times 10^{19} \text{ cm}^{-3}$, electron concentration increases with increase in Si dopant concentration, while contact resistivity decreases rapidly. For 440 °C growth, the lowest observed contact resistivity was $(1.6 \pm 0.9) \times 10^{-8} \Omega - \text{cm}^2$ for an active carrier concentration of $4.2 \times 10^{19} \text{ cm}^{-3}$. Note that the contact resistivity obtained by Singisetti et al [49] was $(2.0 \pm 0.9) \times 10^{-8} \Omega - \text{cm}^2$ (after correcting for metal resistance) for an active carrier concentration of $3.5 \times 10^{19} \text{ cm}^{-3}$. InGaAs was grown at 460 °C for these samples. Noting that the lowest contact resistivity, $(1.1 \pm 0.6) \times 10^{-8} \Omega - \text{cm}^2$, was obtained at the highest active carrier density ($6 \times 10^{19} \text{ cm}^{-3}$, 420 °C growth), we speculate that increasing the ionized donor concentration decreases the Schottky barrier thickness, increasing the probability of tunneling through the junction.

To study the effect of total Si concentration on contact resistivity, a series of samples were grown with the total Si concentration varying from $4 \times 10^{19} \text{ cm}^{-3}$ to $4 \times 10^{20} \text{ cm}^{-3}$. The electron concentration and the contact resistivity obtained for these samples are plotted in fig 3.7 with respective total Si concentration. Error bars are indicated on each data point for contact resistivity. It can be seen that as the total Si concentration increases, the contact resistivity continues to drop even though the electron concentration decreases at higher Si concentration. This could be attributed to band gap narrowing

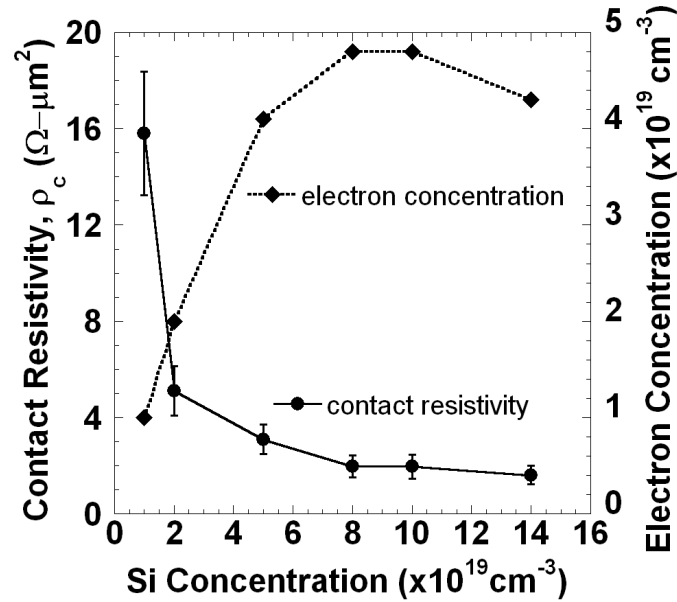


Figure 3.6: Variation of contact resistivity and electron concentration with total Si concentration.

of semiconductor due to heavy doping. As shown in figure 3.8 [6], the impurities form an energy band at sufficiently high carrier concentrations [6] and at low temperatures, carriers can travel in this band without entering the conduction band [11] [53]. At very high doping concentrations, the donor energy band and the conduction band could merge resulting in band gap shrinkage. Li et al [7] have calculated the band gap narrowing for n-type InGaAs (figure 3.9). It has also been mentioned in ref. [7] that, due to band gap narrowing, the effective barrier height at the metal semiconductor is reduced which results in enhanced tunneling across the junction. However, no supporting experimental data was provided. Apart from the donor states, for GaAs, it

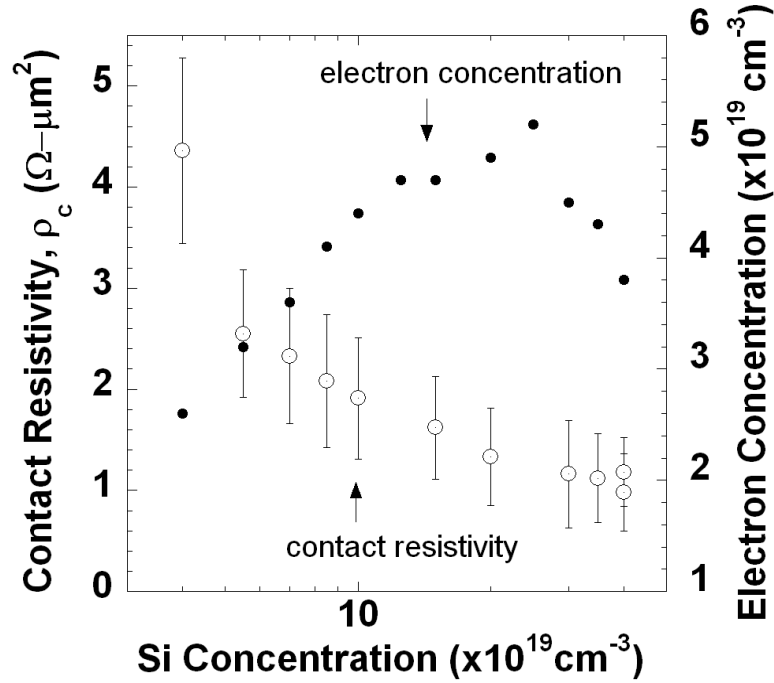


Figure 3.7: Variation of contact resistivity and electron concentration with total Si concentration. Error bars are indicated on respective contact resistivity values.

has been shown that heavy Si doping results in additional states in the band gap which could be due to Si acceptors, neutral Si donor-acceptor pairs and Si-complex (Si-X), possibly a Ga vacancy Si complex [54]. We speculate presence of similar defects in Si doped InGaAs provides additional paths for the electron to travel across the metal semiconductor interface.

Samples were also prepared with W as the contact metal. For comparison, Mo and W metals were deposited on the same sample using a shadow mask. The electron concentration, mobility and sheet resistance (for 100 nm thick film) for nInGaAs was

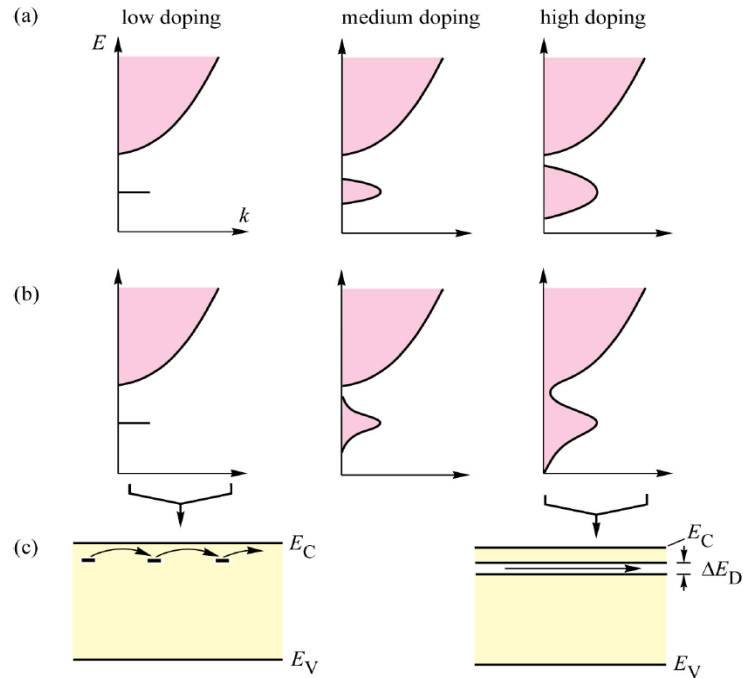


Figure 3.8: Donor impurity level and donor impurity band at low, medium and high doping concentrations for (a) an ordered impurity distribution and (b) a random impurity distribution. (c) Band diagram illustrating hopping conduction and impurity band conduction (from Schubert [6]).

$5.4 \times 10^{19} \text{ cm}^{-3}$, $517.8 \text{ cm}^2/\text{Vs}$ and $21 \text{ } \Omega/\text{sqr}$, respectively. The contact resistivity obtained with W as the contact metal was $(1.9 \pm 0.9) \times 10^{-8} \text{ cm}^2$, which is slightly higher than the contact resistivity for Mo $((1.4 \pm 0.9) \times 10^{-8} \text{ cm}^2)$. We speculate this could be because of the difference in Schottky barrier height for Mo and W. In an attempt to measure the Schottky barrier height, metal contacts formed to a very low doped ($5 \times 10^{16} \text{ cm}^{-3}$) sample were found to be non-rectifying. Hence no conclusive data was obtained.

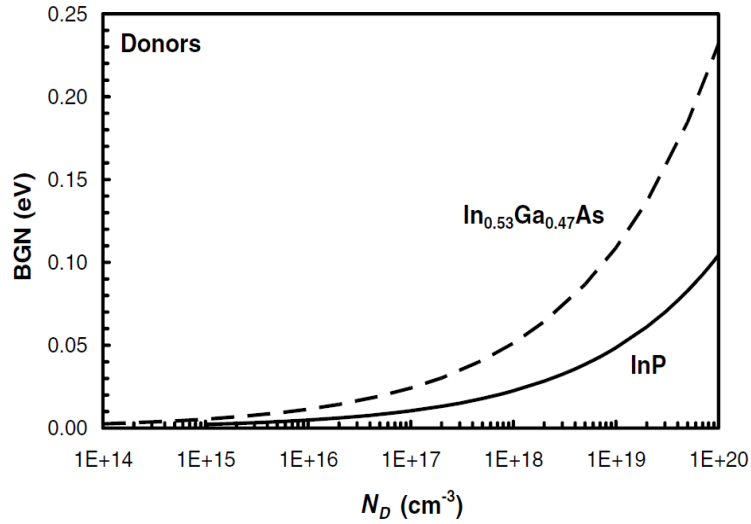


Figure 3.9: Band gap narrowing resulting from high donor in InP (solid) and $\text{In}_{0.53}\text{Ga}_{0.47}\text{As}$ (dashed) [7].

Extraction of the specific contact resistivity ρ_c from the observed lateral access resistivity ρ_H and semiconductor sheet resistivity ρ_s is only accurate if the semiconductor sheet resistivity in regions below the ohmic contacts is the same as that in the space between the contacts. In the fabrication of the TLM test structures reported here, the surface of the semiconductor between the contacts is exposed to the SF_6 /Ar plasma dry etch which removes the Mo contact metal. To verify that this exposure does not significantly change the sheet resistance, two InGaAs samples were grown by MBE. 14.1Ω sheet resistance was measured by Hall method on the control sample. On the second (test) sample, in situ Mo was first deposited by evaporation and removed by SF_6 /Ar plasma dry etching; this showed 14.5Ω sheet resistance.

3.2.2 Ex-situ contacts

For these type of contacts, the sample was first exposed to air (as it would normally happen in any device fabrication process flow). The semiconductor surface was then oxidized with UV-ozone for 10 minutes and then treated with 10% HCl for 1 minute [30]. UV-ozone treatment oxidizes defect causing species (such as elemental As, organic impurities) at the surface [55] [56], which can be easily removed by subsequent etching. Also, UV-ozone plus oxide removal results in a stoichiometric semiconductor surface [55] [56]. After the UV-ozone and oxidal removal, the samples were then immediately loaded in an e-beam metal deposition chamber. 20 nm of molybdenum was deposited on the semiconductor surface at a growth rate of $0.5 \text{ \AA}/s$. The samples were then processed into TLM structures. The observed ρ_c was $(1.5 \pm 1.0) \times 10^{-8} \text{ cm}^2$ for samples with an electron concentration of $5.5 \times 10^{19} \text{ cm}^{-3}$. This ρ_c is higher than that obtained for in-situ contacts ($\rho_c = (1.1 \pm 0.6) \times 10^{-8} \text{ } \Omega\text{-cm}^2$) for similar electron concentrations. This indicates that there might still be some oxide layer present on the semiconductor after UV-ozone + dil. HCl treatment.

3.2.3 Quasi-insitu contacts

For these type of contacts, similar to ex-situ type, the samples were first exposed to air, oxidized in UV-ozone and treated with dil. HCl. The samples were then loaded in MBE system where they were exposed to thermally cracked H for further oxide re-

removal. (Treatment with atomic H results in atomically clean surfaces, which been confirmed with reflection high energy electron diffraction (RHEED)[57][58][59]. Atomic H has been used to clean surfaces prior to semiconductor regrowth [60] by molecular beam epitaxy (MBE). Atomic H cleaning is carried out at lower temperatures than conventional thermal oxide desorption and hence causes less surface roughening due to less group V desorption. The samples were exposed to thermally cracked H for times ranging from 20 to 40 min and temperatures ranging from 375 to 420 °C. The filament temperature of the H cracking cell was maintained at 2200 °C. The chamber pressure during H cleaning was maintained at 10^{-6} Torr. RHEED patterns were recorded along the (110) and ($\bar{1}10$) azimuths after H cleaning. The samples were then transferred to the electron beam evaporator where 20 nm Mo was deposited.

As the samples were exposed to atomic H and the exposure time and temperature are increased, a gradual improvement from a (1×1) to a (2×4) reconstruction was observed. Figure 3.10 shows the RHEED patterns recorded along the (110) and ($\bar{1}10$) azimuths after 40 min of atomic H exposure at 420 °C. The observed (2×4) reconstruction indicates an As-rich or As-terminated surface [61][9][62].

From the TLM data, $\rho_c = (1.1 \pm 0.9) \times 10^{-8} \text{ cm}^{-3}$ was determined for samples with UV-ozone+HCl+H treatment. The contact resistivity here obtained is the lowest reported to date for contacts made to nInGaAs after surface preparation and it is comparable to ρ_c obtained for in situ Mo contacts [50].

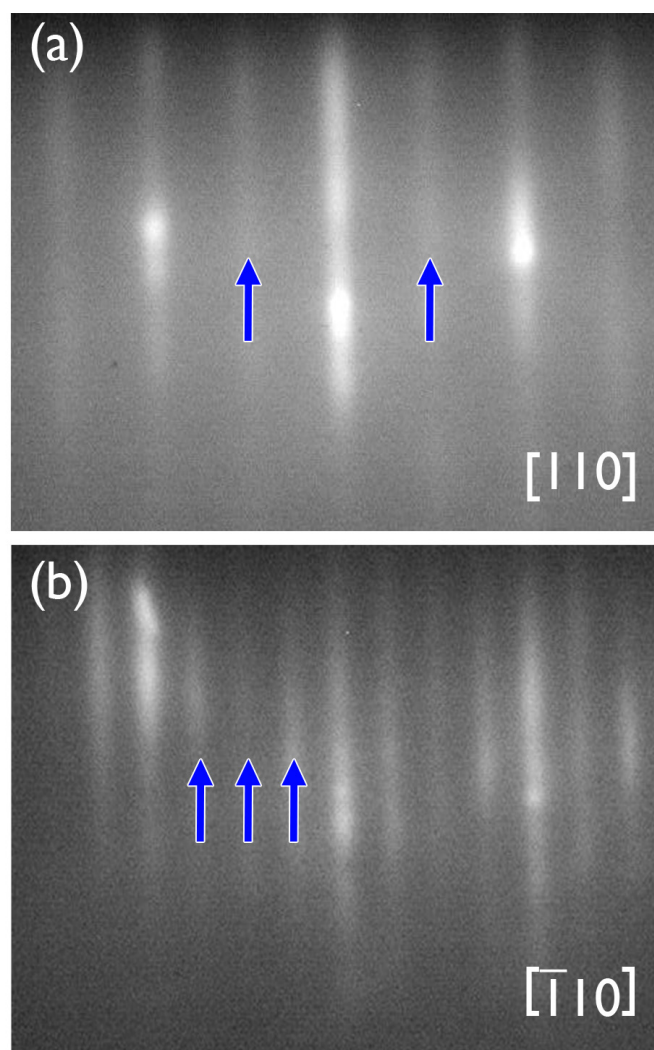


Figure 3.10: RHEED patterns of the atomic H cleaned sample along the (110) and $(\bar{1}10)$ azimuths showing (2×4) reconstructed surface.

For the TLM structures, the transfer length was found to be 280 nm, 2.8 : 1 larger than the $n+$ layer thickness; hence, the resistance analysis assuming that one-dimensional current flow is appropriate [63]. Hall measurements on the samples indicate an active carrier concentration, a mobility, and a sheet resistance of $4.8 \times 10^{19} \text{ cm}^{-3}$, $984 \text{ cm}^2/\text{Vs}$, and $13 \text{ } \Omega/\text{sqr}$, respectively. The sheet resistance obtained with TLM measurements was $13.5 \text{ } \Omega/\text{sqr}$, which closely correlates with the sheet resistance obtained with Hall measurement.

In separate experiments, samples doped at $5 \times 10^{19} \text{ cm}^{-3}$ were exposed to air for 2, 36, and 395 days, and treated with UV-ozone+HCl+H. Mo was deposited and TLM structures were fabricated on these samples. Observed ρ_c were 1.1, 1.1, and $1.0 \text{ } \Omega - \mu\text{m}^2$, respectively. A separate set of samples, doped at $5 \times 10^{19} \text{ cm}^{-3}$, exposed to air for 2 and 395 days, was treated with UV-ozone+HCl. Mo contacts were formed and TLM structures were fabricated on these samples. Observed ρ_c were 1.4 and $1.5 \text{ } \Omega - \mu\text{m}^2$, respectively. These data indicate that the duration of air exposure has little effect on ρ_c given the surface preparation procedures employed.

Chapter 4

n-InAs: Thin Film Growth and Ohmic Contacts

As mentioned previously, the interface conduction band barrier potential, determined either by Fermi level pinning or by work functions, also plays a crucial role in determining the contact resistance. For InAs, the Fermi level is pinned in the conduction band [41] [42] which makes it a potential candidate to be used as the contact layer for metal-semiconductor contacts. Ex-situ, annealed, contacts to InAs with $2 \times 10^{19} \text{cm}^{-3}$ electron concentration have shown to result in $\rho_c = 2 \times 10^{-8} \Omega\text{-cm}^2$ [33]. Ohmic contacts to GaAs and $\text{In}_{0.53}\text{Ga}_{0.47}\text{As}$ using an InAs cap layer have been studied extensively [33] [34] [35]. The contact resistance to GaAs (using an InAs cap layer) decreases on increasing the GaAs electron concentration because of the increased tunneling across the InAs/GaAs heterojunction [34]. The electron concentration in InAs was kept constant in these samples. However, there have been no reports on the effect of InAs electron concentration on ρ_c . In this chapter, we present growth calibrations

for obtaining high electron concentration in InAs. We also present ultra-low contact resistivity for contacts made to n-InAs and the dependence of ρ_c on InAs electron concentration.

4.1 n-InAs growth and doping calibrations

InAs samples were grown on InP substrates. A buffer layer of 100 nm thick $\text{In}_{0.53}\text{Al}_{0.47}\text{As}$ was grown on thermally desorbed InP substrates. 100 nm thick, Si doped InAs layer was then grown on the InAlAs layer. Due to the large lattice mismatch between InAlAs and InAs ($\approx 4\%$), the InAs layer is completely relaxed. A 4×2 RHEED reconstruction was observed during the growth of InAs.

Similar to nInGaAs samples, nInAs doping calibrations were done using various Si cell temperatures and substrate temperatures. However, the range of As flux was found to be narrow for the growth of good quality InAs films (5×10^{-7} Torr to 1.5×10^{-6} Torr). The results of doping calibrations are shown in figure 4.1. In this case also, the electron concentration saturates at higher Si concentration because of austocompensation behavior of Si. As can be seen in fig 4.1, the mobility continues to drop as the electron increases. Also, the electron concentration was found to increase as the substrate temperature was reduced till 380 °C (fig. 4.2). However, a sample grown at 305 °C substrate temperature showed a decrease in electron concentration. This drop could

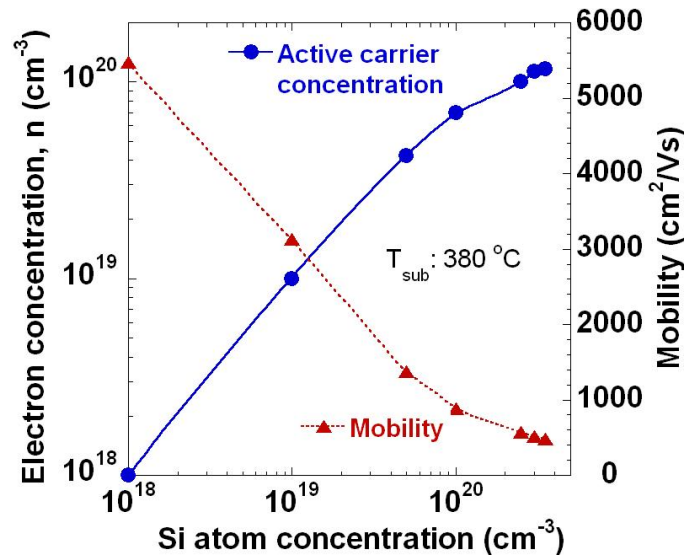


Figure 4.1: Variation of electron concentration and mobility with Si atomic concentration

be because of excess As incorporation resulting in anti-site defects (since the sticking coefficient of As increases as the substrate temperature is reduced). The highest electron concentration achieved after these calibrations was $1.2 \times 10^{20} \text{cm}^{-3}$ for a total Si atom concentration of $3.5 \times 10^{20} \text{cm}^{-3}$, with an As flux of 8×10^{-7} Torr and at a substrate temperature of 380°C . The mobility and sheet resistance for this sample was $635 \text{cm}^2/\text{Vs}$ and $9.8 \Omega/\text{sqr}$, respectively.

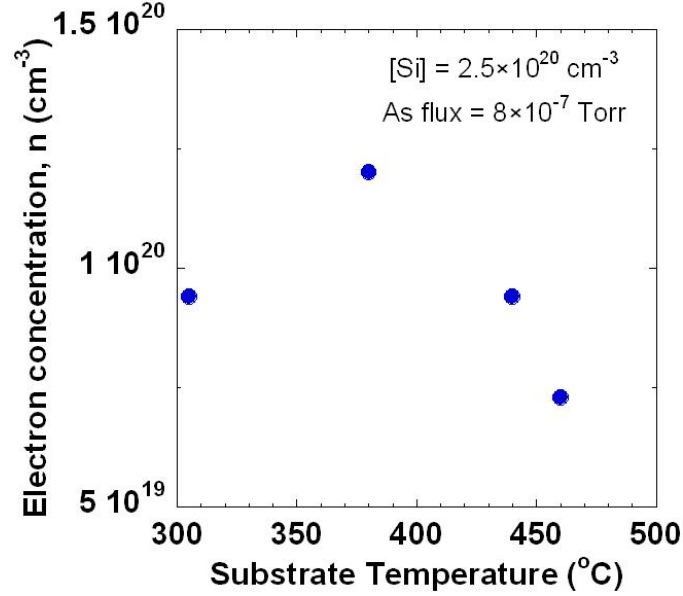


Figure 4.2: Variation of electron concentration with substrate temperature.

4.2 Ohmic Contacts

After the doping calibrations, contact metal, Mo, was deposited on semiconductor surface using in-situ and ex-situ technique (as explained in section 3.2). Contact resistances were measured and contact resistivities are extracted for a series of samples. Fig 4.3 shows ρ_c as a function of active carrier concentration. For active carrier concentration below $8.2 \times 10^{19} \text{cm}^{-3}$, ρ_c decreases with increase in the active carrier concentration and saturates for an active carrier concentration greater than $8.2 \times 10^{19} \text{cm}^{-3}$. This indicates that, although the Fermi level pins in the conduction band for InAs, an active carrier concentration greater than $4 \times 10^{19} \text{cm}^{-3}$ is required to obtain ρ_c less

than $1 \times 10^{-8} \Omega - cm^2$. The lowest ρ_c extracted from the TLM measurements was $(0.6 \pm 0.4) \times 10^{-8} \Omega - cm^2$ for the sample with an active carrier concentration of $8.2 \times 10^{19} cm^{-3}$. For this sample, the variation of TLM test structure resistance with contact separation is shown in Fig. 4.4. Note that after correcting for the effect of TLM test structure interconnect resistance on measurements [50], we had earlier obtained $\rho_c = (1.4 \pm 0.5) \times 10^{-8} \Omega - cm^2$ for in-situ Mo contacts to a composite layer of 5 nm of n-type InAs on 95 nm of InGaAs [49]. For this sample, the active carrier concentration in the InAs layer was $3 \times 10^{19} cm^{-3}$ (calibrated on separate samples). As shown in Fig. 4.3, ρ_c reported for InAs (5 nm) /InGaAs (95 nm) sample of ref. [49] is greater than expected from the current data because the observed resistivity includes Mo/InAs and InAs/InGaAs interfaces in series. Also shown in Fig. 4.3 is the ρ_c obtained with exsitu, annealed, contacts to InAs (Shiraishi et. al.), which is greater than for in-situ contacts.

For the Mo contacts made by ex-situ technique, a contact resistivity of $(0.7 \pm 0.5) \times 10^{-8} \Omega - cm^2$ was obtained for the sample with $8.2 \times 10^{19} cm^{-3}$ electron concentration. This contact resistivity is comparable to that obtained by in-situ technique indicating the effectiveness of the surface cleaning procedure.

For the sample with $\rho_c = (0.6 \pm 0.4) \times 10^{-8} \Omega - cm^2$ the transfer length was 260 nm, 2.6:1 larger than the n+ layer thickness; hence resistance analysis assuming one dimensional current flow is appropriate. Hall measurements on the same sample with lowest contact resistivity indicate $568 cm^2/Vs$ mobility, and $10.5 \Omega/sqr$ sheet

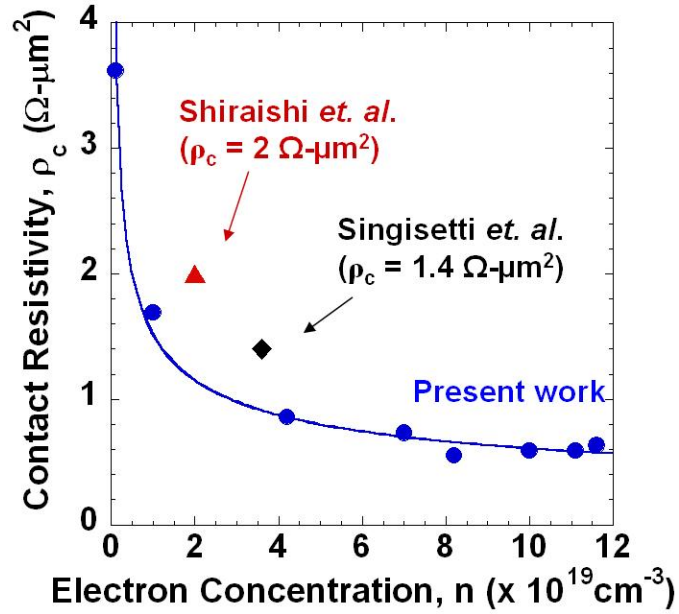


Figure 4.3: Variation of contact resistivity with electron concentration.

resistivity. The sheet resistivity determined from TLM measurements was $11 \Omega/sqr$, correlating closely to the sheet resistivity obtained with Hall measurements.

To find the Schottky barrier height for the metal semiconductor junction, metal contacts were formed to a very low doped ($4.5 \times 10^{16} \text{cm}^{-3}$) sample. The contacts were found to be ohmic, indicating very low or zero barrier height for the junction. These measurements support the fact that the Fermi level pins close to the conduction band for InAs.

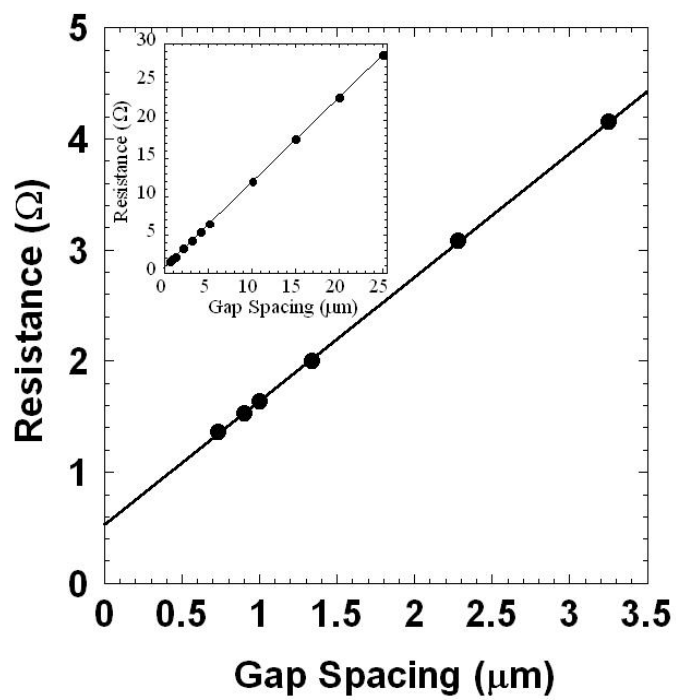


Figure 4.4: Measured TLM resistance as a function of pad spacing for the sample with $\rho_c = (0.6 \pm 0.4) \times 10^{-8} \Omega\text{-cm}^2$.

Chapter 5

p-InGaAs: Epitaxial Growth and Ohmic Contacts

In this chapter, the experimental details and results of p-type InGaAs doping calibrations are presented. The contact resistivities obtained for these degenerately doped epitaxial layers will also be discussed.

5.1 pInGaAs Doping Calibrations

Similar to n-type InGaAs, doping calibrations were done for p-type InGaAs by calibrating the dopant flux, arsenic flux and substrate temperature during growth.

5.1.1 Dopant flux calibrations

For a first set of samples, CBr_4 flux was varied during InGaAs growth keeping arsenic flux and substrate temperature constant. As shown in figure 5.1, the hole con-

centration increases initially with increase in CBr_4 flux (≤ 30 mTorr) but saturates at higher CBr_4 flux (≥ 30 mTorr). The saturation is because of autocompensation behavior of carbon. At higher carbon concentrations, the tendency to form di-carbon defects (split interstitial C-C pairs) increases [64]. These di-carbon defects act as deep donors compensating the active holes [65][66]. As shown in figure 5.1, the mobility continues to drop even as the hole concentration saturates at higher CBr_4 fluxes. We speculate that this drop in mobility could be due to scattering due the increased di-carbon defects sites.

5.1.2 Arsenic flux calibrations

For the arsenic flux calibration, the V/III ratio was varied from 8 to 60 (fig 5.2) on separate set of samples. For these calibrations, the CBr_4 flux and substrate temperature was kept constant at 60 mTorr and 460 °C, respectively. It was found that the hole concentration increases as the V/III ratio decreases. This is because the probability of carbon occupying a group V site increases on arsenic deficient surfaces [67]. V/III ratio below 8 resulted in rough films. As per our flux calibrations, V/III ratio of 8 corresponds to an arsenic flux of 1.5×10^{-6} Torr.

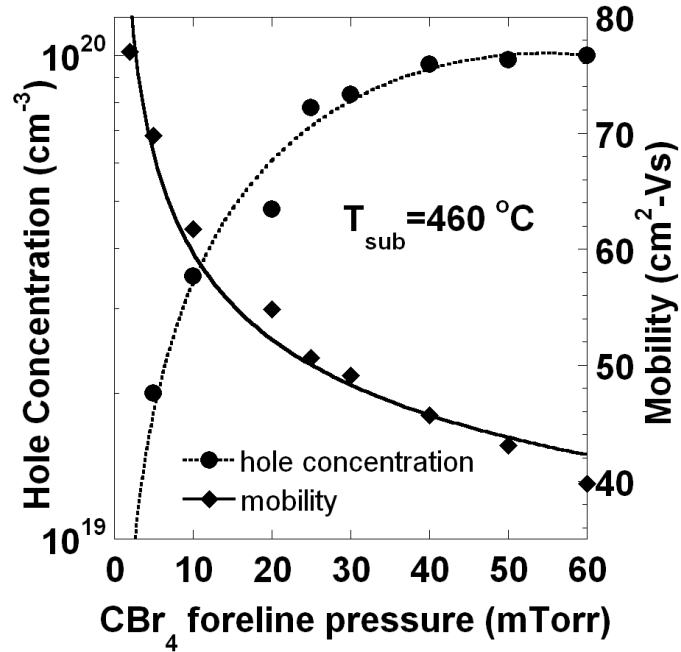


Figure 5.1: Variation of hole concentration and mobility with CBr₄ foreline pressure.

5.1.3 Substrate temperature calibrations

A third set of samples was grown by varying the substrate temperature (T_{sub}). Fig 5.3 shows the variation of hole concentration for samples grown at different substrate temperatures. As explained in references [68],[69], the tendency to form di-carbon defects decreases as the substrate temperature is reduced. However, the hole concentration was found to drop when the growth temperature was dropped below 325 °C. This drop could be because of insufficient decomposition of CBr₄ at low temperatures [70]. The effect of substrate temperature is again emphasized in fig 5.4 which

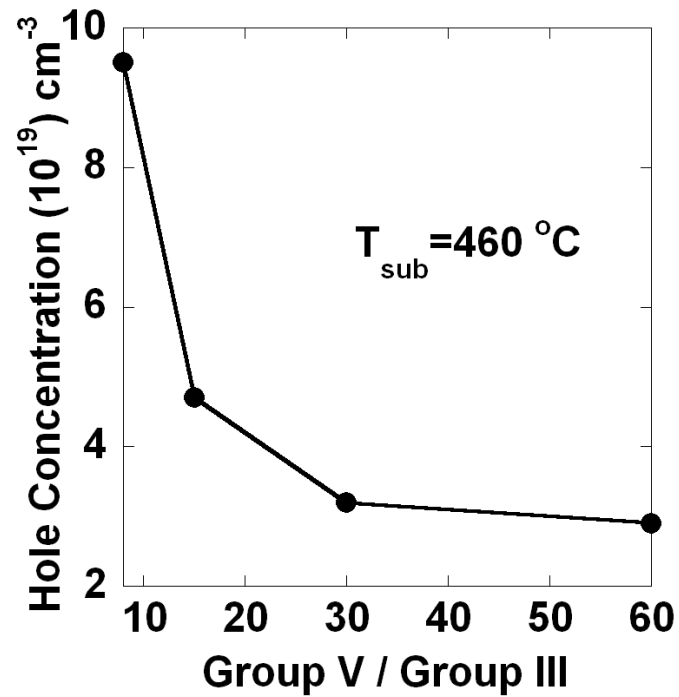


Figure 5.2: Variation of hole concentration with group V/group III ratio during growth.

compares the hole concentration for samples grown at 350 and 460 °C, with various CBr_4 fluxes.

The maximum hole concentration obtained after these calibrations was $2.2 \times 10^{20} \text{ cm}^{-3}$ at an As flux of 1×10^{-6} Torr and at a substrate temperature of 350 °C. This hole concentration is equivalent to the highest reported value [71].

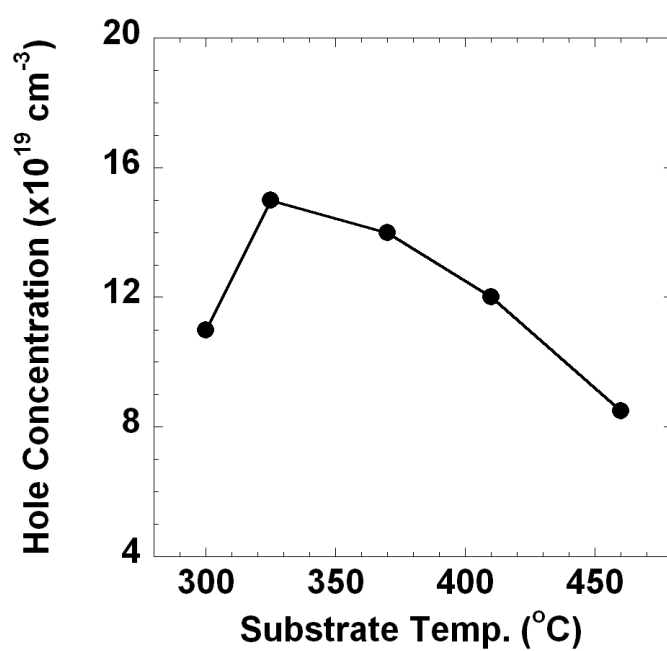


Figure 5.3: Variation of hole concentration with substrate temperature

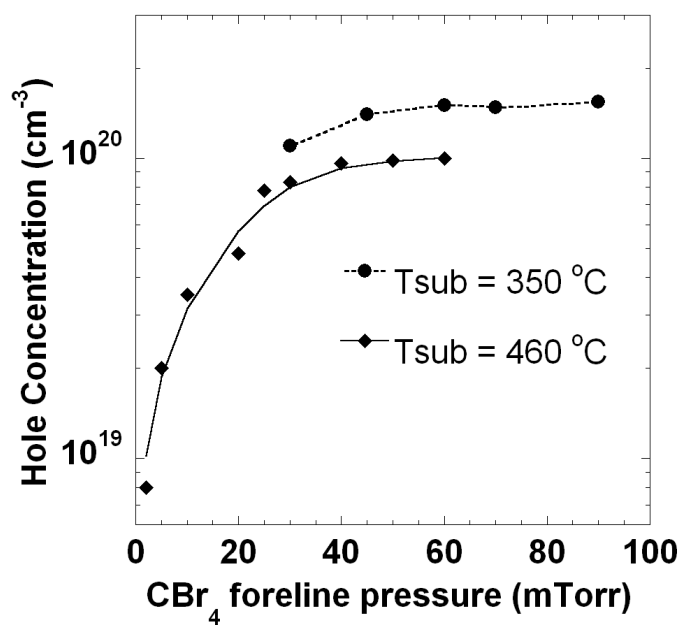


Figure 5.4: Dependence of hole concentration on substrate temperature

5.2 Ohmic Contacts

After the hole concentration was optimized, metal contacts were formed on p-type InGaAs epilayers. The contacts were formed by two techniques.

5.2.1 In-situ Contacts

In-situ contacts were formed to pInGaAs using the technique explained in section 3.2.1. We studied three different refractory metal contacts for pInGaAs: Mo, W and Ir. The work functions and melting points of these metals are listed in Table 5.1

Table 5.1: Refractory metal work functions and melting points

Metal	Work Function (eV)	Melting Point (°C)
W	4.5	3420
Mo	4.6	2620
Ir	5.7	2460

After the contact metal deposition, the samples were fabricated into TLM structures. The contact resistivities obtained for the three different metals are plotted with hole concentration in fig 5.5. It can be seen that all the three metals display ultra low contact resistivities at very high hole concentration. At a hole concentration of $2.2 \times 10^{20} \text{cm}^{-3}$ the contact resistivity obtained for Ir, W and Mo was $(0.6 \pm 0.5) \times 10^{-8} \Omega - \text{cm}^2$, $\rho_c = (1.2 \pm 0.7) \times 10^{-8} \Omega - \text{cm}^2$ and $\rho_c = (1.9 \pm 0.9) \times 10^{-8} \Omega - \text{cm}^2$, respectively. We suspect that these variations in contact resistivity for these metals could be due to

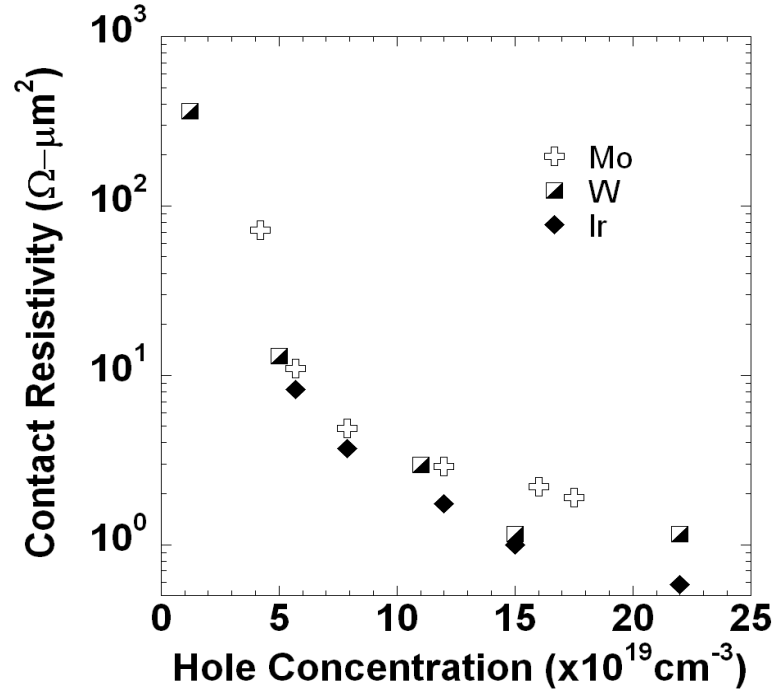


Figure 5.5: Variation of contact resistivity with hole concentration for in-situ W, Mo and Ir contacts.

difference in the Schottky barrier height. Nevertheless, these contact resistivities are the lowest reported to date for in-situ type contacts made to p-type InGaAs.

5.2.2 Ex-situ Contacts

For ex-situ contacts, as explained in section 3.2.2, the air exposed samples were oxidized with UV-ozone for 10 minutes and then treated with 10% HCl for 1 minute. After the UV-ozone and oxidal removal, the samples were then immediately loaded in an e-beam metal deposition chamber. 20 nm of W was deposited on the semiconduc-

tor surface at a growth rate of $0.5\text{\AA}/s$. The samples were then processed into TLM structures as explained in section 5.1. Figure 5.1 shows the variation of the contact resistivity obtained for ex-situ contacts. The lowest contact resistivity obtained was $(0.6 \pm 0.5) \times 10^{-8} \Omega - cm^2$ for a hole concentration of $1.6 \times 10^{20} cm^{-3}$. This contact resistivity is, again, the lowest reported to date for ex-situ type contacts made to p-type InGaAs.

Previously, NH_4OH treatment after UV-ozone treatment has shown to result in good ohmic contacts [37][36]. To compare the effectiveness of dil HCl with NH_4OH in cleaning the semiconductor surface, two samples were exposed to UV-ozone treatment 10 minute. One sample was treated with dil. HCl for 1 minute and the other sample was treated with NH_4OH . 20 nm of Mo was then deposited on both samples under similar conditions. The contact resistivity obtained for the sample treated with NH_4OH was found to be $(4 \pm 1.4) \times 10^{-8} \Omega - cm^2$ which was higher than the contact resistivity obtained for the sample treated with dil. HCl ($(2.2 \pm 1.0) \times 10^{-8} \Omega - cm^2$). This experiment proved the effectiveness of dil. HCl in removing the oxides and impurities from semiconductor surface.

Note: Quasi-insitu contacts were also studied for p-type InGaAs. As explained in 3.2.3, quasi-insitu contacts involve exposure of the semiconductor surface to atomic hydrogen. After exposure to atomic hydrogen, the hole concentration was found to decrease. This reduction in hole concentration can be explained by the passivation of

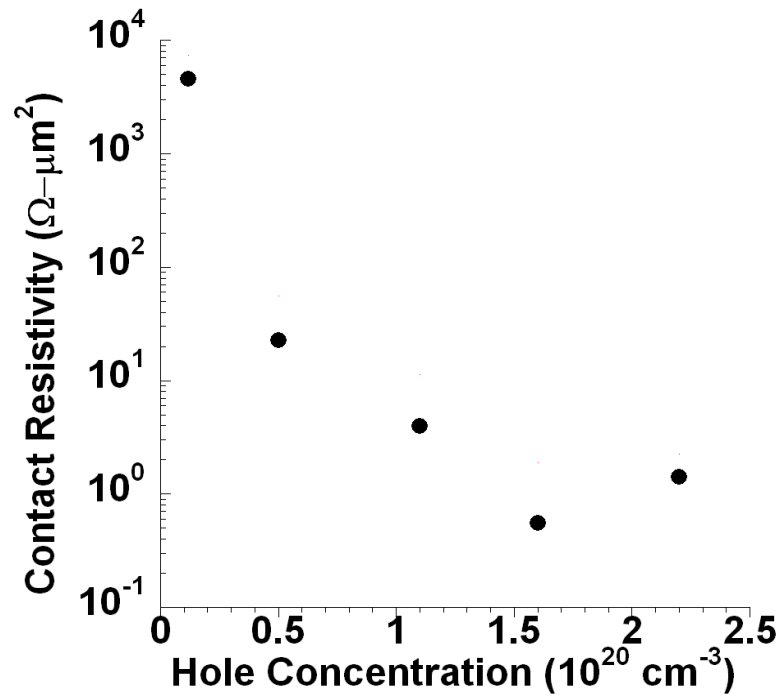


Figure 5.6: Variation of contact resistivity with hole concentration for ex-situ W contacts.

active carriers by atomic hydrogen. Atomic hydrogen attaches itself to C forming a $C_x\text{-H}$ complex ($x=\text{Ga,As}$) resulting in deactivation of the charge center [72][73]. Due to this deactivation of active carriers, surface cleaning using atomic hydrogen was not pursued.

5.3 Capacitance-Voltage Measurements

To ascertain the reasons for the difference in contact resistivities for the various refractory metals used for in-situ contacts, capacitance-voltage (C-V) measurements were done on Schottky contacts. For the fabrication of Schottky diodes, 2 μm thick Be doped InGaAs layer was grown on semi-insulating InP substrate. The hole concentration for these samples was $2 \times 10^{16} \text{cm}^{-3}$ as measured by Hall. Be was chosen as the dopant because it was easier to obtain hole concentration below $5 \times 10^{16} \text{cm}^{-3}$ controllably. CBr_4 flux was found to be unstable for obtaining such a low hole concentration.

Indium dots were put down at the corners of the sample to serve as the ohmic contact. Because of low doping ($2 \times 10^{16} \text{cm}^{-3}$) in the semiconductor, the surface depletion region was around 200 nm. It was important to diffuse the indium through the surface to make a contact with the conducting layer. This was achieved by annealing the samples at 250 °C for 30 minutes. Contact metal was then deposited on the samples so as to avoid exposure to the annealing conditions (as the Schottky barrier may change due to annealing). Before putting the metal contact, the semiconductor surface was oxidized with UV-ozone for 10 minutes and then treated with 10% HCl for 1 minute. The samples were then loaded immediately in a e-beam deposition chamber for contact metal (Ir or Mo or W) deposition. 20 nm of contact metal was deposited at a rate of 0.5 Å/s. The samples were then covered with a shadow mask with 150 μm wide

circular openings. Ti(20 nm)/Au(500 nm)/Ni(50 nm) dots were then deposited on the samples using electron beam evaporation. The samples were then dry etched using SF₆/Ar plasma which removes the contact metal (Ir or Mo or W) from the region in between the patterned dots.

C-V measurements were done on the fabricated samples using Agilent's 4284A C-V measurement system. The measurements were done at a frequency of 50 kHz with an AC modulation of 50 mV. Figure 5.7 shows the inverse of the square of the junction capacitance against the applied bias. The Schottky barrier height calculated from these plots were found to be equal for Ir and Mo (≈ 0.65 eV). Even though the barrier height for Ir and Mo are found to be about the same, the contact resistivity obtained for these contacts tend to differ (ρ_c for Ir = $(0.6 \pm 0.5) \times 10^{-8} \Omega - cm^2$; ρ_c for Mo = $(1.9 \pm 0.9) \times 10^{-8} \Omega - cm^2$). The Schottky barrier height for W was found to be ≈ 0.6 eV. Table 5.2 lists the contact resistivities and Schottky barrier obtained for the refractory contacts. Also, it should be noted that, although the contacts were fabricated on pieces taken from the same sample, difference in hole concentration can be observed from the $1/C^2$ -V plot shown in figure 5.7. The hole concentrations calculated from the slope of the plot were $1.2 \times 10^{16} cm^{-3}$, $1.6 \times 10^{16} cm^{-3}$ and $2.4 \times 10^{16} cm^{-3}$ for Ir, W and Mo Schottky contacts, respectively.

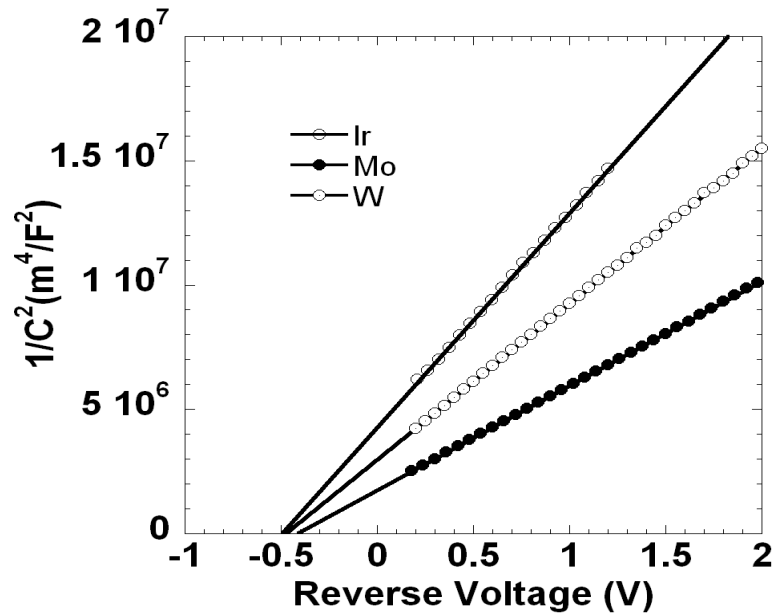


Figure 5.7: Reverse-bias $1/C^2$ versus voltage measured at room temperature for the Schottky diodes fabricated with W, Mo and Ir.

Table 5.2: Refractory metal contact resistivity and Schottky barrier height

Metal	ρ_c ($\Omega\text{-cm}^2$)	Schottky Barrier Height (eV)
W	1.2 ± 0.7	0.6
Mo	1.9 ± 0.9	0.65
Ir	0.6 ± 0.5	0.65

Chapter 6

Thermal Stability

During HBT fabrication flow, the device gets subjected to thermal cycles. In specific, the device needs to undergo annealing at 250 °C under N₂ atmosphere for 60 minutes for benzo cyclo butene (BCB) cure. For application in HBTs, the contacts studied here need to be stable at these annealing conditions. ρ_c data was compared for these contacts before and after annealing.

Table 6.1 compares the ρ_c obtained for nInGaAs, pInGaAs and nInAs samples, before and after annealing. A slight drop in ρ_c for nInGaAs contacts can be observed

Semiconductor	Contact Metal	$\rho_c(\Omega - \mu m^2)$ As Prepared	$\rho_c(\Omega - \mu m^2)$ Annealed
nInAs	Mo	1.5 ± 1.0	1.5 ± 1.0
nInGaAs	Mo	1.5 ± 1.0	1.5 ± 1.0
pInGaAs	Mo	1.5 ± 1.0	1.5 ± 1.0
pInGaAs	Mo	1.5 ± 1.0	1.5 ± 1.0
pInGaAs	Mo	1.5 ± 1.0	1.5 ± 1.0

Table 6.1: Resistivity comparison of various contacts before and after annealing

after annealing. Whereas, pInGaAs contacts show a rise in ρ_c on annealing. ρ_c for nInAs also showed slight increase after annealing.

To investigate the reason for these minor changes in contact resistivity, SIMS and TEM studies were done. The cross section of the samples was analyzed using TEM using a 200 kV FEI T20/EDX microscope. TEM sample preparation was performed using a focused ion beam (FIB) system. The analysis was done on a sample with W as the contact metal. For this sample, ρ_c was found to increase from x to y. Figure 6.1 compares the TEM micrographs of the unannealed and annealed sample. It can be seen that, on annealing, the W-InGaAs interface remains uniform and abrupt and indicates minimal intermixing of the metal semiconductor layers. However, intermixing between Ti and Au can be observed.

Energy-dispersive X-ray spectroscopy (EDS) measurements were also done on the annealed sample using the lamella prepared for TEM. EDS was done on 300 kV FEI Titan microscope. Figure 6.2 shows the compositional line scan along the cross section of the sample obtained by EDS. The depth resolution was found to be somewhat poor which could be because the lamella prepared for this study was thicker than 100 nm. However, slight diffusion of Au into Ti can be observed.

Schottky barrier height measurements were also done on the unannealed and annealed samples, using the technique explained in section pInGaAs Schottky contacts).

However, no change in Schottky barrier height was observed after annealing the samples.

Based on these measurements, it is difficult to ascertain the exact cause of the change in contact resistivity. It is possible that there might be minor interdiffusion of species across the interfaces which is difficult to detect with the characterization techniques used here.

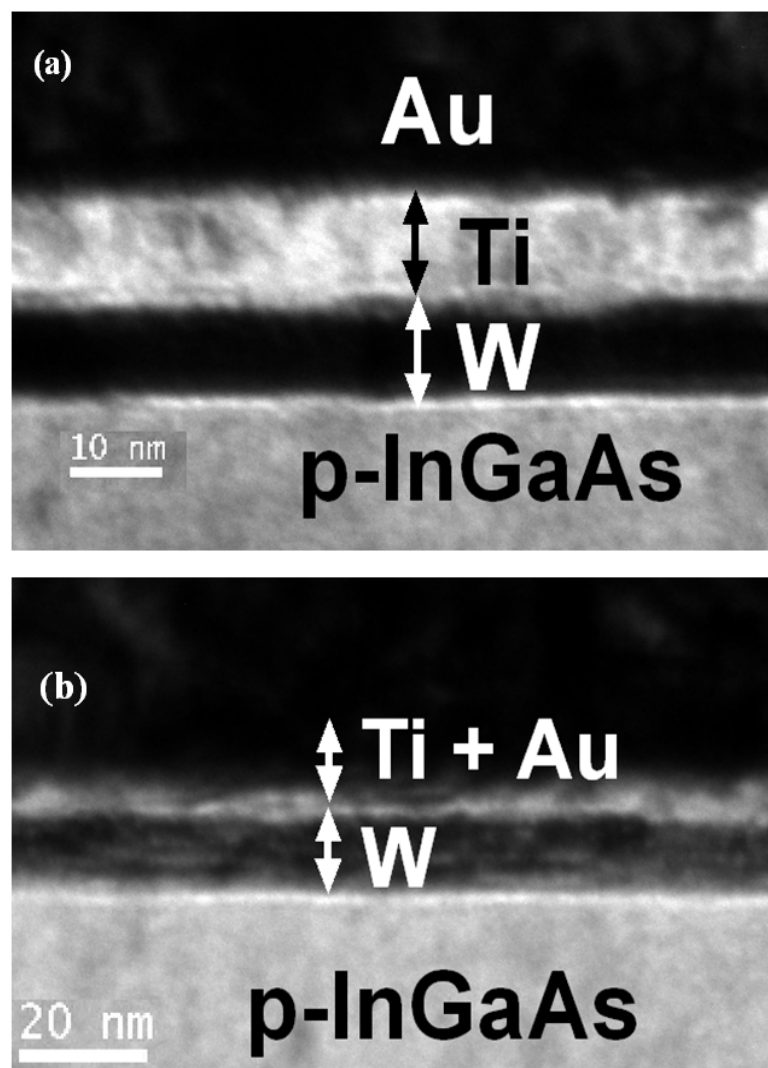


Figure 6.1: TEM images of W-pInGaAs samples before and after annealing. Intermixing between Ti and Au can be observed for annealed samples

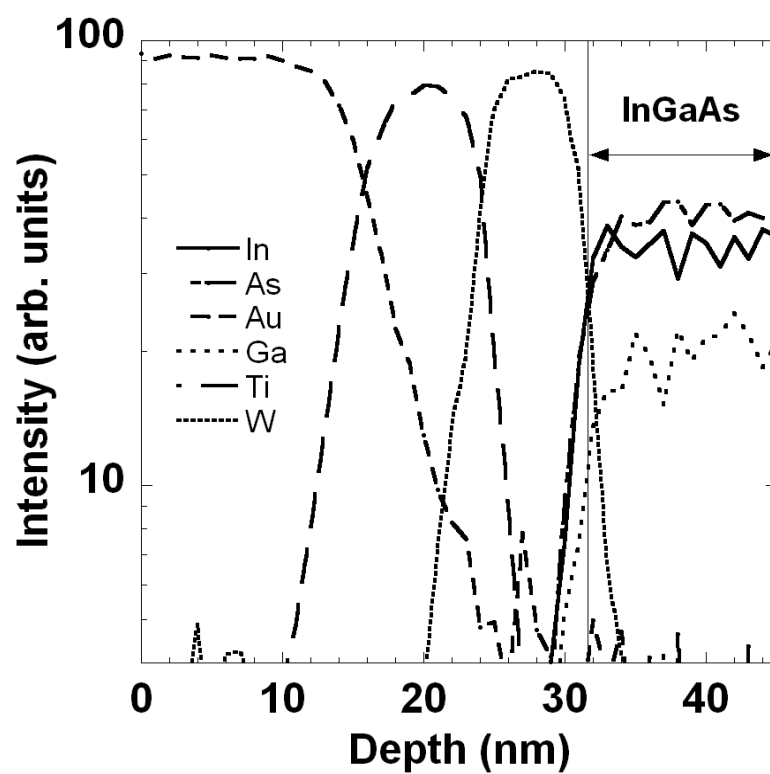


Figure 6.2: Compositional line scan along the cross section obtained by EDS

Chapter 7

Theoretical Analysis

In this chapter, we present theoretical calculations for the minimal possible contact resistivity for n-type and p-type semiconductors. We also, compare our experimental results with the calculations. The exact formula for the lowest contact resistance includes the non parabolic nature of the conduction-band and Fermi-Dirac statistics.

7.1 Current Density Derivation

The current density from semiconductor to metal is given by 7.1:

$$dJ_{sm} = \frac{2q}{(2\pi)^3} f(E, E_{fs})(1 - f(E, E_{fm}))v_{sz}T(k_s)dk_{sx}dk_{sy}dk_{sz} \quad (7.1)$$

where: v_{sz} = electron velocity in the semiconductor

$$f(E, E_{fs}) = \frac{1}{1 + \exp\left(\frac{E - E_{fs}}{kT}\right)}; \text{ semiconductor Fermi function}$$

$$f(E, E_{fm}) = \frac{1}{1 + \exp\left(\frac{E - E_{fm}}{kT}\right)}; \text{ metal Fermi function}$$

$$E_{fs} - E_{fm} = qV; V = \text{applied bias}$$

$$k_s^2 = k_{sx}^2 + k_{sy}^2 + k_{sz}^2$$

Similarly, the current density from metal to semiconductor is given by

$$dJ_{ms} = \frac{2q}{(2\pi)^3} f(E, E_{fm})(1 - f(E, E_{fs}))v_{mz}T(k_m)dk_{mx}dk_{my}dk_{mz} \quad (7.2)$$

where,

$$k_m^2 = k_{mx}^2 + k_{my}^2 + k_{mz}^2$$

assuming specular transmission at the interface

$$k_{mx} = k_{sx}; k_{my} = k_{sy} \quad (7.3)$$

For arbitrary energy band structures, it can be shown that (Appendix A):

$$v_{mz}dk_{mx}dk_{my}dk_{mz} = v_{sz}dk_{sx}dk_{sy}dk_{sz} \quad (7.4)$$

Also, $T(k_m) = T(k_s)$ [74]

Therefore, the net current density is given by:

$$dJ = dJ_{sm} - dJ_{ms} = \frac{2q}{(2\pi)^3} (f(E, E_{fs}) - f(E, E_{fm})) v_{sz} T(k_s) dk_{sx} dk_{sy} dk_{sz} \quad (7.5)$$

$$J = \int_{k_{sx}=-\infty}^{k_{sx}=\infty} \int_{k_{sy}=-\infty}^{k_{sy}=\infty} \int_{k_{sz}=0}^{k_{sz}=\infty} \frac{2q}{(2\pi)^3} [f(E, E_{fs}) - f(E, E_{fm})] v_{sz} T(k_s) dk_{sx} dk_{sy} dk_{sz} \quad (7.6)$$

Contact resistivity is defined as

$$\frac{1}{\rho_c} = \frac{dJ}{dV}_{@V=0} \quad (7.7)$$

$$\frac{1}{\rho_c} = \int_{k_{sx}=-\infty}^{k_{sx}=\infty} \int_{k_{sy}=-\infty}^{k_{sy}=\infty} \int_{k_{sz}=0}^{k_{sz}=\infty} \frac{2q^2}{(2\pi)^3 kT} \left[\frac{\exp\left(\frac{E-E_{fs}}{kT}\right)}{\left(1 + \exp\left(\frac{E-E_{fs}}{kT}\right)\right)^2} \right] v_{sz} T(k_s) dk_{sx} dk_{sy} dk_{sz} \quad (7.8)$$

Translating to polar coordinates

$$k_{st}^2 = k_{sx}^2 + k_{sy}^2 \quad (7.9)$$

$$dk_{sx} dk_{sy} = k_{st} dk_{st} d\theta \quad (7.10)$$

For a semiconductor with parabolic energy bands, the total electron energy in the semiconductor is given by:

$$E = q\phi_R + \frac{\hbar^2}{2m_s}(k_{st}^2 + k_{sz}^2) \quad (7.11)$$

and the electron group velocity is given by:

$$v_{sz} = \frac{1}{\hbar} \frac{\partial E}{\partial k_{sz}} = \frac{\hbar k_{sz}}{m_s} \quad (7.12)$$

Therefore,

$$\frac{1}{\rho_c} = \int_{k_{st}=-\infty}^{k_{st}=\infty} \int_{k_{sz}=0}^{k_{sz}=\infty} \int_{\theta=0}^{\theta=2\pi} \frac{2q^2}{(2\pi)^3 kT} \left[\frac{\exp\left(\frac{E-E_{fs}}{kT}\right)}{(1 + \exp\left(\frac{E-E_{fs}}{kT}\right))^2} \right] \frac{\hbar k_{sz}}{m_s} T(k_s) k_{st} dk_{st} d\theta dk_{sz} \quad (7.13)$$

$$\frac{1}{\rho_c} = \int_{k_{st}=-\infty}^{k_{st}=\infty} \int_{k_{sz}=0}^{k_{sz}=\infty} \frac{2q^2 \hbar}{(2\pi)^2 m_s kT} \left[\frac{\exp\left(\frac{E-E_{fs}}{kT}\right)}{(1 + \exp\left(\frac{E-E_{fs}}{kT}\right))^2} \right] T(k_s) k_{st} dk_{st} k_{sz} dk_{sz} \quad (7.14)$$

Let $E_{fs} = q\phi_{fs}$ and substituting

$$\frac{\hbar^2 k_{st}^2}{2m_s} = q\phi_{st} \quad (7.15)$$

$$\frac{\hbar^2}{m_s} k_{st} dk_{st} = q d\phi_{st} \quad (7.16)$$

$$k_{st} dk_{st} = \frac{qm_s}{\hbar^2} d\phi_{st} \quad (7.17)$$

Similarly,

$$\frac{\hbar^2 k_{sz}^2}{2m_s} = q\phi_{sz} \quad (7.18)$$

$$\frac{\hbar^2}{m_s} k_{sz} dk_{st} = q d\phi_{sz} \quad (7.19)$$

$$k_{st} dk_{sz} = \frac{qm_s}{\hbar^2} d\phi_{sz} \quad (7.20)$$

$$\frac{1}{\rho_c} = \int_{\phi_{st}=-\infty}^{\phi_{st}=\infty} \int_{\phi_{sz}=0}^{\phi_{sz}=\infty} \frac{2q^4 m_s}{(2\pi)^2 \hbar^3 kT} \left[\frac{\exp\left(\frac{q(\phi_R + V_{st} + \phi_{sz} - \phi_{fs})}{kT}\right)}{(1 + \exp\left(\frac{q(\phi_R + \phi_{st} + \phi_{sz} - \phi_{fs})}{kT}\right))^2} \right] T(k_s) d\phi_{st} d\phi_{sz} \quad (7.21)$$

For a case when $T(k_s) = 1$, substituting

$$p = \exp\left(\frac{q(\phi_R + \phi_{st} + \phi_{sz} - \phi_{fs})}{kT}\right) \quad (7.22)$$

$$\frac{dp}{p} = \frac{q}{kT} d\phi_{st} \quad (7.23)$$

Integration with respect to ϕ_{st} results in,

$$\frac{1}{\rho_c} = \int_{\phi_{sz}=0}^{\phi_{sz}=\infty} \frac{2q^3 m_s}{(2\pi)^2 \hbar^3} \left[\frac{1}{(1 + \exp(\frac{q(\phi_R + \phi_{sz} - \phi_{fs})}{kT}))} \right] d\phi_{sz} \quad (7.24)$$

When temperature, $T=0$ K,

$$\frac{1}{\rho_c} = \int_{\phi_{sz}=0}^{\phi_{sz}=(\phi_{fs}-\phi_R)} \frac{2q^3 m_s}{(2\pi)^2 \hbar^3} d\phi_{sz} \quad (7.25)$$

$$\frac{1}{\rho_c} = \frac{2q^3 m_s}{(2\pi)^2 \hbar^3} (\phi_{fs} - \phi_R) \quad (7.26)$$

$$\frac{1}{\rho_c} = \frac{4\pi q^3 m_s}{h^3} (\phi_{fs} - \phi_R) \quad (7.27)$$

When temperature, $T \neq 0K$,

$$\frac{1}{\rho_c} = \frac{2q^2 m_s}{(2\pi)^2 \hbar^3 kT} \log(1 + \exp(\frac{q}{kT}(\phi_R - \phi_{fs}))) \quad (7.28)$$

For a semiconductor with non-parabolic energy bands, the total electron energy in the semiconductor is given by:

$$(E - q\phi_R)(1 + \alpha(E - q\phi_R)) = \frac{\hbar^2}{2m_s}(k_{st}^2 + k_{sz}^2) \quad (7.29)$$

$$E = q\phi_R + \frac{1}{2\alpha} \left(\sqrt{1 + \frac{2\alpha\hbar^2(k_{st}^2 + k_{sz}^2)}{m_s}} - 1 \right) \quad (7.30)$$

and the electron group velocity is given by:

$$v_{sz} = \frac{1}{\hbar} \frac{\partial E}{\partial k_{sz}} = \frac{\hbar k_{sz}}{m_s \sqrt{1 + \frac{2\alpha\hbar^2(k_{st}^2 + k_{sz}^2)}{m_s}}} \quad (7.31)$$

Using these in 7.13, and using the substitutions from 7.15 and 7.18,

$$\frac{1}{\rho_c} = \int_{\phi_{st}=-\infty}^{\phi_{st}=\infty} \int_{\phi_{sz}=0}^{\phi_{sz}=\infty} \frac{2q^4 m_s}{(2\pi)^2 \hbar^3 kT} \frac{\exp(P)}{(1 + \exp(P))^2} \frac{T(k_s) d\phi_{st} d\phi_{sz}}{\sqrt{1 + 4\alpha q(\phi_{st} + \phi_{sz})}} \quad (7.32)$$

where,

$$P = \left(\frac{q\phi_R}{kT} + \frac{1}{2\alpha kT} (\sqrt{1 + 4\alpha q(\phi_{st} + \phi_{sz})} - 1) - \frac{q\phi_{fs}}{kT} \right) \quad (7.33)$$

For $T(k_s) = 1$

$$\frac{1}{\rho_c} = \int_{\phi_{sz}=0}^{\phi_{sz}=\infty} \frac{2q^3 m_s}{(2\pi)^2 \hbar^3} \frac{1}{1 + \exp(P)} d\phi_{sz} \quad (7.34)$$

Calculation of Fermi level position ($\phi_{fs} - \phi_R$)

The electron concentration is given by:

$$dn = 2f(E)N(E)dE \quad (7.35)$$

where, $N(E)$ is the 3D density of states

$$N(E) = \frac{\sqrt{2}}{\pi^2 \hbar^3} m_s^{3/2} \sqrt{E - E_c} \quad (7.36)$$

Therefore,

$$n = \frac{(2m_s)^{3/2}}{\pi^2 \hbar^3} \int_{E=0}^{E=\infty} \frac{\sqrt{E - E_c}}{1 + \exp\left(\frac{E - E_{fs}}{kT}\right)} dE \quad (7.37)$$

Here $E_c = q\phi_R$

7.1.1 Calculation of transmission coefficient, T: Parabolic case

In the past, WentzelKramersBrillouin (WKB) approximation has been used to calculate the transmission probability across a metal semiconductor interface [75]. However, there are certain limitations with this approximation. It breaks down at the regions close to the maximum of the potential barrier and it neglects quantum mechanical reflection at the interface. Here we present the derivation for the exact transmission coefficient, which includes quantum mechanical reflection and it is valid in all energy ranges. For calculating the transmission coefficient, the potential was approximated as shown in figure 7.1. This approximation is again illustrated in figure 7.2. In the region $d_1 < z < d_2$, inflection point ($z = i$) and the slope (m_i) at the inflection point was calculated for the theoretical potential barrier. A linear potential barrier was then assumed for this region ($d_1 < z < d_2$) with slope = m_i . The barrier approximation for region $0 < z < d_1$ is illustrated in figure 7.2. In this region, the barrier has a non-zero slope and the potentials at $z = 0$ and $z = d_1$ differ by a very small amount $d\phi_{Bn}$. This approximation was chosen as it facilitates the use of Airy functions as the solution of the Schrodinger equation in this region. The Airy function solutions are valid in all the energy ranges [76] i.e. $q\phi_R < E < \infty$ making the calculations less cumbersome. If a barrier with constant potential energy was chosen for this region ($0 < z < d_1$), it would require solutions of Schrodinger equations for $q\phi_R < E < q\phi_{Bn}$, $E = q\phi_{Bn}$ and $E > q\phi_{Bn}$ making the calculations tedious.

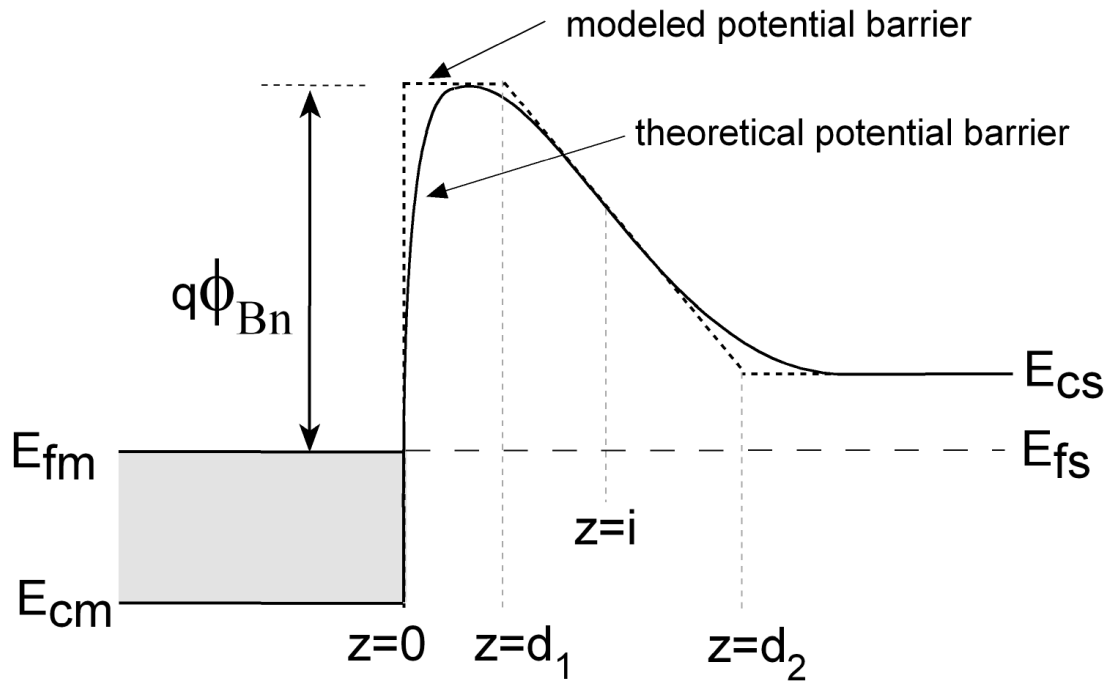


Figure 7.1: Schematic of the approximated potential barrier.

As shown in figure 7.2, the potential energy for various regions for the metal semiconductor junction is given by:

$$V_1(z) = 0, \quad z \leq 0 \quad (7.38)$$

$$V_2(z) = \phi_m - d\phi_{Bn} + s_1z, \quad 0 \leq z \leq d_1 \quad (7.39)$$

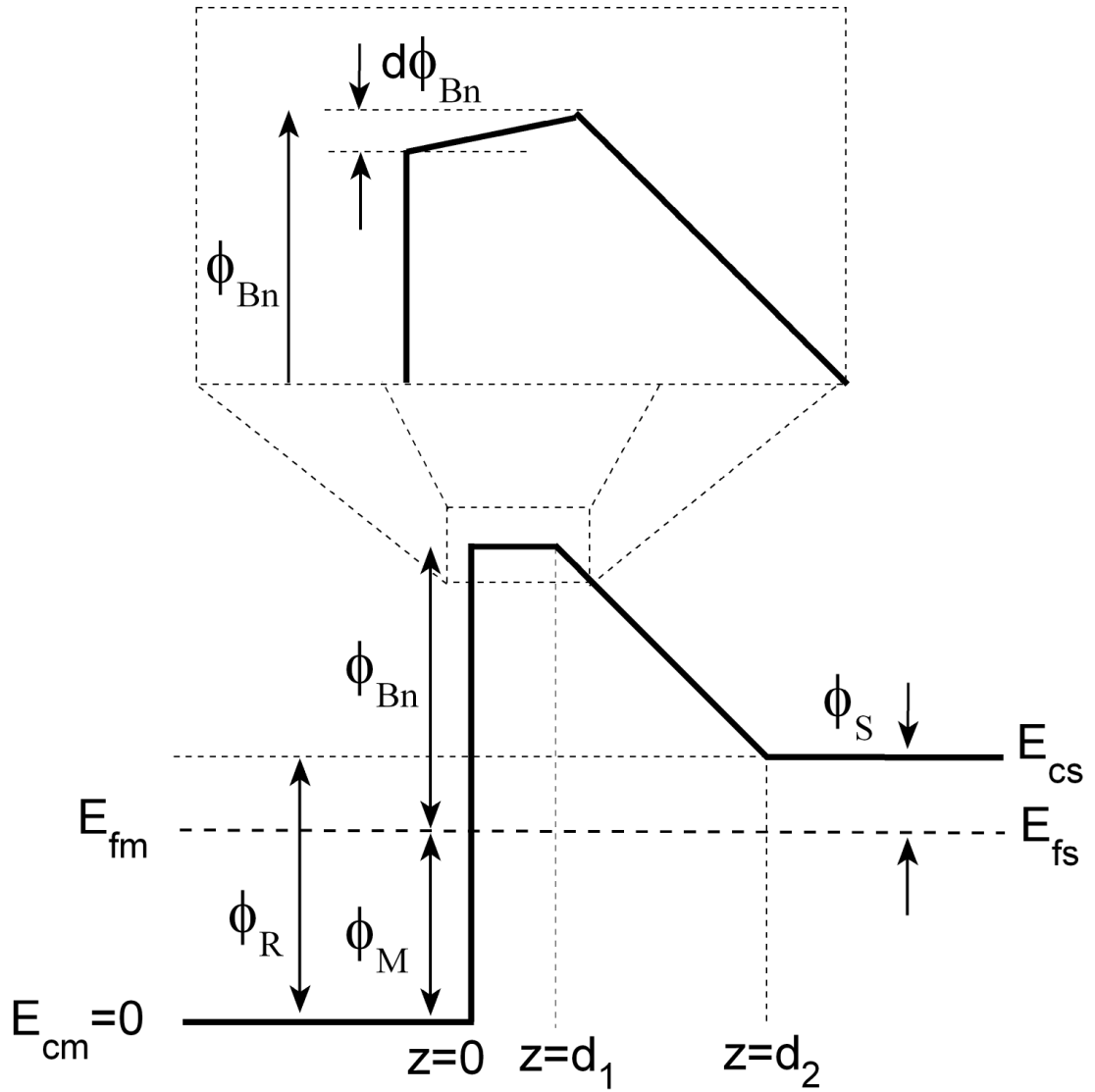


Figure 7.2: Schematic of the approximated potential barrier.

$$V_3(z) = \phi_m + \frac{\phi_m - \phi_R}{d_2 - d_1} d_1 - s_2 z, \quad d_1 \leq z \leq d_2 \quad (7.40)$$

$$V_4(z) = \phi_R, \quad z \geq d_2 \quad (7.41)$$

where: $\phi_m = \phi_M + \phi_{Bn} - \phi_S$

$$s_1 = d\phi_m/d_1$$

$$s_2 = \frac{\phi_m - \phi_R}{d_2 - d_1}$$

For the Schrödinger equation,

$$\frac{\hbar^2}{2m_s} \frac{d^2\psi}{dz^2} + [E_z - V(z)]\psi = 0 \quad (7.42)$$

the eigen function solutions in various regions are given by:

$$\psi_1(z) = \exp(ik_{mz}z) + R\exp(-ik_{mz}z), \quad z \leq 0 \quad (7.43)$$

$$\psi_2(z) = CAi[\rho_1(qV_1(z) - E_z)] + DBi[\rho_1(qV_1(z) - E_z)], \quad 0 \leq z \leq d_1 \quad (7.44)$$

$$\psi_3(z) = FAi[\rho_2(qV_2(z) - E_z)] + GBi[\rho_2(qV_2(z) - E_z)], \quad d_1 \leq z \leq d_2 \quad (7.45)$$

$$\psi_4(z) = texp(ik_{sz}z), \quad z \geq d_2 \quad (7.46)$$

where: $Ai(z)$ and $Bi(z)$ are the Airy functions[77], R, C, D, F, G and t are complex constants, and

$$\rho_1 = \left(\frac{2m_s}{\hbar^2 s_1^2}\right)^{1/3}, \rho_2 = \left(\frac{2m_s}{\hbar^2 s_2^2}\right)^{1/3}$$

From conservation of total energy (E) across the interface,

$$E = E_{mt} + E_{mz} = q\phi_R + E_{st} + E_{sz} \quad (7.47)$$

where:

$E_{mt} = q\phi_{mt}$ is the tranverse component of electron kinetic energy in metal

$E_{mz} = q\phi_{mz}$ is the component of electron kinetic energy perpendicular to the interface

$E_{st} = q\phi_{st}$ is the tranverse component of electron kinetic energy in semiconductor

$E_{sz} = q\phi_{sz}$ is the component of electron kinetic energy perpendicular to the interface

Also, from conservation of transverse momentum,

$$k_{mx} = k_{sx} \quad (7.48)$$

$$k_{my} = k_{sy} \quad (7.49)$$

Assuming parabolic energy bands for the metal and the semiconductor, the total energy is given by

$$E = q\phi_{mt} + \frac{\hbar^2 k_{mz}^2}{2m_m} = q\phi_R + q\phi_{st} + \frac{\hbar^2 k_{sz}^2}{2m_s} \quad (7.50)$$

$$k_{sz} = \left(\frac{2qm_s\phi_{sz}}{\hbar^2} \right)^{1/2} \quad (7.51)$$

$$k_{mz} = \left(\frac{2m_m(E - q(m_s/m_m)\phi_{st})}{\hbar^2} \right)^{1/2} \quad (7.52)$$

At $z = 0$,

$$\psi_1(0) = \psi_2(0) \quad (7.53)$$

$$\frac{1}{m_m} \frac{d\psi_1(0)}{dz} = \frac{1}{m_s} \frac{d\psi_2(0)}{dz} \quad (7.54)$$

At $z = d_1$,

$$\psi_2(d_1) = \psi_3(d_1) \quad (7.55)$$

$$\frac{d\psi_2(d_1)}{dz} = \frac{d\psi_3(d_1)}{dz} \quad (7.56)$$

At $z = d_2$,

$$\psi_3(d_2) = \psi_4(d_2) \quad (7.57)$$

$$\frac{d\psi_3(d_2)}{dz} = \frac{d\psi_4(d_2)}{dz} \quad (7.58)$$

Let,

$$A_{10} = Ai[\rho_1(\phi_m - d\phi_{Bn} - E_z)]; \frac{d}{dz} A_{10} = A_{10p}$$

$$B_{10} = Bi[\rho_1(\phi_m - d\phi_{Bn} - E_z)]; \frac{d}{dz} B_{10} = B_{10p}$$

$$A_{11} = Ai[\rho_1(\phi_m - E_z)]; \frac{d}{dz} A_{11} = A_{11p}$$

$$B_{11} = Bi[\rho_1(\phi_m - E_z)]; \frac{d}{dz} B_{11} = B_{11p}$$

$$A_{21} = Ai[\rho_2(\phi_m - E_z)]; \frac{d}{dz} A_{21} = A_{21p}$$

$$B_{21} = Bi[\rho_2(\phi_m - E_z)]; \frac{d}{dz} B_{21} = B_{21p}$$

$$A_{22} = Ai[\rho_2(\phi_R - E_z)]; \frac{d}{dz} A_{22} = A_{22p}$$

$$B_{22} = Bi[\rho_2(\phi_R - E_z)]; \frac{d}{dz} B_{22} = B_{22p}$$

Solving for t ,

$$t = \frac{2}{a_{10}(A_{10} + a_1 A_{10p}) + a_{11}(B_{10} + a_1 B_{10p})} \quad (7.59)$$

where,

$$a_{11} = (a_4 a_9 + a_5 a_8)$$

$$a_{10} = (a_6 a_9 + a_7 a_8)$$

$$a_9 = \exp(ik_{sz}d_2)(B_{22p} - a_3 B_{22})/W$$

$$a_8 = -\exp(ik_{sz}d_2)(A_{22p} - a_3 A_{22})/W$$

$$a_7 = (B_{21} B_{11p} - a_2 B_{21p} B_{11})/W$$

$$a_6 = (A_{21} B_{11p} - a_2 A_{21p} B_{11})/W$$

$$a_5 = (a_2 B_{21p} A_{11} - B_{21} A_{11p})/W$$

$$a_4 = (a_2 A_{21p} A_{11} - A_{21} A_{11p})/W$$

$$a_3 = -\frac{ik_{sz}}{\rho_2 s_2}$$

$$a_2 = -\frac{\rho_2 s_2}{\rho_1 s_1}$$

$$a_1 = -\frac{im_m \rho_1 s_1}{m_s k_{mz}}$$

$W = \text{Wronskian of Airy functions [77]} = (A_{ij}B_{ijp} - B_{ij}A_{ijp}) = 1/\pi; i, j = 1, 2$

The transmission probability is then given by [78]

$$T = \frac{k_{sz}}{m_s} \frac{m_m}{k_{mz}} |t|^2 \quad (7.60)$$

For a case where there is no depletion region in the semiconductor i.e. for a **step barrier** (as shown in fig 7.3), the solutions of the Schrodinger equation for the two regions are given by:

$$\psi_1(z) = \exp(ik_{mz}z) + A\exp(-ik_{mz}z), \quad z \leq 0 \quad (7.61)$$

$$\psi_2(z) = B\exp(ik_{sz}z), \quad z \geq d \quad (7.62)$$

At $z = 0$,

$$\psi_1(0) = \psi_2(0) \quad (7.63)$$

$$\frac{1}{m_m} \frac{d\psi_1(0)}{dz} = \frac{1}{m_s} \frac{d\psi_2(0)}{dz} \quad (7.64)$$

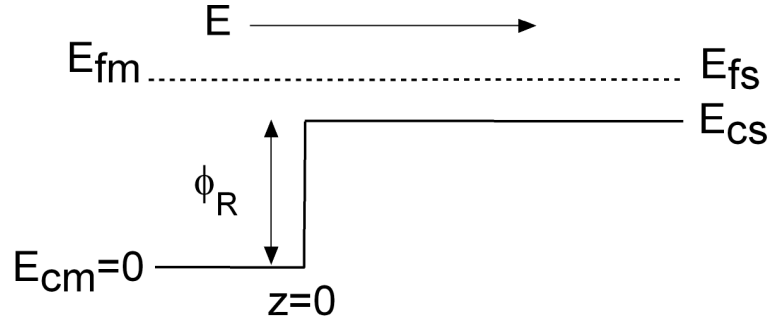


Figure 7.3: Schematic of a potential energy step

which yields,

$$B = \frac{2k_{mz}/m_m}{k_{mz}/m_m + k_{sz}/m_s} \quad (7.65)$$

where,

$$k_{sz} = \left(\frac{2qm_s\phi_{sz}}{\hbar^2} \right)^{1/2} \quad (7.66)$$

$$k_{mz} = \left(\frac{2m_m(E - q(m_s/m_m)\phi_{st})}{\hbar^2} \right)^{1/2} \quad (7.67)$$

The transmission probability is then given by [78]

$$T = \frac{k_{sz} m_m}{m_s k_{mz}} |B|^2 \quad (7.68)$$

7.1.2 Transmission probability: Non-parabolic case

As shown in equation 7.44, the component of energy in z-direction is required to calculate the transmission probability across a finite barrier. For a semiconductor with non-parabolic energy bands, the total energy is given by:

$$E = q\phi_R + \frac{1}{2\alpha} \left(\sqrt{1 + \frac{2\alpha\hbar^2(k_{st}^2 + k_{sz}^2)}{m_s}} - 1 \right) \quad (7.69)$$

For this case, it is not possible to separate out the components of energy in transverse and z-direction. Hence, for non-parabolic semiconductors, we will be calculating the minimum possible contact resistivity assuming a step barrier (i.e. no depletion region in the semiconductor). As explained in section (with step barrier), the eigenfunction solutions are given by,

$$\psi_m(z) = \exp(ik_{mz}z) + A\exp(-ik_{mz}z), \quad z \leq 0 \quad (7.70)$$

$$\psi_s(z) = B\exp(ik_{sz}z), \quad z \geq d \quad (7.71)$$

At $z=0$,

$$\psi_m(0) = \psi_s(0) \quad (7.72)$$

$$\frac{1}{m_m} \frac{d\psi_m(0)}{dz} = \frac{1}{m_s^*} \frac{d\psi_s(0)}{dz} \quad (7.73)$$

where m_s^* is the energy dependent conductivity mass in a non-parabolic semiconductor and is defined as [79]

$$m_s^* = m_s(1 + 2\alpha(E - q\phi_R)) \quad (7.74)$$

which yields,

$$B = \frac{2k_{mz}/m_m}{k_{mz}/m_m + k_{sz}/m_s^*} \quad (7.75)$$

Again, let

$$\frac{\hbar^2 k_{sz}^2}{2m_s} = q\phi_{sz} \quad (7.76)$$

$$\frac{\hbar^2 k_{st}^2}{2m_s} = q\phi_{st} \quad (7.77)$$

$$k_{sz} = \sqrt{2qm_s\phi_{sz}/\hbar^2} \quad (7.78)$$

$$k_{mz} = \sqrt{\frac{2m_m}{\hbar^2}\left(q\phi_R + \frac{C-1}{2\alpha} - q\frac{m_s}{m_m}\phi_{st}\right)} \quad (7.79)$$

where,

$$C = \sqrt{(1 + 4\alpha q(\phi_{st} + \phi_{sz}))}; \quad (7.80)$$

Therefore,

$$t = \frac{2k_{mz}/m_m}{k_{mz}/m_m + k_{sz}/m_s C} \quad (7.81)$$

Hence, the transmission probability is,

$$T = \frac{k_{sz}}{m_s} \frac{1}{(1 + 2\alpha(E - q\phi_R))} \frac{m_m}{k_{mz}} |t|^2 \quad (7.82)$$

7.2 Contact Resistivity Comparison

In this section, we present the calculated contact resistivities for n-type and p-type $\text{In}_{0.53}\text{Ga}_{0.47}\text{As}$, InAs , GaAs , InP , GaSb and InSb using the equations detailed in previous section and the parameters listed in Table 7.1 [79]. A comparison of the calculated and experimental contact resistivities for n- $\text{In}_{0.53}\text{Ga}_{0.47}\text{As}$, p- $\text{In}_{0.53}\text{Ga}_{0.47}\text{As}$ and n- InAs

Table 7.1: Compound semiconductor parameters

Parameter	InAs	In _{0.53} Ga _{0.47} As	GaAs	InP	GaSb	InSb
Band Gap Energy (eV)	0.354	0.74	1.424	1.344	0.726	0.17
Electron Effective Mass (m_s/m_o)	0.023	0.041	0.067	0.08	0.045	0.014
Light Hole Effective Mass (m_{lh}/m_o)	0.026	0.053	0.082	0.089	0.05	0.015
Heavy Hole Effective Mass (m_{hh}/m_o)	0.41	0.458	0.51	0.6	0.4	0.43
Split-off Hole Effective Mass (m_{sof}/m_o)	0.16	0.15	0.15	0.17	0.14	0.19
Split-off Band Energy (eV)	0.41	0.35	0.34	0.11	0.8	0.8
Non-parabolicity (eV^{-1})	2.73	1.12	0.64	0.67	1.36	5.72

is also presented.

7.2.1 nInAs Contact Resistivity

To calculate ρ_c , first the variation of the Fermi level $E_f - E_c$ or $\phi_{fs} - \phi_R$ with electron concentration was calculated using equation 7.37. Figure 7.4 shows the variation of electron concentration with Fermi level position, for parabolic and non-parabolic case.

The data computed from equation 7.37 was then used to calculate ρ_c . Figure 7.5 compares the calculated contact resistivities for the parabolic and non-parabolic case. It can be seen that the contact resistivities are equivalent for the two cases for most of the doping concentration range. This indicates that contact resistivity depends mainly on the total electron concentration. However, the contact resistivities show a slight deviation at electron concentrations $> 1 \times 10^{20} \text{ cm}^{-3}$.

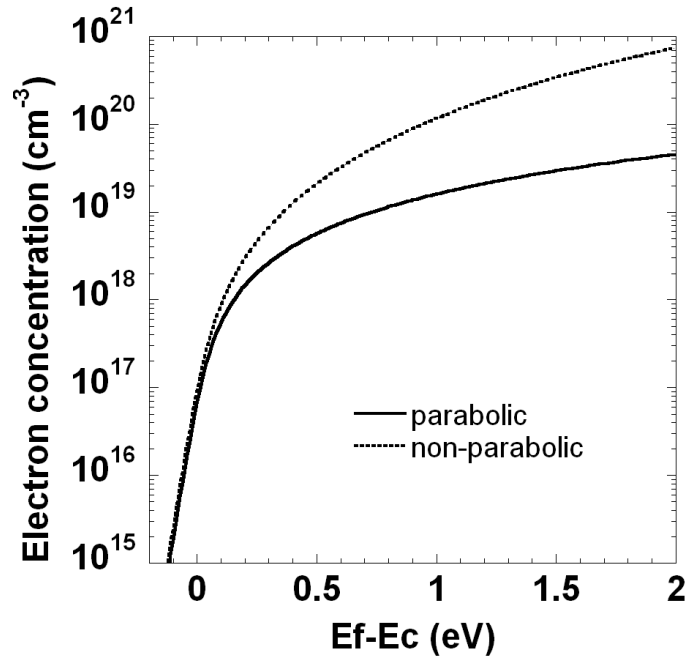


Figure 7.4: Variation of electron concentration with Fermi energy level for parabolic and non-parabolic case

Contact resistivity was also calculated assuming complete transmission, i.e. $T(E)=1$. Figure 7.6 compares the contact resistivity obtained for $T(E)=1$ with the contact resistivity for a step barrier for parabolic energy dispersion. Comparable contact resistivities were observed for the two cases, however, the contact resistivity tends to deviate at electron concentrations above $5 \times 10^{18} \text{ cm}^{-3}$. Figure 7.7 compares the contact resistivity obtained for $T(E)=1$ with the contact resistivity for a step barrier for non-parabolic energy dispersion. As seen in the figure, the contact resistivity for the step barrier is found to be somewhat higher than that for $T(E)=1$.

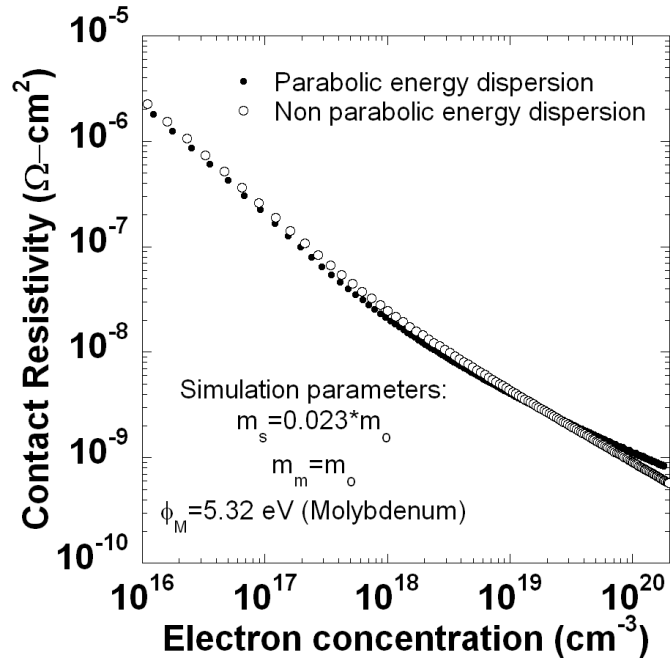


Figure 7.5: Variation of contact resistivity with electron concentration for parabolic and non-parabolic case.

Figure 7.8 compares the experimental contact resistivity (in-situ contacts) with the calculated minimum contact resistivity for non-parabolic case (it must be noted that non-parabolicity becomes dominant at high electron concentrations). For the calculations, the parameters used were:

$$m_s = 0.023m_o \quad (m_o = 9.1 \times 10^{-31})kg$$

$$m_m = m_o$$

$$\phi_M = 5.32eV \text{ (Molybdenum Fermi energy)}$$

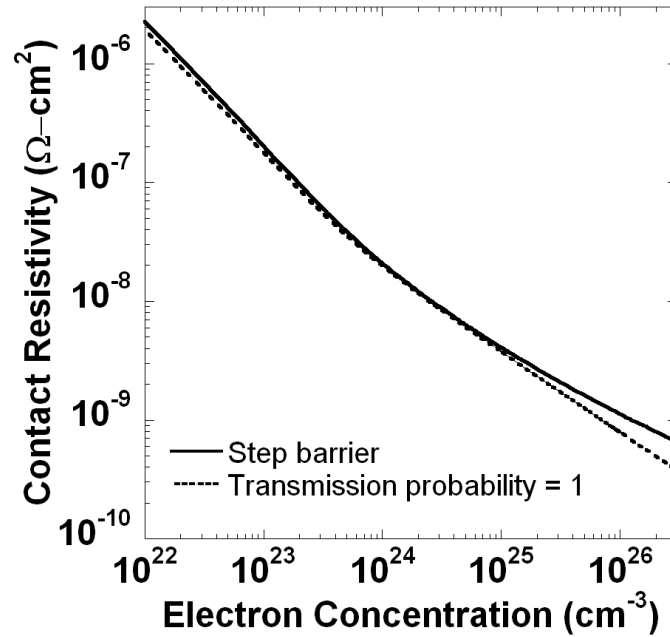


Figure 7.6: Comparison of contact resistivity obtained for a step barrier and for the case when $T(E)=1$ for parabolic energy dispersion.

It can be seen that the experimental values are higher than the calculated ones. This could be because, even though the in-situ contacts were fabricated in ultra high vacuum, there might still be a thin interfacial oxide layer between the metal and the semiconductor. In addition, the experimental contact resistivity follows a different slope as compared to the calculated contact resistivities. As shown in fig7.9, at high electron concentrations, L -valley may get populated. Due to the difference in effective electron mass between L -valley and Γ -valley, the transmission probability may be different for the electrons occupying the valleys. This filling of additional valley was neglected in present calculations and occupation only in Γ valley was assumed.

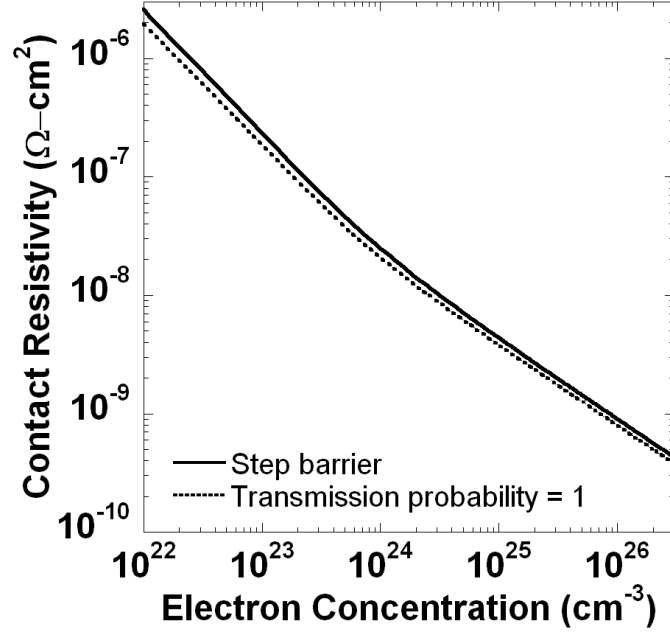


Figure 7.7: Comparison of contact resistivity obtained for a step barrier and for the case when $T(E)=1$ for non-parabolic energy dispersion.

Contact resistivities were also calculated for parabolic energy bands for various ϕ_B . The results are plotted in figure 7.10 along with the experimental data from present work for comparison. Figure also shows experimental data from literature, which includes contact resistivities obtained for as prepared and annealed contacts (add references).

To see the effect of $\phi_M = E_{fm} - E_{cm}$ on contact resistivity, calculations were done using three $\phi_M = 2, 5$ and 10 eV. The results are plotted in figure 7.11. As it can be seen in the figure, there is very minor dependence of contact resistivity on ϕ_M .

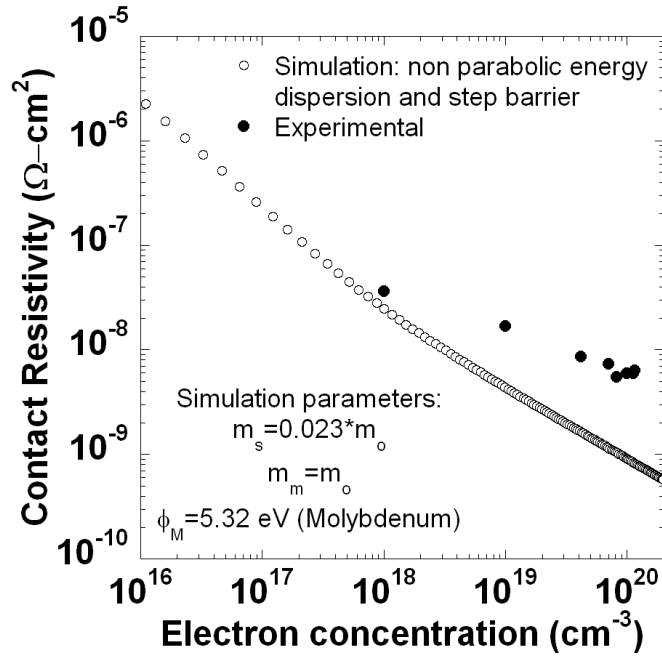


Figure 7.8: Comparison of experimental and calculated contact resistivity

Calculations were also done by varying the electron effective mass in metal. Fig7.12 shows the variation in contact resistivity with electron concentration for different metal electron mass. It can be seen that as the effective mass of electron in the metal increases the contact resistivity goes down. This could be because of the difference in the transmission probability for different electron effective mass. To verify this, we calculated the transmission probability across a step barrier for two different m_m . The results are plotted in fig 7.13. As seen in the figure, the transmission probability approaches unity at a lower energy (0.1 eV) for $m_m = m_o$, as compared to the case where $m_m = 0.023m_o$ [80].

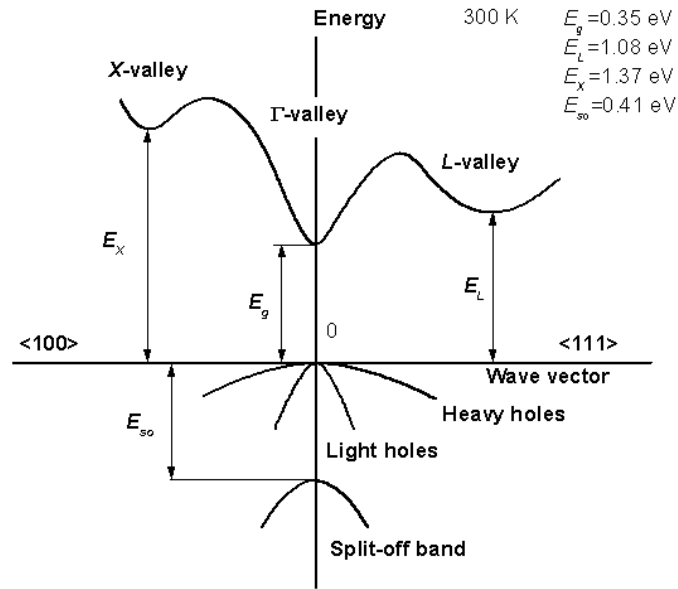


Figure 7.9: Energy band diagram for InAs [8].

7.2.2 n-In_{0.53}Ga_{0.47}As contact resistivity

Figure 7.14 shows the variation of electron concentration with Fermi level position, for parabolic and non-parabolic energy bands. Figure 7.15 shows the comparison of the contact resistivity for the parabolic and non-parabolic energy bands. A step potential barrier was assumed for these calculations. The parameters used for these calculations are also shown in the figure. As seen previously for n-InAs, the contact resistivity obtained for nInGaAs contacts for the two cases (parabolic and non-parabolic energy bands) are comparable.

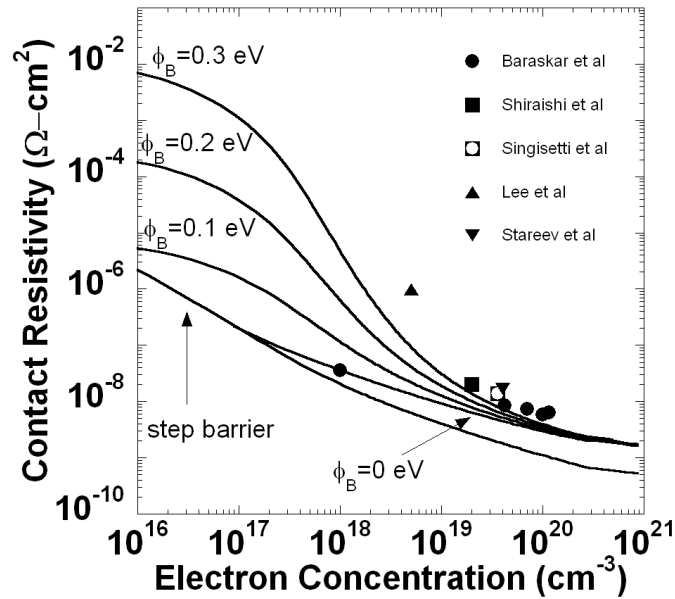


Figure 7.10: Variation of contact resistivity with electron concentration for parabolic case for various ϕ_B . Experimental data points are also plotted for comparison.

Figure 7.16 compares the the experimental contact resistivity data with the contact resistivity calculated for non-parabolic energy bands, assuming a step potential barrier. As mentioned previously, contact resistivity values for a finite tunneling barrier could not be calculated for the non-parabolic case. This is because to calculate the transmission coefficient it is required to know the component of energy perpendicular to the metal semiconductor interface. For non-parabolic energy dispersion it is not possible to separate out various components of energy without making approximations. However, contact resistivity for a finite tunnel barrier can be calculated for parabolic case. Figure 7.17 shows the contact resistivity calculated for parabolic case for different values of ϕ_B . Experimental data has also been shown on the plot for comparison (includes an-

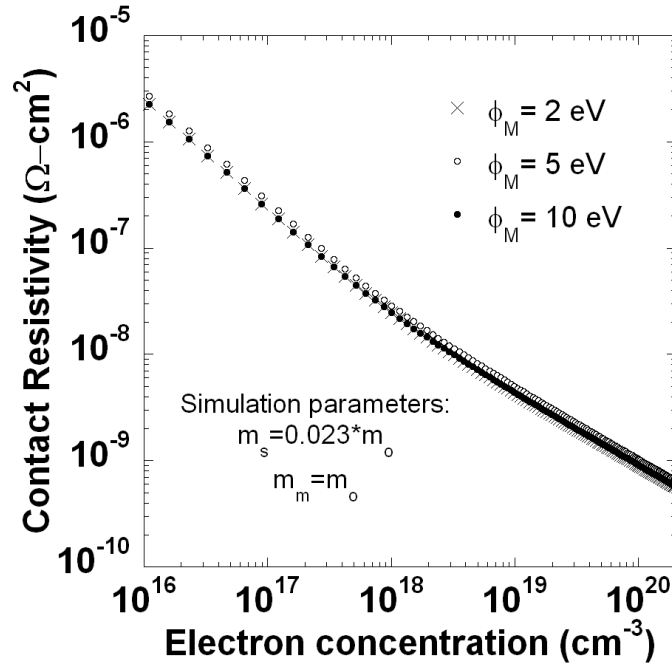


Figure 7.11: Variation of contact resistivity with electron concentration for various metal Fermi energies

nealed and un-annealed contacts). It must be noted that for these calculations, band gap narrowing due to heavy doping was neglected.

7.2.3 p-In_{0.53}Ga_{0.47}As contact resistivity

Contact resistivity was calculated for pInGaAs assuming parabolic energy dispersion in valence band. Figure 7.18 shows the variation of electron concentration with Fermi level position for parabolic energy bands. Figure 7.19 shows comparison of contact resistivity for various values of ϕ_B . As expected, ρ_c decreases as the value of

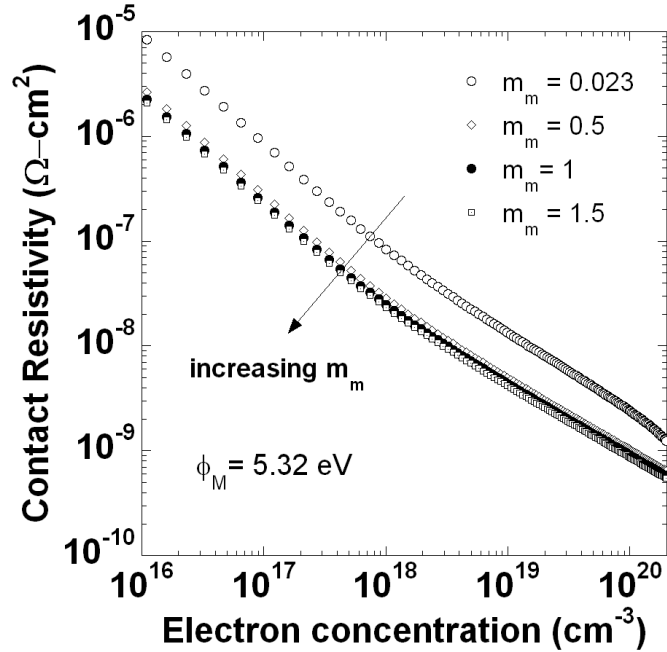


Figure 7.12: Variation of contact resistivity with electron concentration for various electron effective mass in metal

ϕ_B decreases. Experimental data is also plotted in figure 7.19 for comparison. As mentioned in section 5.3, the Schottky barrier height for p-InGaAs contacts was found to be 0.6 eV . As seen in the figure, majority of the experimental contact resistivity values lie close to the values calculated for $\phi_B = 0.6\text{-}0.8 \text{ eV}$.

7.2.4 Contact resistivities for GaAs, InP, GaSb and InSb

Calculations were also done to compute the minimum possible contact resistivity for n-type and p-type GaAs, InP, GaSb and InSb. For comparison, a step potential

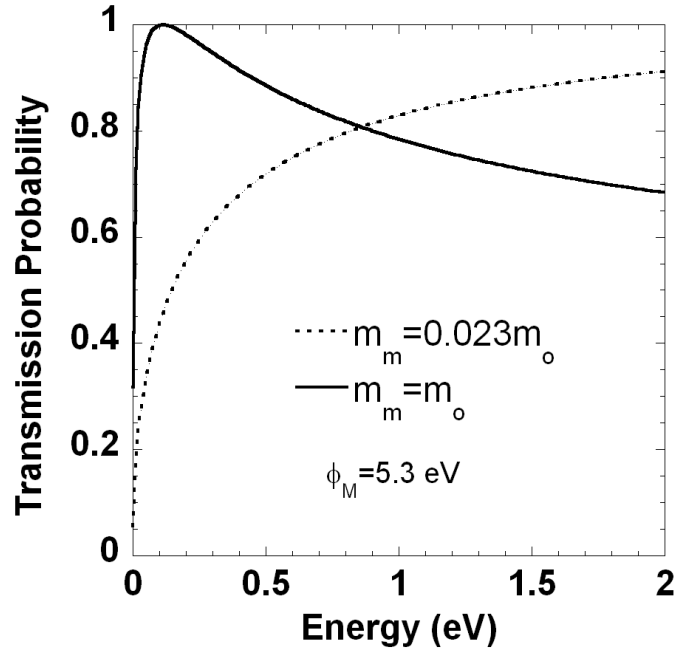


Figure 7.13: Dependence of electron transmission probability on effective mass

barrier and an un-pinned Fermi level in the semiconductor was assumed and contact resistivity was calculated by varying electron/hole concentrations. The parameters used for the calculations are listed in Table 7.1. Figure 7.20 shows the variation in contact resistivity with electron concentration for these semiconductors, including InAs and InGaAs. It can be observed that for lower electron concentrations, contact resistivity strongly depends on electron effective mass of the semiconductor. However, as the electron concentration increases, contact resistivity becomes comparable for these semiconductors. Figure 7.21 shows the variation of contact resistivity with hole concentration for these semiconductors. It can be observed that these semiconductors,

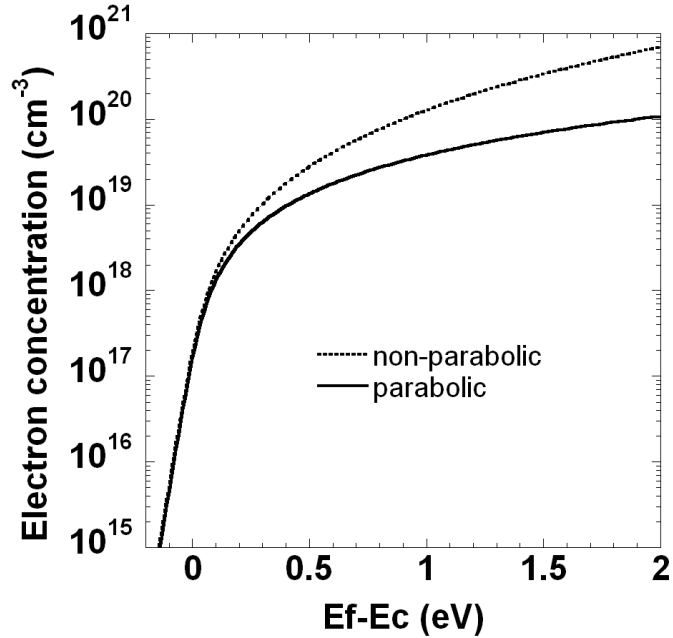


Figure 7.14: Variation of electron concentration with Fermi energy level for parabolic and non-parabolic energy bands for n-type $\text{In}_{0.53}\text{Ga}_{0.47}\text{As}$.

when doped p-type, exhibit comparable contact resistivity. However, slight dependence on the heavy hole mass m_{hh} was observed, as shown in figure 7.22.

Contact resistivities were also calculated for n-type and p-type InSb, GaSb, InP and GaAs for different Schottky barrier heights. The results are plotted in figures. Experimental contact resistivities obtained from various references are also indicated on the figures 7.23-7.34 (no experimental contact resistivity has been reported for contacts made to n-type and p-type InSb).

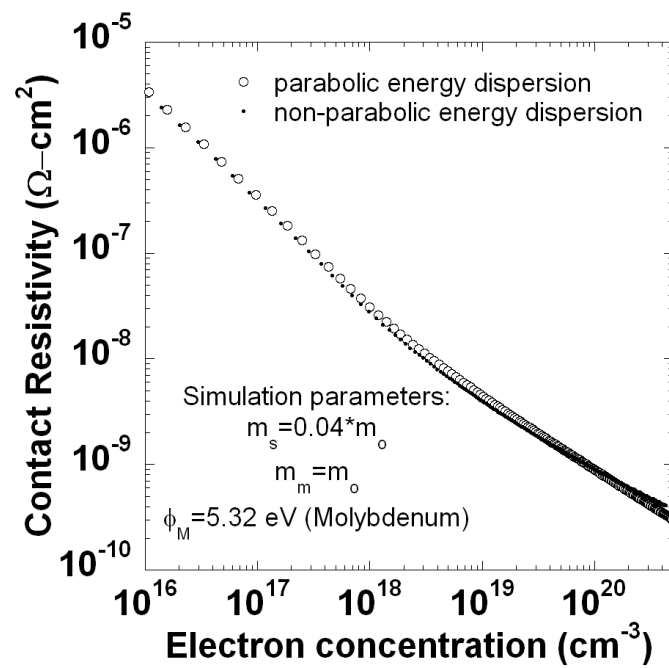


Figure 7.15: Variation of contact resistivity with electron concentration for parabolic and non-parabolic energy bands for n-type $\text{In}_{0.53}\text{Ga}_{0.47}\text{As}$.

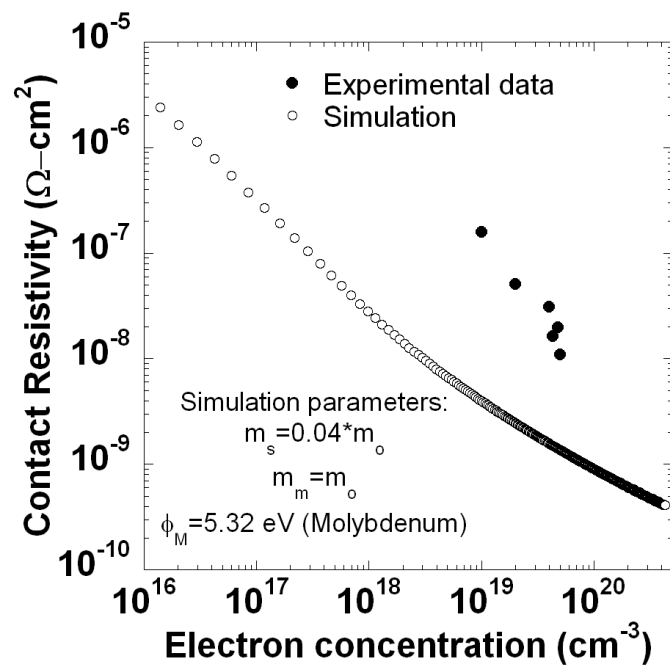


Figure 7.16: Comparison of experimental and calculated contact resistivity for n-type $\text{In}_{0.53}\text{Ga}_{0.47}\text{As}$. Calculations were done assuming non-parabolic energy bands.

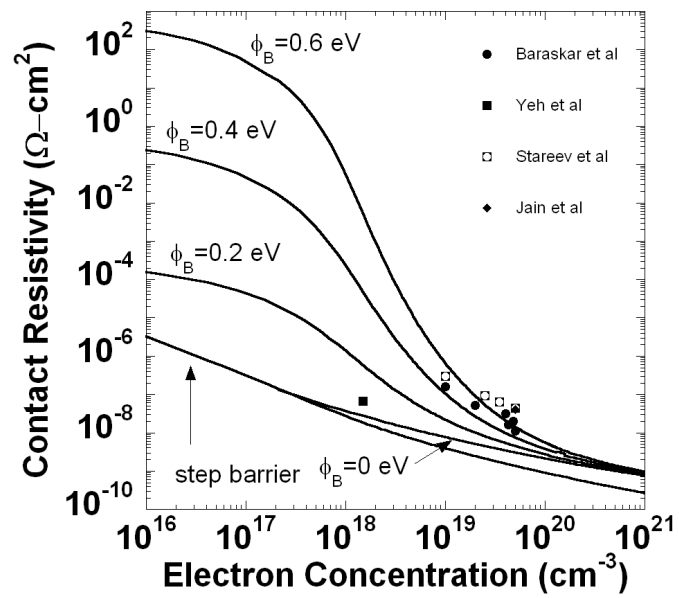


Figure 7.17: Comparison of experimental and calculated contact resistivities at various ϕ_B . Calculations were done assuming parabolic energy bands.

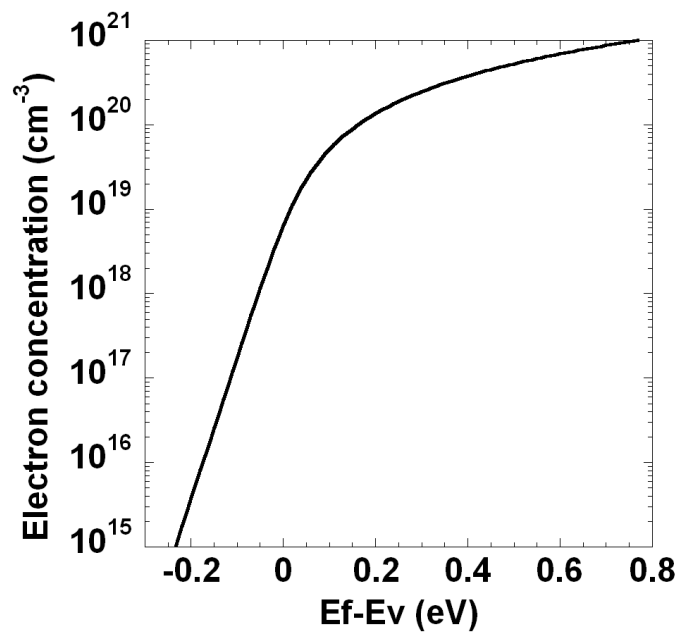


Figure 7.18: Variation of electron concentration with Fermi energy level for parabolic case.

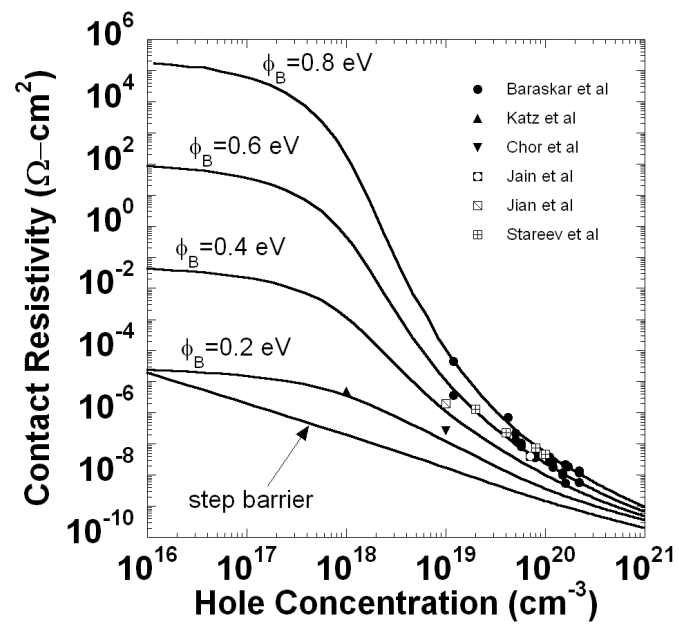


Figure 7.19: Comparison of calculated and experimental contact resistivities at various ϕ_B .

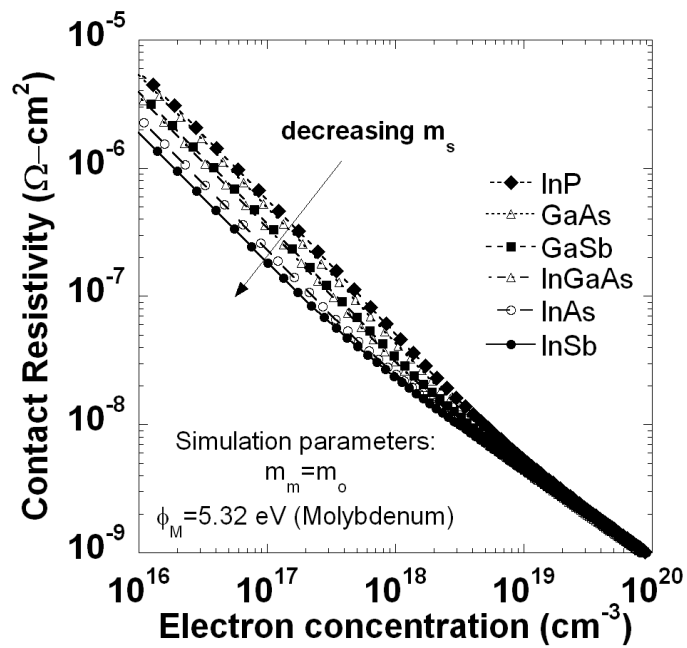


Figure 7.20: Comparison of contact resistivities of various semiconductors indicating the dependence on effective electron mass.

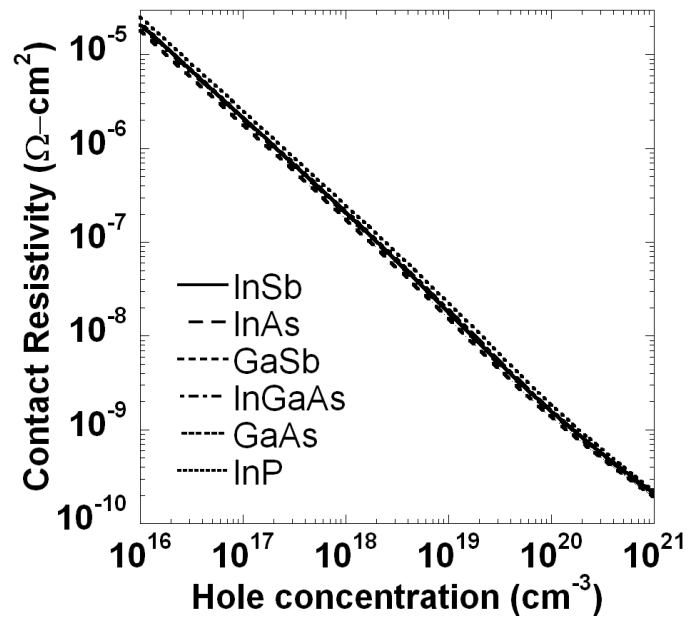


Figure 7.21: Comparison of contact resistivities of various p-type semiconductors.

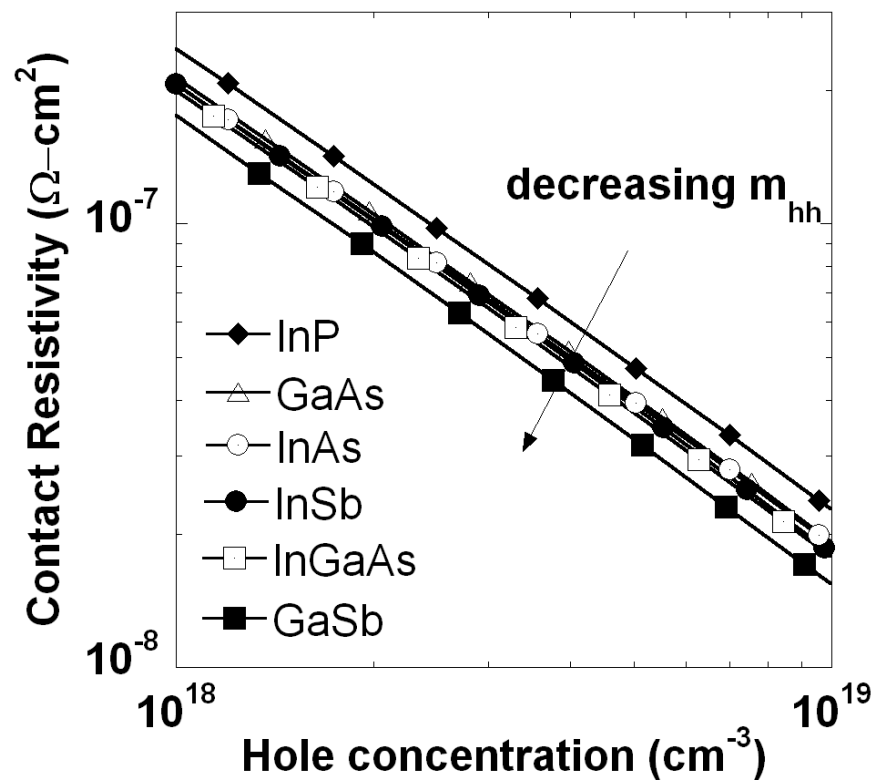


Figure 7.22: Comparison of contact resistivities of various semiconductors indicating the effect of effective hole mass.

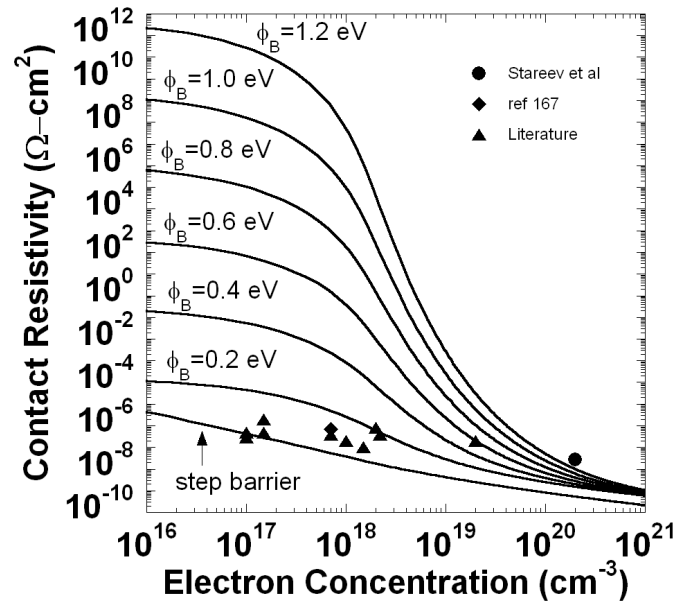


Figure 7.23: Comparison of calculated and experimental contact resistivities at various ϕ_B for n-type GaAs

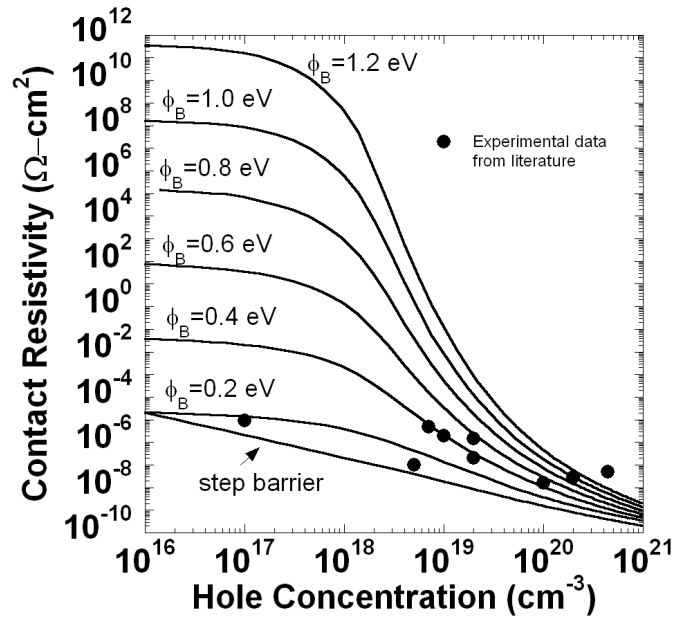


Figure 7.24: Comparison of calculated and experimental contact resistivities at various ϕ_B for p-type GaAs

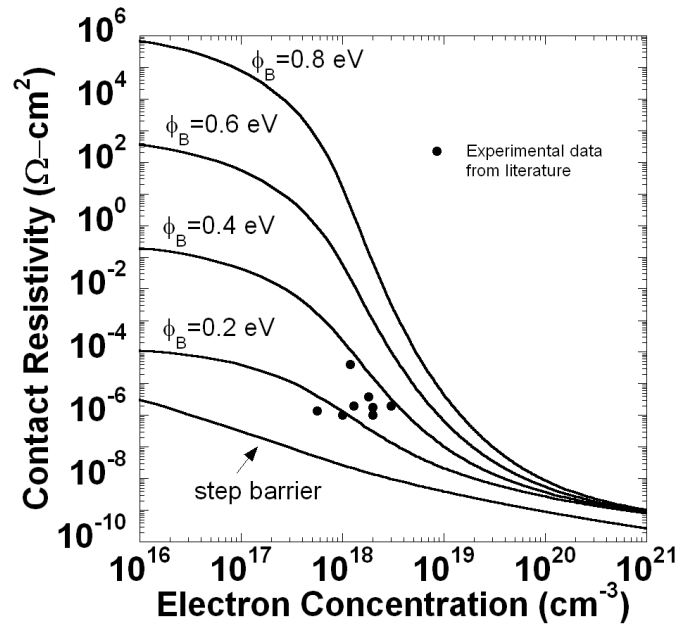


Figure 7.25: Comparison of calculated and experimental contact resistivities at various ϕ_B for n-type GaSb

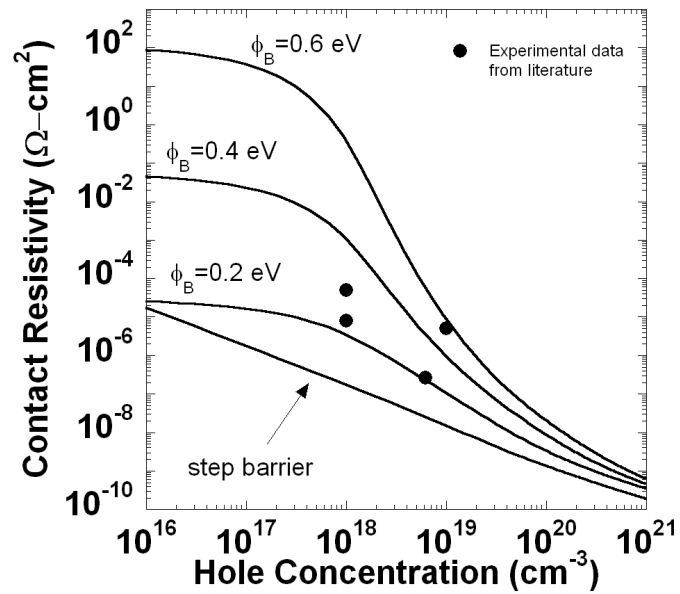


Figure 7.26: Comparison of calculated and experimental contact resistivities at various ϕ_B for p-type GaSb

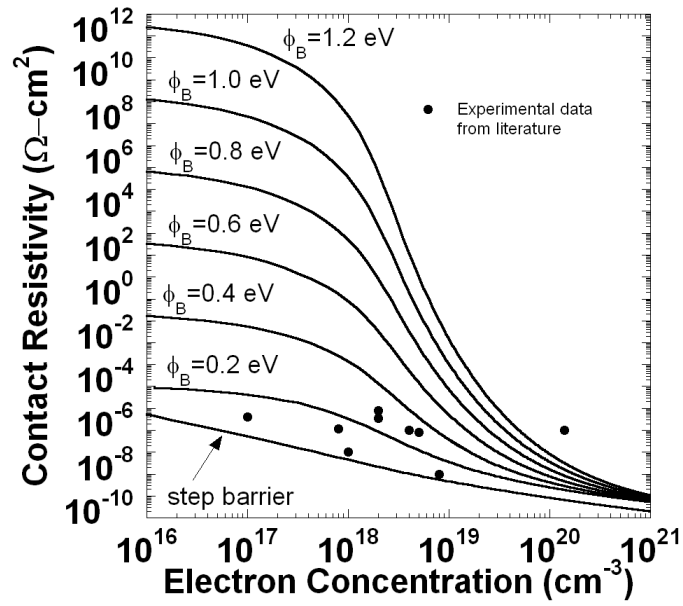


Figure 7.27: Comparison of calculated and experimental contact resistivities at various ϕ_B for n-type InP

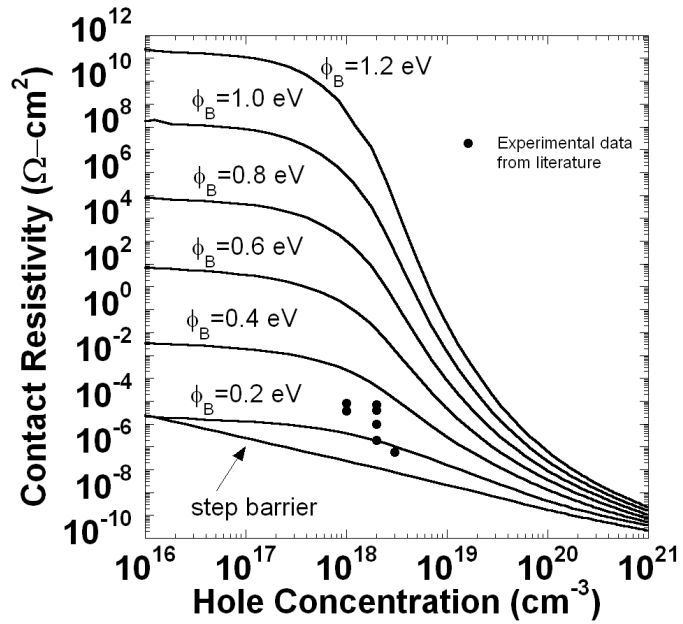


Figure 7.28: Comparison of calculated and experimental contact resistivities at various ϕ_B for p-type InP

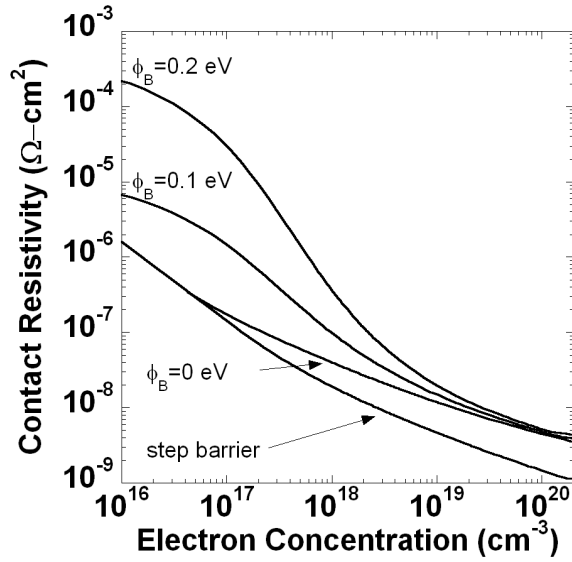


Figure 7.29: Comparison of calculated and experimental contact resistivities at various ϕ_B for n-type InSb

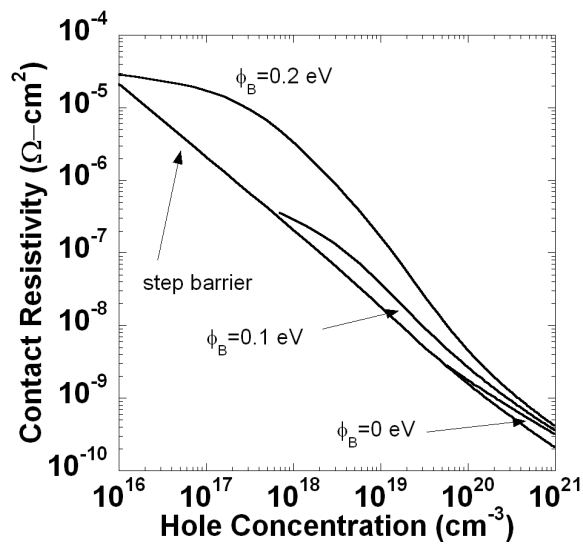


Figure 7.30: Comparison of calculated and experimental contact resistivities at various ϕ_B for p-type InSb

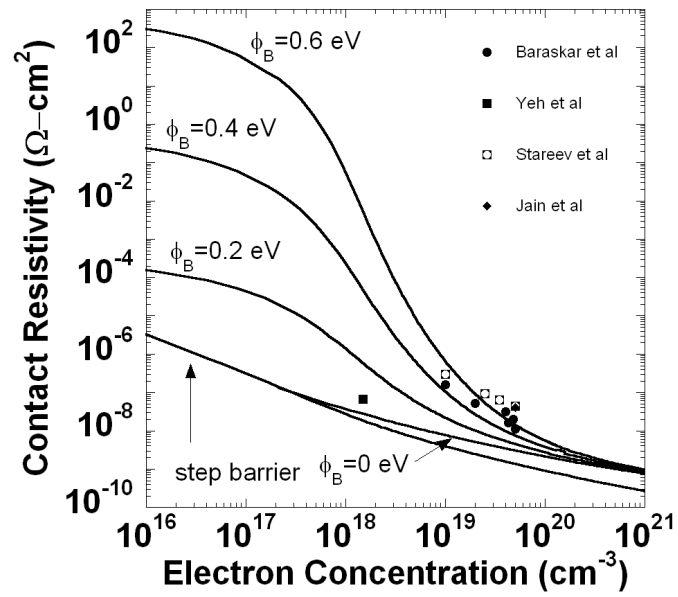


Figure 7.31: Comparison of calculated and experimental contact resistivities at various ϕ_B for n-type InGaAs

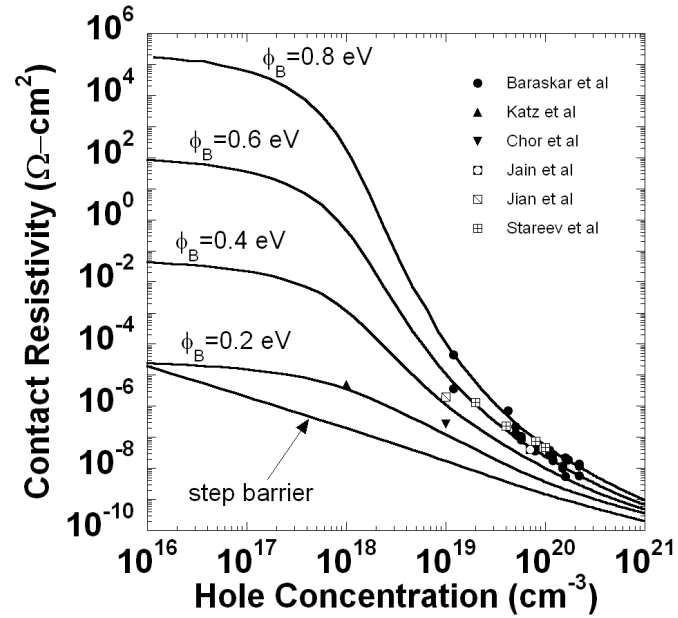


Figure 7.32: Comparison of calculated and experimental contact resistivities at various ϕ_B for p-type InGaAs

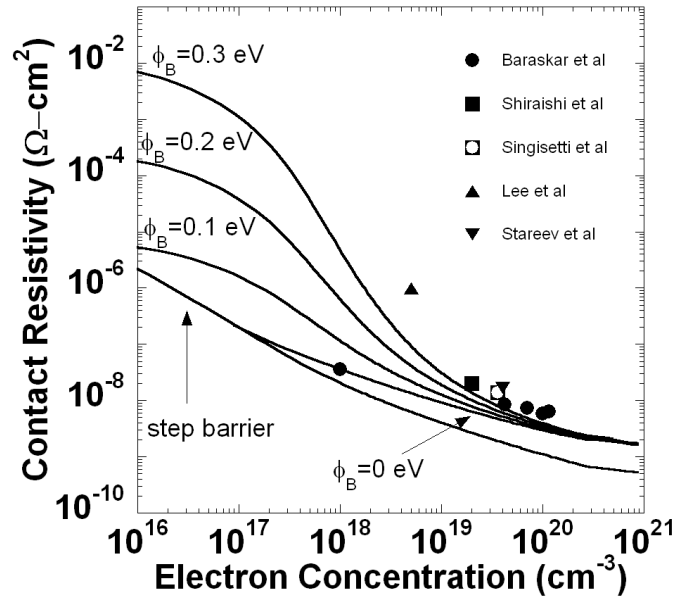


Figure 7.33: Comparison of calculated and experimental contact resistivities at various ϕ_B for n-type InAs

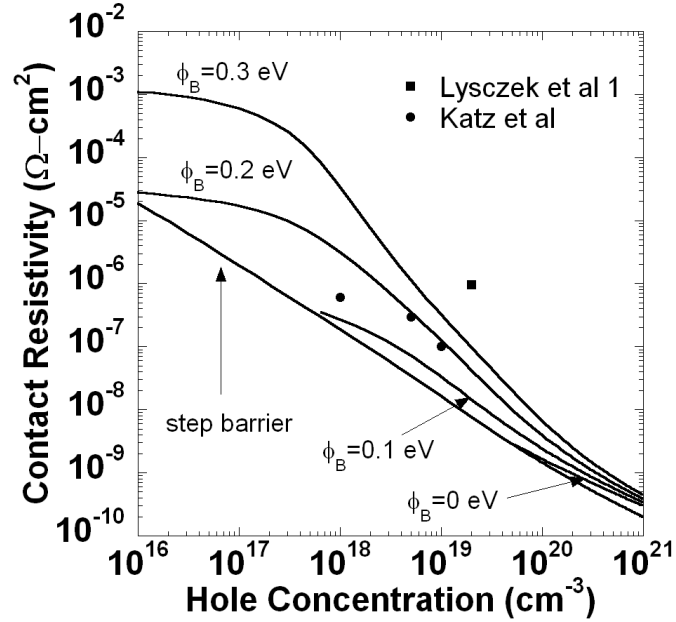


Figure 7.34: Comparison of calculated and experimental contact resistivities at various ϕ_B for p-type InAs

Chapter 8

Conclusions and Future Work

8.1 High doping

We have obtained high active carrier concentrations for n-type InAs, n-type $\text{In}_{0.53}\text{Ga}_{0.47}\text{As}$ and p-type $\text{In}_{0.53}\text{Ga}_{0.47}\text{As}$ through optimization of substrate temperature, arsenic flux and dopant flux during MBE growth. For n-type $\text{In}_{0.53}\text{Ga}_{0.47}\text{As}$, it was observed that heavy dopant concentration ($[\text{Si}] \approx 2 \times 10^{20} \text{ cm}^{-3}$), low substrate temperature (≈ 350 °C) and high arsenic overpressure (1.5×10^{-5} Torr) result in high electron concentrations. The low substrate temperature results in enhanced sticking coefficient of arsenic, thereby allowing Si to occupy only group III sites. Similarly, due to high arsenic overpressure, all group V sites are occupied by arsenic atoms reducing the probability of Si occupying group V site and hence results in reducing auto compensation of carriers. Through these calibrations, the highest electron concentration obtained was $6 \times 10^{19} \text{ cm}^{-3}$.

Similarly, for the growth of n-type InAs low growth temperature (≈ 350 °C) and heavy dopant concentration ($[\text{Si}] \approx 2 \times 10^{20} \text{ cm}^{-3}$) was found to result in high electron concentrations. However, the range of As flux was found to be narrow for the growth of good quality InAs films (5×10^{-7} Torr to 1.5×10^{-6} Torr). The highest active carrier concentrations obtained was $1 \times 10^{20} \text{ cm}^{-3}$, which is also the **highest reported to date** for Si doped InAs.

For the growth of heavily doped p-type $\text{In}_{0.53}\text{Ga}_{0.47}\text{As}$, a low arsenic overpressure of 1.5×10^{-6} Torr was required. This is because the tendency of carbon to occupy group V site increases at a low arsenic overpressure. A low substrate temperature (≈ 350 °C) was also required because the tendency to form di-carbon defects decreases at low substrate temperatures. Using these calibrations, the highest hole concentration obtained was $2.2 \times 10^{20} \text{ cm}^{-3}$.

8.2 Contact Resistivity

Refractory contacts were made on the heavily doped semiconductor epitaxial layers using in-situ and ex-situ techniques, which resulted in **record low** specific contact resistivities.

For n-type $\text{In}_{0.53}\text{Ga}_{0.47}\text{As}$, an ultra-low specific contact resistivity of $(0.98 \pm 0.34) \times 10^{-8} \Omega\text{-cm}^2$ was obtained through in-situ techniques using Mo as the contact metal.

It was also observed that the contact resistivity depends on total silicon concentration in $\text{In}_{0.53}\text{Ga}_{0.47}\text{As}$. Our results indicate that above a total silicon concentration of $\geq 2 \times 10^{20} \text{ cm}^{-3}$, the specific contact resistivity continues to decrease, even though the total electron concentration drops beyond this silicon concentration. We speculate that the silicon atoms introduce defect states in the band gap of $\text{In}_{0.53}\text{Ga}_{0.47}\text{As}$ providing additional paths for the electron to travel across the metal semiconductor interface. The contacts were found to remain stable on annealing.

For n-type InAs, the specific contact resistivity was found to vary with electron concentration, even though the Fermi level is believed to be pinned in the conduction band. For active carrier concentration below $8.2 \times 10^{19} \text{ cm}^{-3}$, contact resistivity decreases with increase in the active carrier concentration and saturates for an active carrier concentration greater than $8.2 \times 10^{19} \text{ cm}^{-3}$. This indicates that, although the Fermi level pins in the conduction band for InAs, an active carrier concentration greater than $4 \times 10^{19} \text{ cm}^{-3}$ is required to obtain contact resistivity less than $1 \times 10^{-8} \Omega\text{-cm}^2$. Metal contacts formed to a very low doped ($4.5 \times 10^{16} \text{ cm}^{-3}$) sample were found to be ohmic, indicating the absence of a Schottky barrier and supports the fact that the Fermi level pins close to the conduction band for InAs. The drop in contact resistivity with increase in electron concentration could be attributed to the increase in the number of conduction electrons at higher doping concentrations. The lowest contact resistivity extracted from the TLM

measurements was $(0.6 \pm 0.4) \times 10^{-8} \Omega\text{-cm}^2$ for in-situ Mo contacts for a sample with an active carrier concentration of $8.2 \times 10^{19} \text{cm}^{-3}$.

For p-type $\text{In}_{0.53}\text{Ga}_{0.47}\text{As}$, W, Mo and Ir refractory metals were used for making the contact. The lowest contact resistivity obtained was $(0.6 \pm 0.5) \times 10^{-8} \Omega\text{-cm}^2$ for Ir contacts made to p-type $\text{In}_{0.53}\text{Ga}_{0.47}\text{As}$ with a hole concentration of $2.2 \times 10^{20} \text{cm}^{-3}$. Contacts made using W and Mo as the contact metal demonstrated somewhat higher contact resistivities. A contact resistivity of $(1.2 \pm 0.9) \times 10^{-8} \text{cm}^{-3}$ and $(\pm 0.9) \times 10^{-8} \text{cm}^{-3}$ was obtained for W and Mo contacts, respectively, for a hole concentration of $2.2 \times 10^{20} \text{cm}^{-3}$. These contacts, however, show similar Schottky barrier height ($\approx 0.6 \text{eV}$). The reason for the difference in contact resistivities for these refractory metals could not be determined. Also, the contact resistivities were found to increase by about 50 % on annealing. SIMS, TEM, EDX and CV measurements were done to determine the reason for the increase in contact resistivity. However, no conclusive results were obtained.

In conclusion, we have demonstrated ultra-low resistance contacts to n-type InAs, n-type $\text{In}_{0.53}\text{Ga}_{0.47}\text{As}$ and p-type $\text{In}_{0.53}\text{Ga}_{0.47}\text{As}$ which make them a potential candidate to be applied in highly scaled HBTs and other devices of near-terahertz bandwidths.

8.3 Future Work

8.3.1 Epitaxial Contacts

The future work could involve focus on further reduction in contact resistivity for a particular active carrier concentration. Our theoretical calculations indicate that the contact resistivity can be further reduced if the Schottky barrier height is reduced. There is a possibility of changing the barrier height by the use of epitaxially grown metal contacts. The epitaxial contacts could satisfy the dangling bonds on the semiconductor surface and could result in unpinned Fermi level.

8.3.2 Regrown Base Ohmic Contacts

As mentioned previously, in a scaled HBT (80 nm emitter-base junction), the base is going to be very thin (≈ 20 nm). To make good ohmic contacts to this base, it is important to dope it very heavily. But this heavy doping could result in reduced current gain (β) due to Auger recombination. As a solution [60], heavily doped p-InGaAs can be regrown to form good ohmic contacts, whereas the intrinsic base could be kept thin and lightly doped. Figure 8.1 shows the SEM image of p-InGaAs regrown on dummy emitters. Further effort is required to optimize the doping concentration in the regrown layers.

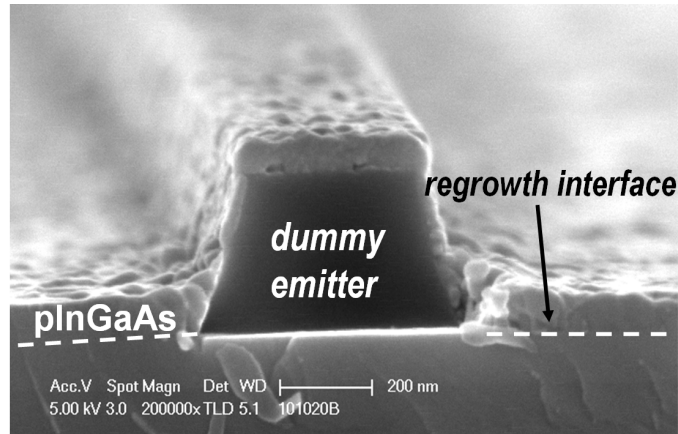


Figure 8.1: Scanning electron micrograph of p-InGaAs regrowth on dummy emitters.

8.3.3 Contact Resistivity Error Reduction

Since contact resistivity is extracted by extrapolation, the accuracy of extraction increases as we move closer to the y-axis i.e. smaller L_{gap} . TLM structures can be designed so as to have narrower separation between the metal pads (L_{gap}). This can be achieved by TLM gaps defined by electron beam lithography. Also, present TLM fabrication process steps result in non-uniform edges along the gap between the metal pads. If the process can be modified such that a uniform edge profile is obtained, the error in L_{gap} measurement (dL) could be reduced below 20 nm. This will result in reduced error margins and it will enhance the accuracy of the extracted contact resistivity.

8.3.4 Annealing Studies

Annealing studies could be pursued further to ascertain the reasons for increase in contact resistivity for p-type $\text{In}_{0.53}\text{Ga}_{0.47}\text{As}$. Atom probe microscopy could be utilized to determine the interdiffusion of species, if any, across the metal semiconductor interface.

Bibliography

- [1] Hideki Hasegawa, "Fermi Level Pinning and Schottky Barrier Height Control at Metal-Semiconductor Interfaces of InP and Related Materials," *Japanese Journal of Applied Physics*, 38 (1999) 1098.
- [2] U. Singiseti, *In_{0.53}Ga_{0.47}As MOSFETs with 5 nm channel and self-aligned source/drain by MBE regrowth*. PhD Thesis, 2009.
- [3] [http : //www.photonics.ethz.ch/research/core_competences/technology/epitaxial_growth/](http://www.photonics.ethz.ch/research/core_competences/technology/epitaxial_growth/)
- [4] <http://www.ioffe.ru/SVA/NSM/Semicond/index.html>.
- [5] D. Schroder, *Semiconductor Material and Device Characterization*. John Wiley and Sons, New Jersey, 2006.
- [6] E. F. Schubert, *Doping in III-V semiconductors*. Cambridge University Press, 1993.
- [7] James C. Li, Marko Sokolich, Tahir Hussain, Peter M. Asbeck, "Physical modeling of degenerately doped compound semiconductors for high-performance HBT design," *Solid State Electronics*, 50 (2006) 1440.
- [8] <http://www.nist.gov/pml/semiconductor/hall.cfm>.
- [9] F. Braun, "Über die Stromleitung durch Schwefelmetalle," *Ann. Phys. Chem.*, 153 (1874) 556.
- [10] W. Schottky, "Halbleiterttheorie der Sperrschicht," *Naturwissenschaften*, 26 (1938) 843.
- [11] N. F. Mott, "Note on the Contact between a Metal and an Insulator or Semiconductor," *Proc. Cambr. Philos. Soc.*, 34 (1938) 568.
- [12] H.K.Henisch, *Rectifying semiconductor contacts*. Clarendon Press, Oxford, 1957.

Bibliography

- [13] E.H.Rhoderick, *Metal-semiconductor contacts*. Clarendon Press, Oxford, 1977.
- [14] S.M.Sze and K. K. Ng., *Physics of Semiconductor Devices*. John Wiley and Sons, Inc., Hoboken, New Jersey, 2007.
- [15] E.H. Rhoderick, "Metal-Semiconductor Contacts," *IEE Proceedings*, 129 (1982) 1.
- [16] W. E. Spicer, P. W. Chye, P. R. Skeath, C. Y. Su and I Lindau, "New and unified model for Schottky barrier and IIIV insulator interface states formation," *Journal of Vacuum Science and Technology*, 16 (1979) 1422.
- [17] Volker Heine, "Theory of Surface States," *Physical Review*, 138 (1965) 1689.
- [18] J. Tersoff, "Schottky barriers and semiconductor band structures," *Physical Review B*, 32 (1985) 6968.
- [19] H. Hasegawa , "Unified disorder induced gap state model for insulatorsemiconductor and metalsemiconductor interfaces," *Journal of Vacuum Science and Technology B*, 4 (1986) 1130.
- [20] J. M. Woodall and J. L. Freeouf, "GaAs metallization: Some problems and trends," *Journal of Vacuum Science and Technology*, 19 (1981) 794.
- [21] F. A. Padovani and R. Stratton, "Field and Thermionic-Field Emission in Schottky Barriers," *Solid State Electronics*, 9 (1966) 695.
- [22] M. J. W. Rodwell, M. L. Le, B. Brar, "InP bipolar ICs: Scaling roadmaps, frequency limits, manufacturable technologies," *IEEE Proceedings*, 96 (2008) 271.
- [23] Rodwell et al, "THz Bipolar Transistor Circuits: Technical Feasibility, Technology Development, Integrated Circuit Results," in *2008 IEEE Compound Semiconductor IC Symposium*, October 12-14, Monterey, CA.
- [24] W. Liu, *Fundamentals of III-V Devices*. New York: John Wiley and Sons, 1999.
- [25] M. Rodwell, M. Wistey, U. Singisetti, G. Burek, A. Gossard, S. Stemmer, R. Engel-Herbert, Y. Hwang, Y. Zheng, C. Van de Walle, P. Asbeck, Y. Taur, A. Kummel, B. Yu, D. Wang, Y. Yuan, C. Palmstrom, E. Arkun, P. Simmonds, P. McIntyre, J. Harris, M. Fischetti, and C. Sachs., "Technology development and design for 22 nm InGaAs/InP-channel MOSFETs," in *20th International Conference on Indium Phosphide and Related Materials*, May 2008, pp. 1-6.

- [26] E. F. Chor, R. J. Malik, R. A. Hamm, and R. Ryan, "Metallurgical Stability of Ohmic Contacts in Base InP/InGaAs/InP HBTs," *IEEE Electron Device Letters*, 17 (1996) 62.
- [27] Yoshino K. Fukai, Kenji Kurishima, Norihide Kashio, Minoru Ida, Shoji Yamahata, Takatomo Enoki, "Emitter-metal-related degradation in InP-based HBTs operating at high current density and its suppression by refractory metal," *Microelectronics Reliability*, 49 (2009) 357.
- [28] A.G. Baca, F. Ren, J.C. Zolper, R.D. Briggs, S.J. Pearton, "A survey of ohmic contacts to III-V compound semiconductors," *Thin Solid Films*, 308 (1997) 599.
- [29] T. V. Blank and Yu. A. Goldberg, "Mechanisms of Current Flow in Metal Semiconductor Ohmic Contacts," *Semiconductors*, 41 (2007) 1263.
- [30] Vibhor Jain, Ashish K. Baraskar, Mark A. Wistey, Uttam Singiseti, Zach Griffith, Evan Lobisser, Brian J. Thibeault, Arthur. C. Gossard, Mark. J. W. Rodwell, "Effect of surface preparations on contact resistivity of TiW to highly doped n-InGaAs," in *IEEE, Intern. Conf. on Indium Phosphide and Related Materials*, 10-14 May 2009.
- [31] G. Stareev, H. Kijnzel and G. Dortmund, "A controllable mechanism of forming extremely low-resistance nonalloyed ohmic contacts to group III-V compound semiconductors," *Journal of Applied Physics*, 74 (1993) 7344.
- [32] Takumi Nittono, Hiroshi Ito, Osaake Nakajima and Tadao Ishibashi, "Non-Alloyed Ohmic Contacts to n-GaAs Using Compositionally Graded $\text{In}_x\text{Ga}_{1-x}\text{As}$ Layers," *Japanese Journal of Applied Physics*, 27 (1988) 1718.
- [33] Y. Shiraishi, N. Furuhashi and A. Okamoto, "Influence of metal-n-InAs-interlayer-n-GaAs structure on nonalloyed ohmic contact resistance," *Journal of Applied Physics*, 76 (1994) 5099.
- [34] S.L. Wright, R. F. Marks, S. Tiwari, T. N. Jackson, and H. Baratte, "In-situ contacts to GaAs based on InAs," *Applied Physics Letters*, 49 (1986) 1545.
- [35] C. K. Peng, J. Chen, J. Chyi, and H. Morkoc, "Extremely low nonalloyed and alloyed contact resistance using an InAs cap layer on InGaAs by MBE," *Applied Physics Letters*, 64 (1988) 429.
- [36] Z. Griffith, M.J.W. Rodwell, M. Dahlstrm, X.-M. Fang, D. Lubyshev, Y. Wu, J.M. Fastenau and W.K. Liu, " $\text{In}_{0.53}\text{Ga}_{0.47}\text{As}/\text{InP}$ Type-I DHBTs w/ 100 nm Collector and 491 GHz f_t , 415 GHz f_{max} ," in *2005 IEEE/OSA Conference on Indium Phosphide and Related Materials*, May 8-12, Glasgow.

- [37] Vibhor Jain, Evan Lobisser, Ashish Baraskar, Brian J. Thibeault, Mark Rodwell, Z Griffith, M Urteaga, S. T. Bartsch, D. Loubychev, A. Snyder, Y. Wu, J. M. Fasteau, W.K. Liu, "High performance 110 nm InGaAs/InP DHBTs in dry-etched in-situ refractory emitter contact technology," in *2010 IEEE Device Research Conference*, June 21-23, 2010.
- [38] E. F. Chor, D. Zhang, H. Gong, W. K. Chong and S. Y. Ong, "Electrical characterization, metallurgical investigation, and thermal stability studies of (Pd, Ti, Au)-based ohmic contacts," *Journal of Applied Physics*, 87 (2000) 2437.
- [39] P.K. Bhattacharya and M.D. Yeaman, "Enhanced barrier height of Au-In_{1-x}Ga_xAs_yP_{1-y} Schottky diodes," *Solid State Electronics*, 24 (1981) 297.
- [40] J.L. Veteran, D.P. Mullin and D.I. Elder, "Schottky barrier measurements on p-type In_{0.53}Ga_{0.47}As," *Thin Solid Films*, 97 (1982) 187.
- [41] C. A. Mead and W. G. Spitzer, "Fermi Level Position at Metal-Semiconductor Interfaces," *Physical Review*, 134 (1964) A713.
- [42] S. Bhargava, H. R. Blank, V. Narayanamurti and H. Kroemer, "Fermi-level pinning position at the AuInAs interface determined using ballistic electron emission microscopy," *Applied Physics Letters*, 70 (1997) 759.
- [43] A. Cho, "Film Deposition by Molecular Beam Techniques," *Journal of Vacuum Science and Technology*, 8 (1971) S31.
- [44] A. Cho and J. Arthur, "Molecular Beam Epitaxy," *Progress in Solid State Chemistry*, 10 (1975) 157.
- [45] M. A. Herman and H. Sitter, *Molecular Beam Epitaxy: Fundamentals and Current Status*. Springer-Verlag, 1997.
- [46] W. Braun, *Applied RHEED: Reflection High-Energy Electron Diffraction During Crystal Growth*. Springer, Germany, 1999.
- [47] H. H. Berger, "Models for Contacts to Planar Devices," *Solid State Electronics*, 15 (1972) 145.
- [48] Adam M. Crook, Erik Lind, Zach Griffith, Mark J. W. Rodwell, Jeremy D. Zimmerman, Arthur C. Gossard and Seth R. Bank, "Low resistance, nonalloyed Ohmic contacts to InGaAs," *Applied Physics Letters*, 2007.

Bibliography

- [49] U. Singiseti, M. A. Wistey, J. D. Zimmerman, B. J. Thibeault, M. J. W. Rodwell, A. C. Gossard, and S. R. Bank, "Ultralow resistance in situ Ohmic contacts to InGaAs/InP," *Applied Physics Letters*, 2008.
- [50] Ashish Baraskar, Mark A. Wistey, Vibhor Jain, Uttam Singiseti, Greg Burek, Brian Thibeault, Yong Ju Lee, Arthur Gossard and Mark Rodwell, "Ultralow resistance, nonalloyed Ohmic contacts to n-InGaAs," *Journal of Vacuum Science and Technology B*, 2009.
- [51] Y. G. Chai, R. Chow, and C. E. C. Wood, "The effect of growth conditions on Si incorporation in molecular beam epitaxial GaAs," *Applied Physics Letters*, 1981.
- [52] J. H. Neave, P. J. Dobson, J. J. Harris, P. Dawson, and B. A. Joyce, "Silicon Doping of MBE-Grown GaAs Films," *Applied Physics A*, 1983.
- [53] B.I.Shklovskii and A.L.Efros, *Electronic properties of doped semiconductors*. Springer, Berlin, 1984.
- [54] Maguire et al, "Mechanism of compensation in heavily Si doped GaAs by MBE," *Applied Physics Letters*, 50 (1987) 516.
- [55] R. Driad, Z.H. Lu, S. Laframboise, D. Scansen, W.R. McKinnon and S.P. McAlister, "Surface passivation of InGaAs/InP heterostructures using UV-irradiation and ozone," in *IEEE, 10th Intern. Conf. on Indium Phosphide and Related Materials*, 11-15 May 1998.
- [56] Z. H. Lu, B. Bryskiewicz, J. McCaffrey, Z. Wasilewski, and M. J. Graham, "Ultraviolet-ozone oxidation of GaAs(100) and InP(100)," *Journal of Vacuum Science and Technology B*, 1993.
- [57] G. R. Bell, N. S. Kaijaks, R. J. Dixon, and C. F. McConville, "Atomic hydrogen cleaning of polar III-V semiconductor surfaces," *Surface Science*, 401, (1998) 125.
- [58] Takeyoshi Sugaya and Mitsuo Kawabe, "Low-Temperature Cleaning of GaAs Substrate by Atomic Hydrogen Irradiation," *Japanese Journal of Applied Physics*, 30 (1991) 402.
- [59] A. Khatiri, J.M. Ripalda, T.J. Krzyzewski, G.R. Bell, C.F. McConville, T.S. Jones, "Atomic hydrogen clean of GaAs (001): STM study," *Surface Science*, 548 (2004) L1L6.
- [60] U.Singiseti, M.A. Wistey, G.J. Burek, A.K. Baraskar, J. Cagnon, B.J. Thibeault, A.Gossard, S. Stemmer, M. Rodwell, E.Kim, B.Shin, P.C McIntyre,

- “ $\text{In}_{0.53}\text{Ga}_{0.47}\text{As}$ channel MOSFETs with self-aligned InAs Source/Drain formed by MEE regrowth,” *IEEE Electron Device Letters*, 30 (2009) 1128.
- [61] P.A. Bone, J.M. Ripalda, G.R. Bell, T.S. Jones, “Surface reconstructions of In-GaAs alloys,” *Surface Science*, 600 (2006) 973.
- [62] F. S. Aguirre-Tostado, M. Milojevic, C. L. Hinkle, E. M. Vogel, R. M. Wallace, S. McDonnell, and G. J. Hughes, “Indium stability on InGaAs during atomic H surface cleaning,” *Applied Physics Letters*, 92 (2008) 171906.
- [63] E.G.Woelk, H.Krautle, H.Beneking, “Measurement of low resistive ohmic contacts on semiconductors,” *IEEE Transactions on Electron Devices*, ED-33 (1986) 19.
- [64] Byoung-Ho Cheong and K. J. Chang, “Compensation and diffusion mechanisms of carbon dopants in GaAs,” *Physical Review B*, 49 (1994) 17436.
- [65] R. Zhang, S.F. Yoon, K.H. Tan, Z.Z. Sun, Q.F. Huang, “Effects of carbon tetrabromide flux, substrate temperature and growth rate on carbon-doped GaAs grown by molecular beam epitaxy,” *Journal of Crystal Growth*, 262 (2004) 113.
- [66] K. H. Tan, S. F. Yoon, Q. F. Huang, R. Zhang, and Z. Z. Sun, “Dicarbon defects in carbon-doped GaAs,” *Physical Review B*, 67 (2003) 035208.
- [67] Z. Z. Sun, S. F. Yoon, K. H. Tan, R. Zhang and J. Jiang, “Incorporation efficiency of carbon in GaAs using carbon tetrabromide in solid source molecular beam epitaxy,” *Journal of Vacuum Science and Technology B*, 22 (2004) 1017.
- [68] Lubyshev et al, “A comparative study of carbon incorporation in heavily doped GaAs and $\text{Al}_{0.3}\text{Ga}_{0.7}\text{As}$ grown by solid-source molecular beam epitaxy using carbon tetrabromide,” *Journal of Vacuum Science and Technology B*, 1999.
- [69] P. J. Lemonias, W. E. Hoke, D. G. Weir, and H. T. Hendriks, “Carbon p+ doping of molecular-beam epitaxial GaAs films using carbon tetrabromide,” *Journal of Vacuum Science and Technology B*, 1994.
- [70] M. McEllistrem and J. M. White, “Surface chemistry of carbon tetrabromide on GaAs(100),” *Journal of Vacuum Science and Technology A*, 1994.
- [71] Cai et al, “Heavily carbon-doped $\text{In}_{0.53}\text{Ga}_{0.47}\text{As}$ on InP (001) substrate grown by solid source molecular beam epitaxy,” *Journal of Vacuum Science and Technology B*, 1999.

Bibliography

- [72] A. Amore Bonapasta, "Hydrogen passivation of carbon-doped gallium arsenide," *Physical Review B*, 48 (1993) 8771.
- [73] C. R. Abernathy and W. S. Hobson, "Carbon-impurity incorporation during the growth of epitaxial group III-V materials," *Journal of Materials Science: Materials in Electronics*, 7 (1996) 1.
- [74] J. H. Davies, *The Physics of Low-Dimensional Semiconductors: An Introduction*. Cambridge University Press, 1998.
- [75] C. R. Crowell and V. L. Rideout, "Normalized thermionic-field (T-F) emission in metal-semiconductor (Schottky) barriers," *Solid-State Electronics*, 12 (1969) 89.
- [76] D.N.Christodoulides, A.G.Andreou, R.I.Joseph and C.R.Westgate, "Analytical Calculation Of The Quantum Mechanical Transmission Coefficient For A Triangular, Planar-Doped Potential Barrier," *Solid State Electronics*, 28 (1985) 821.
- [77] M. Abramowitz and I. Stegun, *Handbook of Mathematical Functions*. Dover, New York, 1970.
- [78] R. Eisberg and R. Resnick, *Quantum Physics*. John Wiley and Sons, 1985.
- [79] L. Reggiani, *Hot-Electron Transport in Semiconductors*. Springer, New York, 1985.
- [80] A. Levi, *Applied Quantum Mechanics*. Cambridge University Press, 2003.
- [81] D.Schroeder, *Modelling of Interface Carrier Transport for Device Simulation*. Springer-Verlag Wien New York, 1994.

Appendix A

Transformation of k -vectors

Proof of: $v_{mz}(k_s)dk_{mx}dk_{my}dk_{mz} = v_{sz}(k_m)dk_{sx}dk_{sy}dk_{sz}$ [81]
 From conservation of total energy (E_T) across the interface:

$$E_T = E_m(k_m) = q\phi_R + E_s(k_s) \quad (\text{A.1})$$

From conservation of tangential crystal momentum:

$$k_{mx} = k_{sx}; k_{my} = k_{sy} \quad (\text{A.2})$$

The electron velocity is given by:

$$v_{ij} = \frac{1}{\hbar} \frac{\partial E_i}{\partial k_{ij}} \quad (\text{A.3})$$

From equation A.1,

$$\frac{\partial E_m}{\partial k_{mz}} = \frac{\partial E_s}{\partial k_{sx}} \frac{\partial k_{sx}}{\partial k_{mz}} + \frac{\partial E_s}{\partial k_{sy}} \frac{\partial k_{sy}}{\partial k_{mz}} + \frac{\partial E_s}{\partial k_{sz}} \frac{\partial k_{sz}}{\partial k_{mz}} \quad (\text{A.4})$$

$$\frac{\partial E_m}{\partial k_{mz}} = \frac{\partial E_s}{\partial k_{sz}} \frac{\partial k_{sz}}{\partial k_{mz}} \quad (\text{since } \frac{\partial k_{sx}}{\partial k_{mz}} = 0; \frac{\partial k_{sy}}{\partial k_{mz}} = 0) \quad (\text{A.5})$$

From equations A.4 and A.5

$$v_{mz}(k_m) = v_{sz}(k_s) \frac{\partial k_{sz}}{\partial k_{mz}} \quad (\text{A.6})$$

Now,

$$v_{sz}(k_s)dk_{sx}dk_{sy}dk_{sz} = v_{mz}(k_m) \left(\frac{\partial k_{sz}}{\partial k_{mz}} \right)^{-1} \left| \frac{D(k_s)}{D(k_m)} \right| dk_{mx}dk_{my}dk_{mz} \quad (\text{A.7})$$

Appendix A. Transformation of k -vectors

where,

$$\frac{D(k_s)}{D(k_m)} = \begin{vmatrix} \frac{\partial k_{sx}}{\partial k_{mx}} & \frac{\partial k_{sx}}{\partial k_{my}} & \frac{\partial k_{sx}}{\partial k_{mz}} \\ \frac{\partial k_{sy}}{\partial k_{mx}} & \frac{\partial k_{sy}}{\partial k_{my}} & \frac{\partial k_{sy}}{\partial k_{mz}} \\ \frac{\partial k_{sz}}{\partial k_{mx}} & \frac{\partial k_{sz}}{\partial k_{my}} & \frac{\partial k_{sz}}{\partial k_{mz}} \end{vmatrix} \quad (\text{A.8})$$

From equation A.2,

$$\frac{D(k_s)}{D(k_m)} = \begin{vmatrix} 1 & 0 & 0 \\ 0 & 1 & 0 \\ \frac{\partial k_{sz}}{\partial k_{mx}} & \frac{\partial k_{sz}}{\partial k_{my}} & \frac{\partial k_{sz}}{\partial k_{mz}} \end{vmatrix} = \frac{\partial k_{sz}}{\partial k_{mz}} \quad (\text{A.9})$$

$$\Rightarrow v_{sz}(k_s)dk_{sx}dk_{sy}dk_{sz} = v_{mz}(k_m)dk_{mx}dk_{my}dk_{mz}$$

Appendix B

TLM Fabrication Process Flow

1. Surface preparation and contact metal deposition

(a) In-situ contacts

- i. Cool down the samples after epilayer growth in MBE chamber.
- ii. Isolate the e-beam metal deposition chamber and outgas the metal source.
Let the source cool down
- iii. Transfer the sample to the metal deposition chamber
- iv. Deposit 20 nm of contact metal at a growth rate of $0.2 \text{ \AA}/\text{sec}$

(b) Ex-situ contacts

- i. E-beam metal deposition chamber preparation
 - A. Load the source material in the chamber
 - B. Pump down to 2×10^{-6} Torr
 - C. Outgas the source material
- ii. Sample surface preparation
 - A. Solvent clean: 3 min acetone, 3 min iso-propanol and 3 min DI rinse
 - B. Dehydration at 110 C for 10 mins, cool the sample for 5 mins
 - C. Clean the UV ozone chamber for 30 mins
 - D. Oxidize the sample in UV ozone chamber for 30 mins
 - E. Etch the samples in 1:10 HCl:DI solution for 1 min, DI rinse - 1 min, N₂ dry
 - F. Immediate transfer to e-beam metal deposition (e-beam 1) chamber
- iii. Metal deposition
 - A. Pump down to 2×10^{-6} Torr

B. Deposit 20 nm of contact metal at a growth rate of $0.2 \text{ \AA}/\text{sec}$

(c) Quasi ex-situ contacts

Note: As of now, fabrication of this type of contacts requires the use of MBE system (for H clean and RHEED). Hence, it is extremely important to keep the samples as well as the tweezers, beakers and sample baskets used for sample preparation free of Au and photoresist.

- i. Prepare the sample surface as explained above
- ii. Immediate transfer to MBE system (entry-exit chamber)
- iii. Bake the sample for atleast 3 hours at $200 \text{ }^\circ\text{C}$. Let the sample cool down before moving to the next step.
- iv. Transfer the sample to buffer chamber and bake at $325 \text{ }^\circ\text{C}$ for 30 mins
- v. Expose the sample to atomic hydrogen
 - A. Substrate temperature = $420 \text{ }^\circ\text{C}$
 - B. Chamber pressure (with hydrogen) = 10^{-6} Torr
 - C. Exposure time = 40 mins
- vi. Let the sample cool down and the chamber pressure to drop below 10^{-6} Torr
- vii. Transfer to growth chamber, verify surface reconstruction with RHEED
- viii. Isolate the e-beam metal deposition chamber and outgas the metal source. Let the source cool down
- ix. Transfer the sample to e-beam chamber connected to MBE system
- x. Deposit 20 nm of contact metal at a growth rate of $0.2 \text{ \AA}/\text{sec}$

2. Photolithography I: Formation of lift off pattern (Autostepper)

- (a) Solvent clean the sample
- (b) Spin coat negative PR nLOF5510 @4000 rpm for 30 secs (recipe 7)
- (c) Pre bake at $90 \text{ }^\circ\text{C}$ for 1 min
- (d) Shoot TLM first layer. Expose for 0.55 sec for Mo, W and Ir. Use $500 \mu\text{m}$ chuck for $500 \mu\text{m}$ thick wafers
- (e) Post bake at $110 \text{ }^\circ\text{C}$ for 1 min
- (f) Develop in MIF300 solution for 90 secs. Do NOT stir or agitate the sample. Immediate rinse for 2-3 mins in DI water. Stirring blurs the smallest feature size. Verify the pattern under microscope.

3. Metal deposition

- (a) Load the sample in e-beam 4. Wait for it to pump down below 2×10^{-6} Torr
- (b) Deposit Ti/Au/Ni 20/500/50 nm

4. Lift-off

- (a) Dip the substrate in 1165 stripper at 80 C for an hour. Agitation of solution is required. Not advisable to leave the samples in 1165 for a long time (1165 etches off W)
- (b) Immediate transfer to ISO for 3 mins
- (c) DI water rinse for 3 mins, N2 dry

5. Dry etch of contact metal (Panasonic ICP etch) (Eriks process) (Etch recipe varies depending on the metal being etched)

- (a) Change gas to SF₆ and Ar
- (b) Clean carrier wafer and chamber, 20min O₂ plasma (std. O₂ recipe: 121), 3min chamber coat with SF₆/Ar etch recipe: 162) (600W ICP, 150W RF, 50 sccm SF₆, 5 sccm Ar, 1Pa)
- (c) Attach samples to carrier wafer
- (d) Use the etch recipes below:
 - i. For 20 nm Mo: 2min30sec SF₆/Ar etch (600W ICP, 15W RF, 50 sccm SF₆, 5 sccm Ar, 1Pa)
 - ii. For 20 nm W: 30 secs SF₆/Ar etch (600W ICP, 15W RF, 50 sccm SF₆, 5 sccm Ar, 1Pa)
 - iii. For 20 nm Ir: 4 min SF₆/Ar etch (600W ICP, 50W RF, 50 sccm SF₆, 5 sccm Ar, 1Pa)
 - iv. For 20 nm Ru: 10 min SF₆/Ar etch (600W ICP, 50W RF, 50 sccm SF₆, 5 sccm Ar, 1Pa)
- (e) Sample should look smooth without color variations; an extra 15-30 sec etch is advisable for thick semiconductor layers to ensure complete removal of metal (not advisable for thin semiconductor layers as the etch may affect the surface)
- (f) Change the SF₆ gas to CF₄
- (g) Wafer clean 3 min DI, 3 min Acetone, 3 min ISO, 3 min DI. Observe under microscope to ensure the uniformity of the etch.

6. Photolithography II: Isolation Etch (Autostepper)

- (a) Spin coat positive PR SPR510 @4000 rpm for 30 secs (recipe 7)
- (b) Pre bake at 90C for 1 min
- (c) Shoot TLM second layer; expose for 0.27 secs
- (d) Post bake at 110 C for 1 min
- (e) Develop in AZ300MIF solution for 60 secs. Slightly stir or agitate the sample. Immediate rinse for 2-3 mins in DI water. Verify the pattern under microscope

7. Wet etching

- (a) Prepare InGaAs Etchant - 1:1:25 H₃PO₄:H₂O₂:DI
- (b) Etch sample in solution, immediate rinse and N₂ dry; observe under Dektak

8. Photoresist Stripping

- (a) Dip the substrate in 1165 stripper at 80 °C for 20-30 mins
- (b) Immediate transfer to ISO (2-3 mins clean) and DI rinse
- (c) DI water rinse for 3 mins, N₂ dry. Observe under microscope to ensure there is no photoresist left on the wafer